ESTIMATION AND CONTROL OF CONTAMINANT TRANSPORT IN WATER RESERVOIRS

NGUYEN NGOC HIEN

(B. Eng (Hons), Ho Chi Minh City University of Technology)

A THESIS SUBMITTED

FOR THE DEGREE OF DOCTOR OF PHILOSOPHY

IN COMPUTATIONAL ENGINEERING (CE)

SINGAPORE-MIT ALLIANCE

NATIONAL UNIVERSITY OF SINGAPORE

2012

DECLARATION

I hereby declare that this thesis is my original work and it has been written by me in its entirety. I have duly acknowledged all the sources of information which have been used in the thesis.

This thesis has also not been submitted for any degree in any university previously.

Nguyen Ngoc Hien

November 19, 2012

Acknowledgments

It is time for me to express my deepest gratitude to my supervisors, my friends and my family and wife for all the things they have done to support me to finish this dissertation.

First and foremost, my utmost gratitude to Prof. Karen Willcox whose encouragement, guidance, understanding and support I will never forget. Her wisdom, knowledge and commitment to the highest standards inspired and motivated me. Her excellent guidance, discussions and patience helped me in all the time of research and writing. Her supports in both the academic life and real life provided me an excellent atmosphere for studying. It is very lucky for me to have a very nice advisor. I could not have imagined having a better advisor for my Ph.D. time.

Second, I am heartily thankful to Prof. Khoo Boo Cheong, who let me experience the very interested research of reservoir's water problems, constantly and patiently guided and corrected my writing and financially supported my research. I would also like to express my appreciation and thank for his kind helps and support for the past several years since I applied for Ph.D. candidate at Singapore-MIT Alliance program.

I am grateful to Prof. Nguyen Thien Tong for teaching me with a strong background and then supporting and encouraging me to follow the professional academic path and to pursue this degree. My life has turned to a new page with many chances to fulfil my long cherished dream. I am really appreciated for what he has done for me.

motivations to move forward for not only this degree but also for all the future

targets.

Contents

Thesis summary

This thesis presents an end-to-end measure-invert-control strategy for a stochastic problem with application to the management of water quality in a reservoir system. The strategy involves estimating uncertain contaminant source locations within a reservoir, followed by applying an optimal velocity field control to flush the contaminant out of the reservoir, while accounting for uncertainty such as wind velocity and measurement noise. This thesis first develops a finite element numerical simulation code for a 2D laterally averaged reservoir model. The numerical code is validated through comparisons to various benchmark problems. Numerical results show that the simulated hydrodynamic processes are in good agreement with theoretical and experimental data. The determination of the contaminant source location is posed as a Bayesian inference problem and solved using a Markov chain Monte Carlo (MCMC) method. Gaussian mixture models are used to approximately represent the posterior distribution of estimated source locations. The stochastic control problem then seeks an optimal velocity to flush the contaminant out of the reservoir. This control problem is solved using an adjoint method together with collocation over the space of uncertain parameters.

For large-scale models, such as for reservoir applications, these computa-

tional simulations are expensive and time-consuming. Furthermore, due to the stochastic nature of the problem, the computational costs and storage requirements increase rapidly. Thus, this thesis develops a reduced-order model (ROM) that approximates the full model but provides computational speedups. The ROM for the reservoir system is obtained using the proper orthogonal decomposition (POD) and Galerkin projection techniques. To validate and demonstrate the efficiency of the ROM, two examples are considered. The first is a simple 2D transport model with a constant velocity field, and the second is a coupled Navier-Stokes and transport model. In both cases, the final purpose is to flush the contaminant out of the domain with the lowest cost. In the transport example, the ROM decreases the computational time of solution by a factor of approximately 25, while in the coupled Navier-Stokes/transport model, the speedup is by a factor of approximately 90. In both cases, the reduced-order solver is effective for solving the Bayesian inference problem and the stochastic control problem. The control actions lead to a cleaner body of water as compared to the uncontrolled case. These results suggest that the POD-based ROMs may be an effective tool for water quality management.

List of Tables

List of Figures

List of Symbols

Nomenclature with Greek symbols

Symbols	Description	Units
$\alpha(t)$	Time dependent amplitude of POD velocity basis	none
$\gamma(t)$	Time dependent amplitude of POD contaminant basis	none
ρ	Density of water	$\frac{Kg}{m^3}$
ρ_a	Density of air	$\frac{Kg}{m^3}$
μ	Dynamic viscosity	$\frac{Kg}{m.sec}$
μ_x	Longitudinal dynamic viscosity	$\frac{Kg}{m.sec}$
μ_z	Vertical dynamic viscosity	$\frac{Kg}{m.sec}$
μ_t	The eddy dynamic viscosity	$\frac{Kg}{m.sec}$
κ	Diffusivity coefficient	$\frac{Kg}{m.sec}$
κ_x	Longitudinal diffusivity coefficient	$\frac{Kg}{m.sec}$
κ_z	Vertical diffusivity coefficient	$\frac{Kg}{m.sec}$
κ_v	Dimensionless of diffusivity coefficient	none
λ	Thermal conductivity	$\frac{J}{m.sec.K}$
λ_x	Longitudinal thermal conductivity	$\frac{J}{m.sec.K}$
λ_v	Dimensionless of thermal conductivity coefficient	none

Symbols	Description	Units
ν	Dimensionless of fluid kinematic viscosity	none
ϕ	Finite element basis function	none
$\boldsymbol{\phi}$	The contaminant source location	none
$\boldsymbol{\Phi}(\mathbf{x})$	The POD velocity basis vector	none
$\boldsymbol{\Psi}(\mathbf{x})$	The POD contaminant basis vector	none
δ	The boundary layer thickness	m
θ	A constant use in one-step theta schemes	none
$\boldsymbol{\theta}_k$	The kth collocation point	none
ξ, η	A coordinate in collocation space	none
η_w	A constant controlling the relative weighting of cost function	none
$\boldsymbol{\eta}_t$	A vector noise	none
ω	Random variable	none
Ω	The sample space	none
Γ	Boundary of the domain	none
Γ_D	Boundary with Dirichlet condition	none
Γ_N	Boundary with Neumann condition	none
Γ_c	Boundary with control function applied	none
ε_F	Time-dependent relative error norm of solution	none
ε_y	Time-dependent relative error norm of outputs	none
ε_F^T	Space-time norm erorr of solution	none
σ	The width of the white noise	none
σ_{sk}	The kth of the width of external source	none
τ_k	The algorithmic parameter	none
τ_{supg}	The intrinsic time parameter	none

Nomenclature with English symbols

Symbols	Description	Units
$\begin{aligned}&a_i\\&b_{ij}\\&c_{ijk}\end{aligned}$	Coefficients in the mode amplitude equations of velocity	none
$\begin{aligned}&\bar{a}_{mi}\\&\bar{a}_{uik}\\&\bar{a}_{hi}\\&\bar{b}_{mij}\end{aligned}$	Coefficients in the mode amplitude equations of contaminant	none
B	The local width of the domain	m
c_p	The specific heat of water	$\frac{KJ}{Kg.K}$
c	A contaminant concentration	$\frac{Kg}{m^3}$
$\mathcal{D}$	Physical and computational domain	none
Fr	Froude number	none
$G(\boldsymbol{\theta})$	the forward model	none
h_e	the local size of element	none
H	The average depth of reservoir	m
m	A size of general ROM	none
M_u	A size of ROM of velocity	none
M_c	A size of ROM of contaminant	none
N	The size of full order model	none
N_G	Number of Gaussian mixture models	none
N_{mcmc}	Total number of samples	none
N_{snap}^u	Number of velocity snapshot	none
N_{snap}^c	Number of contaminant snapshot	none
p	Pressure	Pa
p_{atm}	Pressure at atmosphere	Pa
P	Number of collocation points	none

Symbols	Description	Units
Pe	Péclet number	none
Pr	Prandtl number	none
R r_1 r_{2i} r_{3ij}	The weighted matrices in the objective function	none
Re	Reynolds number	none
R_N	Total net heat flux	$\frac{W}{m^2}$
R_{SN}	The net solar shortwave radiation	$\frac{W}{m^2}$
R_{AN}	The down-welling longwave radiation	$\frac{W}{m^2}$
R_{BR}	The up-welling longwave radiation	$\frac{W}{m^2}$
R_C	The sensible heat flux	$\frac{W}{m^2}$
R_L	The latent heat flux	$\frac{W}{m^2}$
t	Time	sec
t_0	Initial time of the simulation	sec
t_f	Final time of the simulation	sec
t_{off}	The shut of time of the source	sec
T	Water temperature	^0C
T_a	Atmosphere temperature	^0C
T_s	Water surface temperature	^0C
T_b	Water depth temperature	^0C
u	Velocity component in x-direction	$\frac{m}{s}$
v	Velocity component in y-direction	$\frac{m}{s}$
w	Velocity component in z-direction	$\frac{m}{s}$
w^k	The kth weight of collocation space	none
$\mathbf{Y}(\omega)$	The independent random variables	none

Chapter 1

Introduction

1.1 Motivation

Lakes and reservoirs are the main places to store rainwater in nature. The stored water can be used for many purposes such as agriculture, industry, daily activities, etc. The stored water is also an important factor in the development strategies of the government, especially in water-shortage countries. For example, Singapore is considered as one of the water-shortage countries because of its dependence on imports of water from Malaysia and its limited amount of land area where rainwater can be stored. In order to reduce the dependence on external sources, the Government has built up many reservoirs from river systems to store water. Rainwater, runoff water, etc., are collected and initially treated by a system of storm drains and storm sewers before entering a reservoir. However, there can be other unexpected water sources that flow directly into the reservoir. These unexpected sources may contain contaminant concentrations that cause pollution of the water body. Hence before the stored water treated for

consumption, it is important to monitor, determine and remove any (suspected) contaminants as much as possible out of the water system.

Estimating and locating contaminant sources and then applying the control to flush them out of the water system are the rudimentary tasks of water quality management. The tasks require knowledge of physics, hydrodynamics, data assimilation and optimal control. To understand the behavior of water in reservoirs, hydrodynamics models are needed. In general, environmental flows are all three-dimensional (3D). Modeling the hydrodynamics and water quality in 3D will require much effort due to their complexity. Two-dimensional (2D) models, in some cases, may provide predictions of adequate accuracy while being computationally cheaper than 3D models. Two popular models for simulating water quality in lakes and reservoirs are DYRESM (1981) [3] and CE-QUAL-W2 (1994) [4]. These existing models have been used for simulation and validation for many studies and applications . For example, Gu and Chung (2003) [5] studied the transport and fate of toxic chemicals in a stratified reservoir by modeling the toxic sub-model, then linked to CE-QUAL-W2 model using Microsoft Fortran Power-station program. However, the existing models are not appropriate in some cases due to their complexity or their requirements. Furthermore because of the large-scale reservoirs, these existing models may be expensive with respect to both computational costs and storage requirements. Thus, developing an appropriate methodology to study the dynamics of water quality in lakes and reservoirs directly for our specific purpose is considered.

Considering optimal flow control for reservoir applications, we have to deal with many uncertain parameters relating to the instrumentations that measure

2

the wind speed, water circulation currents, contaminant species and others. These uncertain parameters may have undue influence on the system. As such these need to be properly accounted for as stochastic variables in the system model. The objective of control is to flush the contaminant out of the domain in a short time. The problem may not be too difficult if we know exactly the location of the contaminant in the domain. However, complexities arise if we are only given spatially sparse measurements of the contaminant concentrations. To apply the control effectively, we have to first estimate the contaminant locations. In realistic applications, measured data are subject to a degree of uncertainty and noise. Hence, we pose the parameter estimation problem. We formulate the statistical inverse problem using a Bayesian approach, which accounts for measurement noise and represents uncertainty in model parameters using probability distributions [6, 7]. Under the Bayesian framework, the nonlinear equations governing the system of interest need to be solved repeatedly over the different sample of input parameters. There are available sampling strategies associated with Bayesian computation such as the Markov chain Monte Carlo (MCMC) methods [8, 9, 10, 11].

Finding the solution of the optimal flow control problem can be a computationally expensive undertaking. For simulations to support real-time decision-making in applications governed by the partial differential equations (PDEs), the discretized models may have many thousands or even million degrees of freedom. The situation is even more challenging for stochastic control problems in respect to both storage and computational cost. The computational costs and storage requirements increase very rapidly due to the stochastic nature of the

simulations and optimization formulation. In such situations, the use of tradi-
tional discretization methods, such as finite element or finite volume methods,
to achieve real-time simulations may be infeasible. To address these challenges,
the development of a systematic model reduction technique for the end-to-end
strategy: measure-invert-control for a stochastic problem that minimizes com-
putational costs and storage requirements but retaining accuracy is of particular
interest.

1.2 Background

1.2.1 State of the art in reservoir simulations

Reservoirs are usually constructed at low topographic locations to receive basins
downstream. As a result, reservoirs receive large water inflows from the sur-
rounding watershed. The flushing/flow rates are also rapid in order to balance
water volume in reservoirs. Thus, although there is large variation in water qual-
ity such as pollution loads entering reservoirs from inflows, reservoirs have the
potential to flush these pollutants out rapidly. This process is called the contam-
inant transport process where water velocities play a key role in the near field
and wind induced water velocity is an important factor in the far field. In this
process, the inflows push the water towards and outflows pull/push the water
out, while the wind induced flow exerts a drag on the water surface and causes
floating objects to move in the wind direction. Wind induced flow also causes
the circulation of water, mixing the water surface and transferring heat from at-
mosphere to the water column. The mixing water process is another important

process where the water is enriched with important gases like dissolved oxygen and carbon dioxide that are essential for aquatic life. Furthermore, the temperature distribution in the water body, namely the thermal stratification process which is affected by the heat exchange and water circulation, is important for aquatic life. A better understanding of these processes is important in managing water resources effectively.

To simulate such processes, for example the contaminant transport process, a coupled system of partial differential equations (PDEs) including the Navier-Stokes equations and transport equations needs to be solved iteratively. The general system of equations for the reservoir is derived from the three dimensional Navier-Stokes equations, energy equation and transport equation. The 3D modeling is needed in order to provide detailed solution of the fluid flow. However 3D models are often too complex to build and have long run-times. For the lake and reservoir systems, flow variations over the vertical and longitudinal directions are important, so an appropriate 2D model is a laterally averaged model. There are many textbooks that describe the hydrodynamics models for lake and reservoirs in more detail, such as Ji [12], Martin [13], Orlob [14], and Rubin and Atkinson [15]).

1.2.2 Inverse problems

The direct or forward problems compute the distribution of contaminant directly from given input information such as contaminant location, contaminant properties, fluid flow properties, boundary conditions, initial conditions, etc. On the contrary, the inverse problems infer the unknown physical parameters, boundary

conditions, initial conditions or geometry given a set of measured data. In recent years, the inverse problems have been studied and applied widely to many fields, especially in computational fluid dynamics because of their importance in environmental applications. For example, determining the sources of toxic chemical released on the subways or airports [16] or the pollutant sources of the water-bodies [17] or groundwater contaminant [18], etc. There are several approaches to solve inverse problems such as analytical approach, optimization approach, and probabilistic approach (for more details, see [19]).

The Bayesian inference approach provides a statistical solution to the inverse problem. The Bayesian approach provides a general framework for the formulation of a wide variety of inverse problems such as climate modeling [20], contaminant transport model [21, 22, 23] and heat transfer [24]. However, with complex systems described by partial differential equations, it usually leads to very large numerical models that are too expensive to solve with respect to both storage and computation cost. For Bayesian approach, the outputs of interest need to be evaluated repeatedly for each possible value of the input parameters, and each single evaluation can be a computationally expensive undertaking.

1.2.3 Optimal control for reservoir problems

Optimal control can be used as a strategy to treat the polluted water in groundwater, rivers and reservoirs. For example, Nicklow et al. [25] applied the control on water discharge to minimize sediment scour and deposition in rivers and reservoirs, while Fontane et al. [26] controlled discharge water to obtain a desired target level of the thermal stratification cycle. In the study by Zeitouni [27],

the control applies to the quantity of contaminating chemical on each aquifer which is described by the two-dimensional advection-diffusion equation. In the study by Bhat et al. [28], the surface of water in a large river is modeled by an advection-diffusion partial differential equation. They considered the chemical and sediment loading as a point inflow source of contaminant and developed an optimal control model to determine the optimal pollutant loads at different influx points along the course of a river in order to reduce the environmental damage costs. In the study by Alvarez-Vazquez et al. [29], the strategy consists of the injection of clean water from a reservoir at a nearby point into the river in order to dilute the contaminant in the water up to a certain level in a short period of time. Lenhart [30] has studied an optimal control of a parabolic differential equation, which is modeling the one-dimensional fluid through a soil-packed tube in which a contaminant is initially distributed. Lenhart considered the convective velocity as a control variable. However this framework deals with the one-dimensional deterministic problem and just stands on the theoretical ground. The challenge is for higher dimensional stochastic problems in practical engineering applications.

Despite these above mentioned works, most of the studies dealt with the one dimensional deterministic problem and used transport equations as state equations. It lacks of the generality because the movement of water in reservoir plays a key role in distributing the polluted species. Thus in the control of fluid dynamical system, state equations should be included with momentum equations or Navier-Stokes equations.

In recent years, interest has increased in optimal control problems that in-

volved the Navier-Stokes equations. These problems are challenging because of their complexity in numerical approximations of the Navier-Stokes equations and in the derivation of the optimal formulations. The numerical methods for optimal flow control problems have benefited much from the development of computer/supercomputer together with the development of numerical methods for flow simulation. Adjoint-based methods are one approach used for the solution of flow control and optimization problems. This approach has been widely considered in [31, 32, 33, 34, 35, 36, 37, 38, 39] with respect to both theoretical results and numerical approximations.

To address the stochastic issue in the optimal flow control, the stochastic collocation method is a suitable approach. In the collocation framework, candidate solutions are computed at sample points in the multi-dimensional stochastic space. The global solution of the SPDEs is then represented using interpolation functions [40, 41, 42]. The Smolyak algorithm provides a minimal number of collocation points to construct the interpolation functions, which for many problems leads to efficient and accurate representation of the stochastic solutions [43, 40]. The sparse grid collocation method has been widely applied to stochastic applications, such as natural convection problems [44], source inversion and flow through porous media [45].

For the approaches discussed so far, optimal control problems will be too expensive to solve with respect to both computational costs and storage requirements. This is because each iteration requires to solve at least one non-linear solver. For stochastic control problems, the situation is worse because we have to determine multiple realization of the state system at each iteration. Thus,

reduced order models are studied to reduce the cost.

1.2.4 Model order reduction for reservoir management applications

Model order reduction techniques aim to reduce the dimension of a state-space system, while retaining the characteristic dynamics of the system and preserving the input-output relationship [46]. Many large-scale model reduction frameworks are based on projection approach. The idea is to approximate any solution of the PDEs of interest as a linear combination of solutions that have been pre-computed and to project the large-scale governing equations onto the subspace spanned by a reduced-space basis, hence yielding a low-order dynamical system. Methods to compute the basis include balanced truncation [47, 48], Krylov-subspace [49, 50], and proper orthogonal decomposition methods [51, 52].

The most popular technique to find the basis is the proper orthogonal decomposition (POD). POD provides an orthogonal basis for a set of data, which origin may be theoretical, experimental or computational data. Sirovich introduced the method of snapshots, where each snapshot contains spatial data obtained from numerical simulation at a fixed time, as an efficient way for determining the POD basis vectors for large-scale problems [52]. POD has been successfully applied for simulation [53, 54, 55, 56], optimization and optimal control problems [57, 58, 59].

Since the full dynamic system has variable-dependent functions and nonlinear functions, we must choose a suitable model reduction method. The tradi-

9

tional approach is Galerkin method for incompressible flow. In this method, a set of nonlinear systems is approximated using a finite Galerkin expansion in term of global modes, obtained the evolution equation for the mode amplitudes, called the Galerkin system [60]. In the context of optimal control problems, this approach improves the efficiency of computation by simplifying the full and complex optimality system, resulting in a set of nonlinear ordinary differential equations that is simple and easy to solve. This approach has been used successfully in optimal flow control problems [59, 61, 62, 63, 64]. Another approach is the empirical interpolation method (EIM) [65, 66], in which the nonlinear terms are approximated using linear combination of empirical basis functions and interpolation points where both basic functions and interpolation points are computed based on a greedy selection process. Chaturantabut et al. [67, 68] developed the discrete empirical interpolation method (DEIM) based on the EIM method in a finite-dimensional setting. This approach was successfully applied to derive efficient reduced-order models for reacting flow applications [69].

1.3   Thesis Objectives and Outline

The goal of this work is to develop an efficient end-to-end measure-invert-control approach to solve stochastic problems in the application of water quality management. The objectives of the thesis are as follows:

1. To develop a numerical simulation of hydrodynamic processes in lakes and reservoirs.

2. To develop an efficient reduced-order modeling approach to solve an in-

verse problem to estimate an uncertain contaminant source and then solve

a stochastic control problem to mitigate the effects of the contaminant.

As such, this thesis is structured as follows. In Chapter 2, the problem formulations and numerical simulations for lake and reservoir are given. The 2D laterally averaged model is derived from the Navier-Stokes equations and transport equations. Finite element methods together with a turbulence model and stabilization techniques are used to solve the system equations. In Chapter 3, the computer codes are validated, compared and verified using benchmark problems. The 2D lid-driven cavity flow with low and high Reynolds numbers are used to validate the code for the 2D Navier-Stokes equations. The backward facing step flow with higher Reynolds numbers is used to demonstrate the effect of turbulence models. Test cases for transport equations are described and compared with other methods. Chapter 4 presents a model order reduction technique, based on Galerkin projection and POD methods. A general reduction framework for linear system is firstly presented, the Galerkin method is then derived for nonlinear systems. In Chapter 5, stochastic estimation and stochastic control are developed for transport problems. A numerical example is presented to demonstrate how the end-to-end measure-invert-control strategy works for a stochastic problem governed by the transport equations. Chapter 6 concludes the thesis with recommendations for extensions and future work.

Chapter 2

Mathematical model and

Numerical methods

This chapter describes the governing equations and numerical models for hydrodynamic processes such as fluid flow, thermal stratification and contaminant transport in lakes and reservoirs. Section 2.1 describes a laterally averaged model, which is a combination of the Navier-Stokes equations and a transport equation. Section 2.2 presents the fluid properties and transport properties such as water density, dynamic viscosity, eddy viscosity, thermal conductivity and diffusion coefficients. Section 2.3 describes the boundary conditions for the three hydrodynamics processes. Finally, numerical methods for solving the laterally averaged system are presented in Section 2.4.

2.1 Laterally averaged model for lakes and reservoirs

We are interested in simulating the hydrodynamic processes and water quality changes in lakes and reservoirs. Here we consider a 2D laterally averaged model. The model is obtained by laterally integrating the Navier-Stokes equation, continuity equation and transport equation, which can be found in many textbooks (see e.g., Ji [12], Martin [13], Orlob [14], and Rubin and Atkinson [15]). In this study, we employ the non-hydrostatic model to describe the hydrodynamic processes. This model is first used by Karpik and Raithby [70] to predict the thermal stratification in reservoirs. It has been applied widely in reservoir models [71, 72].

We consider a set of governing equations as described in the following. In order to simplify the system for general applications, we first apply dimensionless analysis to the general governing equations. We define dimensional parameters as given in Table 2.1. Let,

$$x = \frac{x^*}{L_0}, \quad z = \frac{z^*}{L_0}, \quad B = \frac{B^*}{B_0}, \quad u = \frac{u^*}{U_0}, \quad w = \frac{w^*}{L_0}, \quad t = \frac{t^*U_0}{L_0}, \quad g = \frac{g^*}{g_0},$$

$$\rho = \frac{\rho^*}{\rho_0}, \quad \mu_x = \frac{\mu_x^*}{\mu_0}, \quad \mu_z = \frac{\mu_z^*}{\mu_0}, \quad \kappa_x = \frac{\kappa_x^*}{\kappa_0}, \quad \kappa_z = \frac{\kappa_z^*}{\kappa_0}, \quad \lambda_x = \frac{\lambda_x^*}{\lambda_0}, \quad \lambda_z = \frac{\lambda_z^*}{\lambda_0},$$

$$p = \frac{p^*}{\rho_0 U_0^2}, \quad \tau_x = \frac{\tau_x^*}{\frac{1}{2}\rho_0 U_0^2}, \quad T = \frac{T^*}{T_0}, \quad c = \frac{c^*}{c_0}, \quad Re = \frac{\rho_0 U_0 L_0}{\mu_0}, \quad Pe = \frac{U_0 L_0}{\kappa_0},$$

$$Fr = \frac{U_0}{\sqrt{g_0 L_0}}, \quad Pr = \frac{c_p \mu_0}{\lambda_0}, \quad R_N = \frac{R_N^*}{R_{N0}}, \quad E_p = \frac{R_{N0}}{\rho_0 c_p U_0 \Delta T_0}.$$

where the superscript '*' indicates dimensional quantity while subscript '0' indicates a constant reference value. We then use these reference values to derive

13

Table 2.1: The dimensional parameters.

Parameter	Description	Original dimensions
L_0	Length scale	$\{L\}$
B_0	Width averaged scale	$\{L\}$
U_0	Velocity scale	$\{Lt^{-1}\}$
P_0	Pressure	$\{ML^{-1}t^{-2}\}$
g_0	Gravitational acceleration	$\{Lt^{-2}\}$
ρ_0	Density	$\{ML^{-3}\}$
μ_0	Dynamic viscosity	$\{ML^{-1}t^{-1}\}$
κ_0	Diffusivity coefficient	$\{ML^{-1}t^{-1}\}$
λ_0	Thermal conductivity	$\{Mt^{-3}\theta^{-1}\}$
T_0	Temperature	$\{\theta\}$
c_0	Contaminant	$\{ML^{-3}\}$
R_{N0}	Radiative heating	$\{Mt^{-3}\}$

the non-dimensional form of the governing equations.

The continuity equation is

$$\frac{\partial(Bu)}{\partial x} + \frac{\partial(Bw)}{\partial z} = 0, \tag{2.1}$$

where $B(x, z)$ is the local width that varies in vertical z and longitudinal x directions, $u(x, z, t)$ and $w(x, z, t)$ are width-averaged velocity components corresponding to x and z directions, respectively, and t is time.

The momentum equations are

$$\frac{\partial u}{\partial t} + u\frac{\partial u}{\partial x} + w\frac{\partial u}{\partial z} = -\frac{1}{\rho}\frac{\partial p}{\partial x} + \frac{1}{Re\,\rho\,B}\left[\frac{\partial}{\partial x}\left(B\mu_x\frac{\partial u}{\partial x}\right) + \frac{\partial}{\partial z}\left(B\mu_z\frac{\partial u}{\partial z}\right)\right]$$
$$+\tau_x, \tag{2.2}$$

$$\frac{\partial w}{\partial t} + u\frac{\partial w}{\partial x} + w\frac{\partial w}{\partial z} = -\frac{g}{Fr^2} - \frac{1}{\rho}\frac{\partial p}{\partial z}$$
$$+\frac{1}{Re\,\rho\,B}\left[\frac{\partial}{\partial x}\left(B\mu_x\frac{\partial w}{\partial x}\right) + \frac{\partial}{\partial z}\left(B\mu_z\frac{\partial w}{\partial z}\right)\right]. \tag{2.3}$$

14

Here $p(x, z, t)$ is pressure, ρ is the width-averaged density, g is the gravitational acceleration. $Re \equiv \frac{\rho_0 U_0 L_0}{\mu_0}$ is the Reynolds number that expresses the ratio of inertial forces to viscous forces. $Fr \equiv \frac{U_0}{\sqrt{g_0 L_0}}$ is the Froude number which is a ratio of inertial forces to gravitational forces. μ_x and μ_z are the longitudinal and vertical viscosity coefficient, respectively. τ_x is shear stress caused by wind on water surface.

The concentration of any constituent of water such as dissolved gases, organic matter, etc., is computed by the width-averaged transport equation as follows

$$\frac{\partial c}{\partial t} + u\frac{\partial c}{\partial x} + w\frac{\partial c}{\partial z} = \frac{1}{Pe}\frac{1}{B}\left[\frac{\partial}{\partial x}\left(B\kappa_x\frac{\partial c}{\partial x}\right) + \frac{\partial}{\partial z}\left(B\kappa_z\frac{\partial c}{\partial z}\right)\right] + S, \quad (2.4)$$

where $c(x, z, t)$ is the concentration of the constituent, and κ_x and κ_z are the longitudinal and vertical diffusivity coefficients. $Pe \equiv \frac{U_0 L_0}{\kappa_0}$ is the Péclet which is a measure of the relative importance of convection to diffusion. S denotes an external sources or sinks.

In principle, we can use equation (2.4) for any water quality variables. For lakes and reservoir study, contaminant transport and thermal stratification processes are important. Hence contaminant c and water temperature T are chosen. The contaminant transport equation is the same as equation (2.4), but we replace S by external body source f_c.

The water temperature equation is written as follows

$$\frac{\partial T}{\partial t} + u\frac{\partial T}{\partial x} + w\frac{\partial T}{\partial z} = \frac{1}{RePr}\frac{1}{B}\left[\frac{\partial}{\partial x}\left(B\lambda_x\frac{\partial T}{\partial x}\right) + \frac{\partial}{\partial z}\left(B\lambda_z\frac{\partial T}{\partial z}\right)\right] + E_p\frac{\partial R_N}{\partial z}.$$
$$(2.5)$$

15

Here $T(x, z, t)$ is temperature, R_N the solar radiation penetrating into the water, and $E_p \equiv \frac{R_{N0}}{\rho_0 c_p U_0 \Delta T_0}$ is the radiative heating coefficient, with R_{N0} being the typical value for radiation heating in temperate latitudes, $R_{N0} = 200 - 250 W/m^2$. ΔT_0 is the change in water temperature. λ_x and λ_z are the longitudinal and vertical thermal conductivity coefficients, which depend strongly on the temperature and pressure. $Pr \equiv \frac{c_p \mu_0}{\lambda_0}$ is the Prandtl number which signifies the ratio of heat transport to momentum transport, where c_p is the specific heat of water.

In order to simplify the system equations (2.1)–(2.5), we make the following assumptions:

- The velocity distribution in the reservoir is affected by the shape of the reservoir. Beside the main flow, there are other currents developing attributed to the specific geometry of the reservoir such as cross section, side walls, etc. These situations are complicated and specific. Thus, we assume that the local width $B^*(x, z)$ is wide and unchanged.

- The longitudinal and vertical viscosity coefficients are slightly different. In this study, they are treated as approximately equal.

- We assume $B \sim 1$, $\mu_x^* \approx \mu_z^* \sim \mu_0$, $\kappa_x^* \approx \kappa_z^* \sim \kappa_0$, $\lambda_x^* \approx \lambda_z^* \sim \lambda_0$ and $\rho \sim 1$.

The dimensionless system of laterally-averaged equations (2.1)–(2.5) governing

incompressible viscous flow can be written as follows:

$$\nabla \cdot \mathbf{u} = 0, \tag{2.6}$$

$$\frac{\partial \mathbf{u}}{\partial t} + \mathbf{u} \cdot \nabla \mathbf{u} = -\nabla p + \nu_v \nabla^2 \mathbf{u} + \mathbf{f}, \tag{2.7}$$

$$\frac{\partial T}{\partial t} + \mathbf{u} \cdot \nabla T = \lambda_v \nabla^2 T + E_p \nabla R_N, \tag{2.8}$$

$$\frac{\partial c}{\partial t} + \mathbf{u} \cdot \nabla c = \kappa \nabla^2 c + f_c. \tag{2.9}$$

Here $\mathbf{u} = [u, w]^T$, $\mathbf{f} = [0, -\frac{1}{Fr^2}g]^T$, $\nu_v = \frac{1}{Re}$, $\lambda_v = \frac{1}{Re\,Pr}$ and $\kappa = \frac{1}{Pe}$.

2.2 Transport and thermal properties

In this section, we shall briefly describe the fluid properties, transport properties and thermal properties that appeared in equations (2.6)–(2.9).

2.2.1 Water temperature

Water temperature $T(^oC)$ is an important variation of water quality because of its direct affect on the aquatic life. There are many factors that influence water temperature such as mixing water, inflow temperature, heat exchange, etc. Among them, solar radiation is a factor that directly affects the water body. Figure 2-1, adapted from [1], shows the compilation of solar component relationships.

Following that the total net heat flux through the water surface R_N^* is calculated by the net all-wave radiation, given by

$$R_N^* = R_{SN} + R_{AN} - R_{BR} - R_C - R_L. \tag{2.10}$$
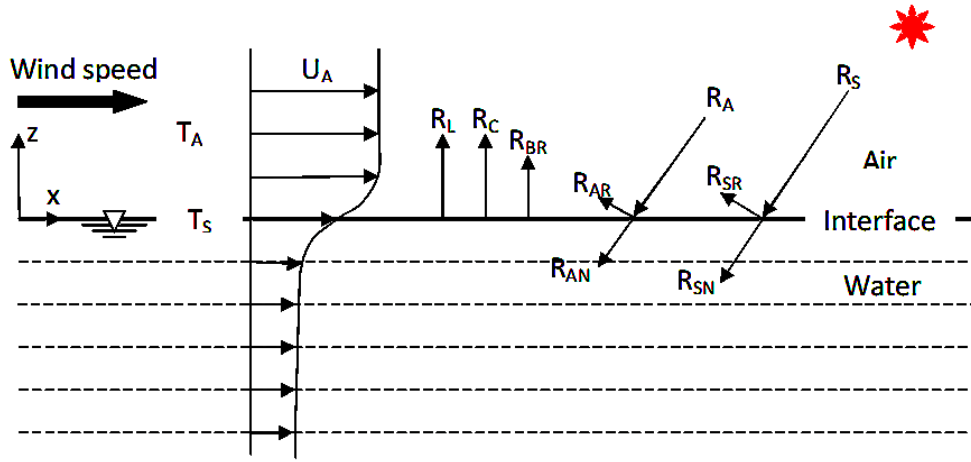
Figure 2-1: The relationship of heat exchange at water surface. Adapted from [1]

Here, R_{SN} is net solar shortwave radiation, R_{AN} is down-welling longwave radiation, R_{BR} is up-welling longwave radiation, R_C is sensible heat flux and R_L is latent heat flux. Details of these radiations can found in Appendix A.1.

2.2.2 Water density

Water density is the mass of water per unit volume. It depends nonlinearly on the temperature, $\rho = f(T)$. Pure water density (kg/m^3) can be calculated using the Thiesen-Scheel-Diesselhorst equation [73].

$$\rho_0 = 1000 \left[1 - \frac{T + 288.9414}{508929.2(T + 68.12963)}(T - 3.9863)^2 \right]. \qquad (2.11)$$

In this empirical formulation, water density will increase its density from 0^oC to 4^oC and decreases its density from 4^oC onwards. As a result, a reservoir in tropical region will stratify the water body in layers where warm water is above and colder water is below.

2.2.3 Dynamic viscosity

Dynamic viscosity is an important water property measuring the resistance to motion. For a Newtonian fluid like water, viscosity is a constant at given temperature. Dynamic viscosity values (Nsm^{-2}) are derived from empirical expressions [73]:

$$\log_{10}\left(\frac{\mu}{100}\right) = \frac{1301}{998.33 + 8.1855(T-20) + 0.00565(T-20)^2}$$
$$- 1.30233 \tag{2.12}$$

$$\log_{10}\left(\frac{\mu}{\mu_{20}}\right) = \frac{1.3272(20-T) - 0.001053(T-20)^2}{T+105}. \tag{2.13}$$

Equation (2.12) is applicable for $T = 0^oC$ to 20^oC, and Equation (2.13) applicable for $T = 20^oC$ to 100^oC. Here μ_{20} is the dynamic viscosity at $20^oC = 0.001002Nsm^{-2}$.

2.3 Boundary conditions

Boundary conditions are different depending on each hydrodynamic process. Common boundary conditions for a reservoir system are shown in Figure 2-2, adapted from [2]. For fluid flow problems, it is necessary to introduce kinematic and dynamic boundary conditions at a free surface. This information is determined locally using a one-dimensional form of the linear wave equation [2]. These boundary conditions will be summarized in this section.

2.3.1 Boundary conditions for fluid flow

Inflow/outflow

In lakes and reservoir problems, we sometimes are not able to determine exactly the inflow boundary conditions because of stochastic water quantity inputs such as rainfalls, flood, tides, etc. These situations are complicated and difficult to deal with. In this study, we shall assume that inflow (or outflow) boundaries are determined. More specifically, at inflow and outflow boundaries, longitudinal velocities are assumed as a parabolic function in z, while vertical velocities are set to zero. That is

$$u_i = f_i(z), \tag{2.14}$$

where subscript 'i' denotes "in" or "out".

Solid surfaces

The bottom and solid-surfaces of reservoir are assumed to be impermeable to fluid and the fluid sticks to their surfaces. Hence, the no-slip boundary condition is applied,

$$u = w = 0. \tag{2.15}$$

Free surface

The free surface boundary conditions include the kinematic boundary condition and dynamic boundary condition.

The kinematic boundary condition

The kinematic boundary condition relates the motions of the free interface to the fluid velocities at the free surface. Let the free surface be defined as $\eta(x, t)$, velocity field $\mathbf{u}(x, z, t) = \nabla\phi(x, z, t)$, the linearized wave kinematic condition is given by [2],

$$\frac{\partial \eta}{\partial t} = \frac{\partial \phi}{\partial z}, \tag{2.16}$$

$$\frac{\partial \phi}{\partial t} + g\eta = 0, \tag{2.17}$$

which are applicable on $z = \eta$. Thus, the complete boundary value problem (BVP) is to find the potential $\phi_w(x, z, t)$ that satisfies

$$\nabla^2 \phi_w = 0,$$

$$s.t. \quad \frac{\partial \phi}{\partial z} = \frac{\partial \eta}{\partial t} \quad \text{on } z = \eta,$$

$$\frac{\partial \phi_w}{\partial t} = -g\eta \quad \text{on } z = \eta,$$

$$\frac{\partial \phi}{\partial z} = 0 \quad \text{on } z = -H,$$

$$\eta = \bar{\eta}\sin(\mathcal{D}t - kx). \tag{2.18}$$

Here $\mathcal{D} = 2\pi/T$, $k = 2\pi/\lambda_w$, $\lambda_w = \frac{g}{2\pi}T^2$, where T is wave period, λ_w wave length, $\bar{\eta}$ wave amplitude, H total depth. A general solution for deep water when $\bar{\eta}/\lambda_w \ll 1$, is

$$u_w = u_s \exp^{kz}\sin(\mathcal{D}t - kx), \tag{2.19}$$

$$w_w = u_s \exp^{kz}\cos(\mathcal{D}t - kx). \tag{2.20}$$

21

Here $u_s = \mathcal{D}\bar{\eta}$ is the velocity amplitude, u_w and w_w are the velocity at free surface in x and z directions.

The dynamic boundary condition

The dynamic boundary condition requires that the stress to be continuous across the free surface which separates the air and water. Wind forcing exerts a drag on water surface is equal and opposite to the traction exerted by water on air. Thus we have

$$\tau_x = C_d \rho_a U_a^2 = C_d \rho u_s^2, \tag{2.21}$$

where τ_x is the wind forcing on water surface, U_a is wind speed at $10m$ above the surface, ρ_a density of air and C_d the wind stress coefficient. Now, u_s can be approximated as

$$u_s = \sqrt{\frac{\rho_a}{\rho}} U_a \approx 0.03 U_a. \tag{2.22}$$
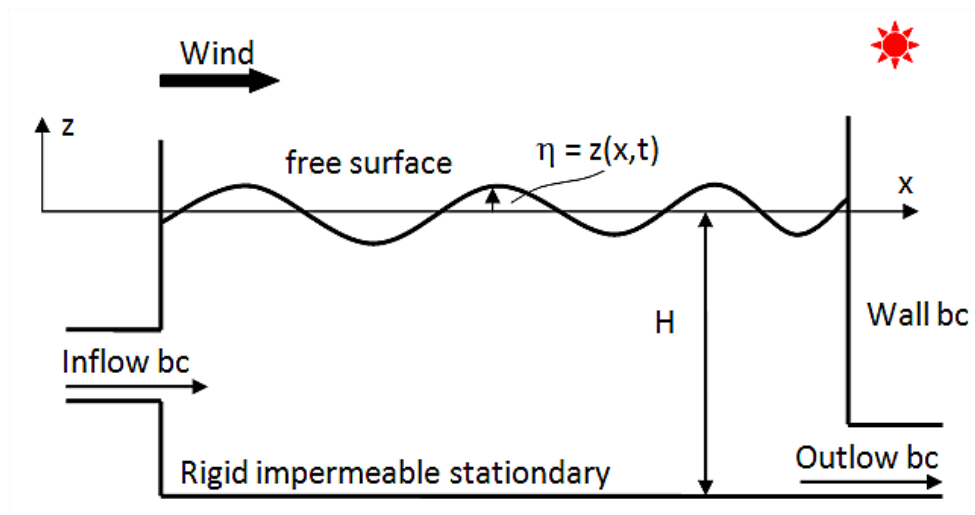
Figure 2-2: Common boundary conditions for reservoir problems. Adapted from [2].

In this study we assume that the lake and reservoir act like a container, meaning that we have a closed water body. The water surface is usually quiescent. Only water velocities and wind-induced water velocity influence the water surface. Water velocities play a key role in the near field and wind induced water velocity is an important factor in the far field. Under these influences, the water surface may have oscillations but with small amplitudes. Overall, these influences are small and do not have a large effect on the entire reservoir. Thus we neglect the kinematic boundary condition.

2.3.2 Boundary conditions for water temperature

Inflow/outflow

Inflow temperature is given as a constant value and outflow temperature satisfy the homogeneous Neumann conditions:

$$T = T_{in} \quad \text{on } \Gamma_{in}, \tag{2.23}$$

$$\frac{\partial T}{\partial \mathbf{n}} = 0 \quad \text{on } \Gamma_{out}, \tag{2.24}$$

where $\mathbf{n}$ is the normal outward vector.

Solid surfaces

In a real reservoir system in a tropical region, the water body will be stratified in layers where warm water is above and colder water is below. In this case, the walls temperature will have the temperature value at that water layer. Here we assume that the bottom of reservoir has a temperature T_b and the surface

water has a temperature T_s. The walls temperature is defined by the temperature linearly decreasing from the surface temperature to the bottom temperature of the reservoir. That is

$$T|_{\text{wall}} = T_s \quad \text{at } z = 0, \tag{2.25}$$

$$T|_{\text{wall}} = T_b \quad \text{at } z = -H, \tag{2.26}$$

where H is average depth of the reservoir.

Free surfaces

Temperature at a free surface is complex because it involves heat exchange at the surface between the atmosphere and water in the reservoir. The boundary temperature at the surface of the water is given by

$$-\rho c_p \lambda \frac{\partial T}{\partial z} = R_{BR} + R_L + R_C. \tag{2.27}$$

Here R_{BR}, R_L and R_C are described in Appendix A.1.

2.3.3 Boundary conditions for contaminant transport

The inflow boundary and other solid boundaries satisfy a homogeneous Dirichlet condition. The outflow boundaries and free surface boundary satisfy homogeneous Neumann condition.

$$c = 0 \quad \text{on } \Gamma_D, \tag{2.28}$$

$$\frac{\partial c}{\partial \mathbf{n}} = 0 \quad \text{on } \Gamma_N. \tag{2.29}$$

2.4 Numerical methods for lateral reservoir system

This section describes the numerical method for solving the system of equations. Here, the mixing length model is briefly described. Then the stabilized second-order fractional-step method is employed to solve for the Navier-Stokes equations. Finally, the finite element method is used to discretize the governing equations in space.

2.4.1 Turbulent models

Many environmental flows are unsteady and turbulent. For large-scale system such as a reservoir, we only want to capture the main characteristics of the flow. Hence, the mixing length turbulence model is suitable for that purpose.

The Reynolds-Averaged Equations in dimensionless form of equations (2.6)–(2.7) are

$$\nabla \cdot \mathbf{u} = 0, \tag{2.30}$$

$$\frac{\partial \mathbf{u}}{\partial t} + \mathbf{u} \cdot \nabla \mathbf{u} = -\nabla p + \nabla \cdot \Big((\nu_v + \nu_t)\nabla \mathbf{u} \Big) + \mathbf{f}, \tag{2.31}$$

where $\mathbf{u}$ is the mean solutions of velocity field and p the mean solution of pressure field. $\nu_v = 1/Re$ with Re is the viscosity Reynolds number, as defined above, $\nu_t = 1/Re_t$ with Re_t is the eddy Reynolds number, defined as $Re_t \equiv \frac{\rho_0 U_0 L_0}{\mu_t}$. Here μ_t is a eddy viscosity. The mixing length model [74] is

then used to determines μ_t. That is,

$$\mu_t = \rho_0 l_m^2 \left| \frac{\partial \mathbf{u}}{\partial z} \right| \quad \text{with } l_m = \begin{cases} \kappa^t z, \ \frac{z}{\delta} \leq \frac{\lambda^t}{\kappa^t} \\[2mm] \lambda^t \delta, \ \frac{z}{\delta} > \frac{\lambda^t}{\kappa^t}. \end{cases} \tag{2.32}$$

Here $\frac{\partial \mathbf{u}}{\partial z}$ is the partial derivative of the stream-wise velocity with respect to the wall normal direction z, l_m is the mixing length, $\kappa^t = 0.41$ and $\lambda^t = 0.09$. δ is the boundary layer thickness.

A similar formulation is derived for the temperature transport equation. If the flow is turbulent, the eddy viscosity is added in to diffusion term as follows

$$\frac{\partial T}{\partial t} + \mathbf{u} \cdot \nabla T = (\lambda_v + \lambda_t) \nabla^2 T + E_p \nabla R_N, \tag{2.33}$$

where $\lambda_t = \frac{1}{Pe_t}$ with Pe_t is eddy Péclet number, defined as $Pe_t \equiv \frac{U_0 L_0}{\lambda_x^T}$. Here λ_x^T is the horizontal eddy viscosity, calculated from the following formula [75]

$$\lambda_x^T = E_t \rho c_t H U_0, \tag{2.34}$$

where H is average depth of the reservoir, $c_t = 2 \times 10^{-5}$. E_t is a constant.

2.4.2 Numerical model for Navier-Stokes equations

As discussed in the boundary section, we wish to solve the fluid flow problem with all Dirichlet conditions applied for the boundaries. Let $\mathcal{D} \in \mathbb{R}^2$ be a physical domain. The Navier-Stokes equations as described in equations (2.30)–

(2.31) with boundary conditions and initial condition are given as

$$\frac{\partial \mathbf{u}}{\partial t} + (\mathbf{u} \cdot \nabla)\mathbf{u} = -\nabla p + \nu \nabla^2 \mathbf{u} + \mathbf{f} \quad \text{in } \mathcal{D} \times [t_0, t_f], \qquad (2.35)$$

$$\nabla \cdot \mathbf{u} = 0 \qquad \text{in } \mathcal{D} \times [t_0, t_f], \qquad (2.36)$$

$$\mathbf{u} = \mathbf{u}_D \qquad \text{on } \Gamma \times [t_0, t_f], \qquad (2.37)$$

$$\mathbf{u}(\mathbf{x}, 0) = \mathbf{u}_0(\mathbf{x}) \qquad \text{in } \mathcal{D}, \qquad (2.38)$$

where $\nu = (\nu_v + \nu_t)$ is the fluid kinematic viscosity, $\mathbf{x} \in \mathcal{D}$ denotes the spatial coordinates, $t \in [t_0, t_f]$ denotes time, and $\mathbf{u}_0$ the initial condition.

In order to solve problem (2.35)–(2.38) we use the pressure stabilized second-order fractional-step method formulation based on the pressure projection. For details discussion and derivation of this method, one may refer to [45, 76]. Here we present the method for this particular problem. Define the algorithmic parameters as follows

$$\tau := \left[4\frac{\nu}{h_e^2} + 2\frac{||\mathbf{u}_h||}{h_e} \right]^{-1} \qquad (2.39)$$

where h_e is the local size of element e, $||\mathbf{u}_h||$ is the local velocity in the element.

Equations (2.35)–(2.38) can be written as follows

$$\frac{\partial \mathbf{u}}{\partial t} + (\mathbf{u} \cdot \nabla)\mathbf{u} = -\nabla p + \nu \nabla^2 \mathbf{u} + \mathbf{f} \quad \text{in } \mathcal{D} \times [t_0, t_f], \quad (2.40)$$

$$-\tau \nabla^2 p + \tau \nabla \cdot \pi + \nabla \cdot \mathbf{u} = 0 \qquad \text{in } \mathcal{D} \times [t_0, t_f], \quad (2.41)$$

$$-\nabla p + \pi = 0 \qquad \text{in } \mathcal{D} \times [t_0, t_f], \quad (2.42)$$

$$\mathbf{u} = \mathbf{u}_D \qquad \text{on } \Gamma \times [t_0, t_f], \quad (2.43)$$

$$\mathbf{u}(\mathbf{x}, 0) = \mathbf{u}_0(\mathbf{x}) \qquad \text{in } \mathcal{D}, \qquad (2.44)$$

where π the projection of pressure.

Finite Element Approximations

Finite element method (FEM) [77] is employed to discretize equations in space. Finite element formulation requires solutions of the weak formulation of (2.40)-(2.44). The weak formulation is obtained based on the variational formulation of the problem. In order to satisfy the Dirichlet boundary condition, for a fixed $t \in [t_0, t_f]$, the weak solutions of the velocity space $\mathcal{V} := \{\mathbf{u}, \mathbf{v}, \mathbf{w} \in \mathcal{H}_0^1(\mathcal{D})\}$, pressure space $\mathcal{Q} := \{q \in L^2(\mathcal{D})\}$ are chosen. Introduction of the bilinear forms is given as follows

$$a(\mathbf{u}, \mathbf{v}) := (\nabla \mathbf{u}, \nabla \mathbf{v}), \tag{2.45}$$

$$b(q, \mathbf{v}) := (q, \nabla \cdot \mathbf{v}), \tag{2.46}$$

$$c(\mathbf{u}, \mathbf{v}, \mathbf{w}) := \left(\mathbf{u} \cdot \nabla \mathbf{v}, \mathbf{w} + \frac{1}{2}((\nabla \cdot \mathbf{u})\mathbf{v}, \mathbf{w})\right), \tag{2.47}$$

$$s(\mathbf{u}, \mathbf{v}) := (\mathbf{u}, \mathbf{v}). \tag{2.48}$$

where $(\mathbf{u}, \mathbf{v}) = \int_{\mathcal{D}} \mathbf{u}\mathbf{v} \, d\mathcal{D}$ denotes the standard L^2 inner product.

For finite element space $\mathcal{V}_h \in \mathcal{V}$, $\mathcal{Q}_h \in \mathcal{Q}$, the discretization of the weak formulation can be defined as: find the approximation $(\mathbf{u}_h^{n+\theta}, \pi_h^{n+\theta}, p_h^n)$ to $(\mathbf{u}_h^{n+1}, \pi_h^{n+1}, p_h^{n+1})$

such that

$$s(\frac{\delta \mathbf{u}_h^n}{\delta t}, \mathbf{v}_h) + c(\mathbf{u}_h^{n+\theta}, \mathbf{u}_h^{n+\theta}, \mathbf{v}_h) + \nu a(\mathbf{u}_h^{n+\theta}, \mathbf{v}_h) = b(p_h^n, \mathbf{v}_h)$$

$$+ s(\mathbf{f}^{n+1}, \mathbf{v}_h) \quad (2.49)$$

$$-dts(\nabla(p_h^{n+1} - p_h^n), \nabla q_h) - \tau s(\nabla p_h^{n+1} - \pi_h^n, \nabla q_h) = b(q_h, \mathbf{u}_h^{n+\theta}), \quad (2.50)$$

$$s(\frac{\delta \mathbf{u}_h^{n+\theta}}{\delta t}, \mathbf{v}_h) - b(p_h^{n+1} - p_h^n, \mathbf{v}_h) = 0, \quad (2.51)$$

$$\nu a(\pi_h^{n+1}, q_h) = \nu a(\nabla p_h^{n+1}, q_h) \quad (2.52)$$

Here δt is the time step size, superscripts refer to the time step level, $\theta \in [0, 1/2, 1]$, $\mathbf{u}_h^{n+\theta} := \theta \mathbf{u}_h^{n+1} + (1 - \theta)\mathbf{u}_h^n$ and $\delta \mathbf{u}_h^n := \mathbf{u}_h^{n+\theta} - \mathbf{u}_h^n$.

The second-order fractional-step algorithm

The second-order fractional-step method need three steps to solve the system of equations (2.49)–(2.52). We introduce the finite element matrices to the form of the system with $\theta = 1/2$. The fundamental formulation of finite element method is provided in Appendix A.2.1. The algorithm is,

1. Determine the intermediate velocity fields

$$\mathbf{M}\frac{\delta \mathbf{u}^n}{dt} + \Big(\mathbf{C}(\mathbf{u}^n) + \mathbf{K}(\mathbf{u}^n)\Big)\mathbf{u}^{n+1/2} = -\mathbf{G}p^n + \mathbf{f} \quad \text{in } \mathcal{D}, \quad (2.53)$$

$$\mathbf{u} = \mathbf{u}_D \quad \text{on } \Gamma. \quad (2.54)$$

2. Update pressure

$$-\mathbf{L}p^{n+1} = \sum_{e=1}^{N_{nel}} \frac{1}{dt+\tau_k}\left(-dt\mathbf{L}^e p^e + \mathbf{A}^e(\mathbf{u}_e^{n+1/2}) - \tau_k\mathbf{D}^e(\boldsymbol{\pi}_e^n)\right), \quad (2.55)$$

$$\mathbf{n}\cdot(\mathbf{L}p^{n+1}) = 0 \qquad\qquad \text{on } \Gamma. \qquad\qquad (2.56)$$

Equation (2.56) is the homogenous Neumman boundary conditions [78]. In addition, the pressure at given point is fixed. Here N_{nel} is the number of element. Note that we need to compute τ_k in each element because τ_k is discontinuous across the element.

3. Update projected pressure and velocity

$$\mathbf{M}\boldsymbol{\pi}^{n+1} = \mathbf{G}p^{n+1} \qquad\qquad \text{in } \mathcal{D}, \qquad (2.57)$$

$$\mathbf{M}\mathbf{u}^{n+1} = \mathbf{M}\mathbf{u}^{n+1/2} - dt\mathbf{G}(p^{n+1} - p^n) \quad \text{in } \mathcal{D}, \qquad (2.58)$$

$$\mathbf{n}\cdot\mathbf{u}^{n+1} = \mathbf{n}\cdot\mathbf{u}_D \qquad\qquad \text{on } \Gamma. \qquad (2.59)$$

These elemental matrices are given in Appendix A.2.2. For computational procedure, we assemble the matrices $\mathbf{M}, \mathbf{L}, \mathbf{G} = [\mathbf{G}_x\ \mathbf{G}_z]$ and $\mathbf{f} = [\mathbf{f}_x\ \mathbf{f}_z]^T$ before the transient analysis. Then we assemble the matrices $\mathbf{K}, \mathbf{C}, \mathbf{A}, \mathbf{D}$ at each time step. The computation will stop when it meets the convergence requirements. Let ε_u be the tolerance interior, and the relative error at each time step is given by

$$\text{error} = \frac{||\mathbf{u}^{n+1} - \mathbf{u}^n||_{L_2}^2}{||\mathbf{u}^{n+1}||_{L_2}^2} < \varepsilon_u. \qquad\qquad (2.60)$$

2.4.3 Numerical model for transport equations

In general, a transport equation has the form of (2.9). In order to represent the stochastic processes which appear in realistic applications, we introduce stochastic variables into the governing equation. Let the diffusivity $\kappa(\mathbf{x}, t; \omega)$ be a function mapping the product space $\mathcal{D} \times [t_0, t_f] \times \Omega \to \mathbb{R}$, where $\mathbf{x} \in \mathcal{D}$ denotes the spatial coordinates and $t \in [t_0, t_f]$ denotes time. The randomness of the diffusivity is contained in $\omega \in \Omega$, where Ω is the sample space. A contaminant concentration which is represented by a function $c :\equiv c(\mathbf{x}, t; \omega)$ satisfies the stochastic parabolic differential equation (SPDE), boundary conditions and initial conditions as follows:

$$\frac{\partial c}{\partial t} + \mathbf{u} \cdot \nabla c - \nabla \cdot \big(\kappa(\mathbf{x}, t; \omega)\nabla c\big) = f_c(\mathbf{x}, t; \boldsymbol{\phi}) \quad \text{in } \mathcal{D} \times [t_0, t_f], \quad (2.61)$$

$$c = c_D \qquad \text{on } \Gamma_D \times [t_0, t_f], (2.62)$$

$$\frac{\partial c}{\partial \mathbf{n}} = 0 \qquad \text{on } \Gamma_N \times [t_0, t_f], (2.63)$$

$$c(\mathbf{x}, t_0; \omega) = c_0(\mathbf{x}; \omega) \qquad \text{in } \mathcal{D}. \qquad (2.64)$$

Here $f_c(\mathbf{x}, t; \boldsymbol{\phi})$ is the external source with $\boldsymbol{\phi} \in \mathbb{R}^2$ are source locations, and c_0 is the given initial condition. The inlet boundary Γ_D is subjected to a Dirichlet condition c_D, while the remainder of the boundary $\Gamma_N = \Gamma \setminus \Gamma_D$ satisfies homogeneous Neumann condition. The velocity field $\mathbf{u} \in \mathbb{R}^2$ in the convective term can be a function of $\mathbf{x}$ and t or constant.

Next we use the finite element method together with stochastic collocation approach to discretize this system of equations in space.

31

Stochastic Collocation Method

In the collocation framework, the SPDE problem is transformed into a parameterized family of deterministic PDEs using an assumption of finite-dimensional noise [41, 79]. The approximation of the SPDE solution is then computed based on a weighted combination of the solutions at each sample in the collocation space.

In order to solve the SPDE problem using collocation method, we assume that the randomness ω can be modelled by a set of finite number of random variables. Thus the uncertain diffusivity field κ can be written as $\kappa(\mathbf{x}, t; \omega) \approx \kappa\big(\mathbf{x}, t; \mathbf{Y}(\omega)\big)$, where $\mathbf{Y}(\omega) = \{Y_i(\omega)\}_{i=1}^{N_Y}$ are independent random variables. We define a finite dimensional subspace or a collocation space as the space of degree $P - 1$ polynomials, $\mathbb{P}^{P-1}(\boldsymbol{\theta})$. The collocation space has two attributes: the collocation points $\{\boldsymbol{\theta}^k\}_{k=1}^P$ and the collocation weights $\{w^k\}_{k=1}^P$. We then represent κ as

$$\kappa(\mathbf{x}, t; \mathbf{Y}) = \mathbb{E}\big[\kappa\big](\mathbf{x}, t) + \sum_{i=1}^{N_Y} \kappa_i(\boldsymbol{\theta}) Y_i(\omega). \qquad (2.65)$$

Here the functions κ_i are deterministic functions and $\boldsymbol{\theta}$ represents the coordinates in the collocation space. The expansion in Equation (2.65) could be computed for example using the Karhunen-Loève decomposition [80]. The uncertain diffusivity field κ in Equation (2.65) can be considered as functions of variable $\boldsymbol{\theta}^k$ if the random vector $\mathbf{Y}(\omega)$ is given. As a result, the stochastic collocation requires evaluation of the solution $c(\mathbf{x}, t; \mathbf{Y})$ at each collocation point $\{\boldsymbol{\theta}^k\}_{k=1}^P$. Hence, the SPDE problem with an uncertain input parameter is now

written as a deterministic parameterized PDE where $\boldsymbol{\theta}$ is the input parameter. The solution of the SPDE is a global approximation constructed by linear combination of the solution at collocation points.

$$c_F(\mathbf{x}, t; \mathbf{Y}) = \sum_{k=1}^{P} c_k(\mathbf{x}, t; \mathbf{Y}) L_k(\boldsymbol{\theta}), \tag{2.66}$$

where $L_k(\boldsymbol{\theta})$ is the Lagrange interpolation function corresponding to the kth collocation point, and $c_k(\mathbf{x}, t; \mathbf{Y}), k = 1, \cdots, P$, are the solutions to:

$$\frac{\partial c_k}{\partial t} + \mathbf{u} \cdot \nabla c_k - \nabla \cdot \left(\kappa(\boldsymbol{\theta}^k)\nabla c_k\right) = f_c(\mathbf{x}, t; \boldsymbol{\phi}) \quad \text{in } \mathcal{D} \times [t_0, t_f], \tag{2.67}$$

$$c_k = c_D \qquad \text{on } \Gamma_D \times [t_0, t_f], \tag{2.68}$$

$$\frac{\partial c_k}{\partial \mathbf{n}} = 0 \qquad \text{on } \Gamma_N \times [t_0, t_f], \tag{2.69}$$

$$c_k(\mathbf{x}, t_0; \boldsymbol{\theta}^k) = c_0(\mathbf{x}; \boldsymbol{\theta}^k) \qquad \text{in } \mathcal{D}. \tag{2.70}$$

Finite Element Approximations

The finite element method (FEM) [77] is employed to obtain a semi-discrete set of equations with the following form

$$\mathbf{M}\dot{\mathbf{c}} + \left(\mathbf{C}_c(\mathbf{u}) + \mathbf{K}_c(t; \boldsymbol{\theta}^k)\right)\mathbf{c} = \mathbf{f}_c(t; \boldsymbol{\phi}), \tag{2.71}$$

$$\mathbf{c}(t_0; \mathbf{Y}) = \mathbf{c}_0(\mathbf{Y}). \tag{2.72}$$

Here, $\mathbf{c}(t; \mathbf{Y}) \in \mathbb{R}^N$ is the discretized approximation of $c(\mathbf{x}, t; \mathbf{Y})$ and contains N state unknowns. $\dot{\mathbf{c}}$ is the derivative of $\mathbf{c}$ with respect to time. $\mathbf{M} \in \mathbb{R}^{N \times N}$ is the mass matrix, $\mathbf{C}_c(\mathbf{u}) \in \mathbb{R}^{N \times N}$ is the convective matrix, $\mathbf{K}_c(t; \boldsymbol{\theta}^k) \in \mathbb{R}^{N \times N}$

is the stiffness matrix, and $\mathbf{f}_c(t; \boldsymbol{\phi}) \in \mathbb{R}^N$ is the external source. Here, N is the number of grid points and $\boldsymbol{\theta}^k$ the kth collocation point.

Chapter 3

Code Verification and Validation on Benchmark Problems

In this chapter, our numerical models are validated, compared and verified using benchmark problems. In Section 3.1, a two-dimensional (2D) lid-driven cavity flow without gravity in the range of Reynolds numbers from $Re = 100$ to $Re = 5000$ is used to validate our codes for the 2D Navier-Stokes equations. Numerical results are in good agreement with those obtained from the study of Ghia et al. [81]. In Section 3.2, the backward facing step flow with $Re = 132,000$ is used to demonstrate the effect of turbulence model at high-Reynolds number. Numerical results are compared with the study found in [82, 83, 84]. In Section 3.3, three test cases for transport equations are described. Numerical results are compared with the other finite difference methods in [85, 86, 87]. Finally, numerical simulations of two-dimensional hydrodynamics processes are presented in Section 3.4.

3.1 Cavity flows

We consider the benchmark problem: lid-driven cavity flow at $Re = 100$, $Re = 1000$ and $Re = 5000$ and compared with Ghia et al. [81]. The problem set up is shown in Figure 3-1. Triangular equal-order velocity/pressure elements are
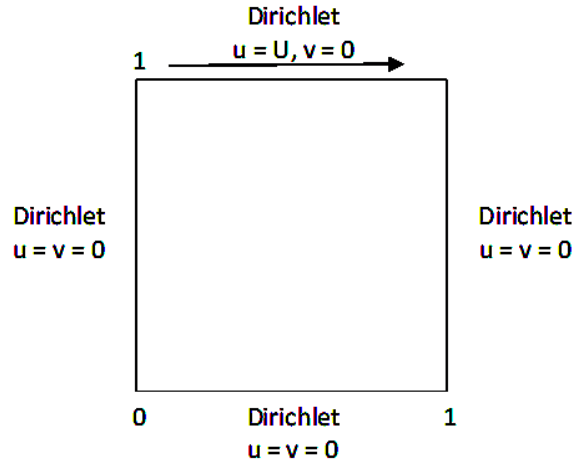
Figure 3-1: Cavity flow set up and boundary.

used to generate the grid. The number of grid points in the x and y directions are $n_x = 60$ and $n_y = 60$, respectively or $N = 3721$. The Crank-Nicolson method [88] (with $\theta = 1/2$) is used to discretize the system equations in time, where $t \in [t_0, t_f]$ with $t_f = 100$ and time step size $\Delta t = 0.08$. The steady solution is obtained when convergence condition (2.60) is satisfied, where the tolerance tol $= 1.0e^{-4}$ is chosen. Figure 3-2 shows the convergence of our computations. We observe that when the Reynolds number is 100, 1000 and 5000, the computed solutions reach the steady solutions but with different computational time. In case $Re = 100$, steady solution reaches very fast while in case $Re = 5000$, the steady solution needs longer time.

Figure 3-3 shows the velocity profiles in the centerline of the cavity at vari-

36
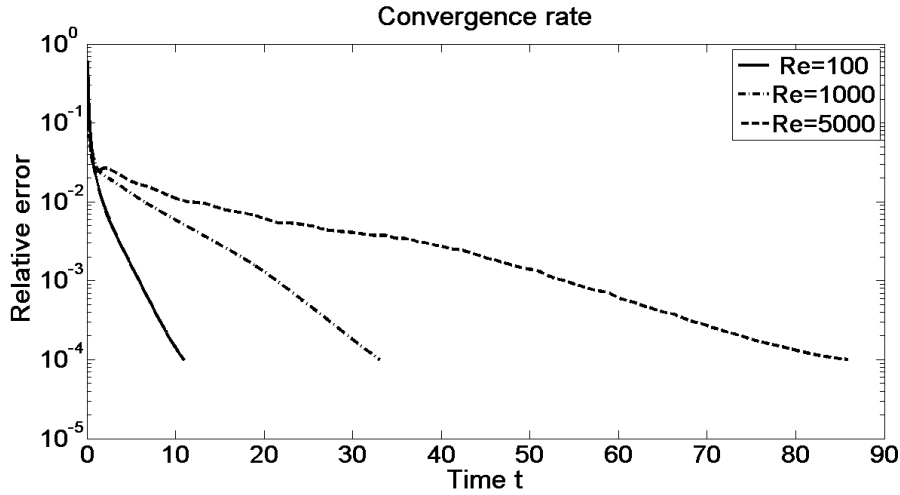
Figure 3-2: Convergence rate of the solutions for various Reynolds numbers.

ous Reynolds numbers. Numerical results are matched with Ghia et al. (1982) results.

3.2 Backward facing step flows

The purpose of this test case is to provide a validation for the mixing length model (which is described in Chapter 2). The fully turbulent flow past a backward-facing step is set up for the $3 : 2$ expansion ratio and Reynolds number $Re = 132,000$. We compare with the available results in the literature [82, 83, 84]. The geometry is given as in Figure 3-4, with $-5 \leq x \leq 22$ and $-1 \leq y \leq 2$. Boundary conditions are set as follows:

$$\text{Inlet}: \begin{cases} u = 1 \\ v = 0 \end{cases} \text{if} \begin{cases} x = -5 \\ 0 \leq y \leq 2, \end{cases} \qquad \text{Outlet}: \begin{cases} \frac{\partial u}{\partial x} = 0 \\ v = 0 \end{cases} \text{if} \begin{cases} x = 22 \\ -1 \leq y \leq 2. \end{cases}$$

Walls are set to the no-slip boundary condition. Triangular equal-order velocity/pressure elements are used to generate the grid with $N_{elem} = 9728$ elements

37
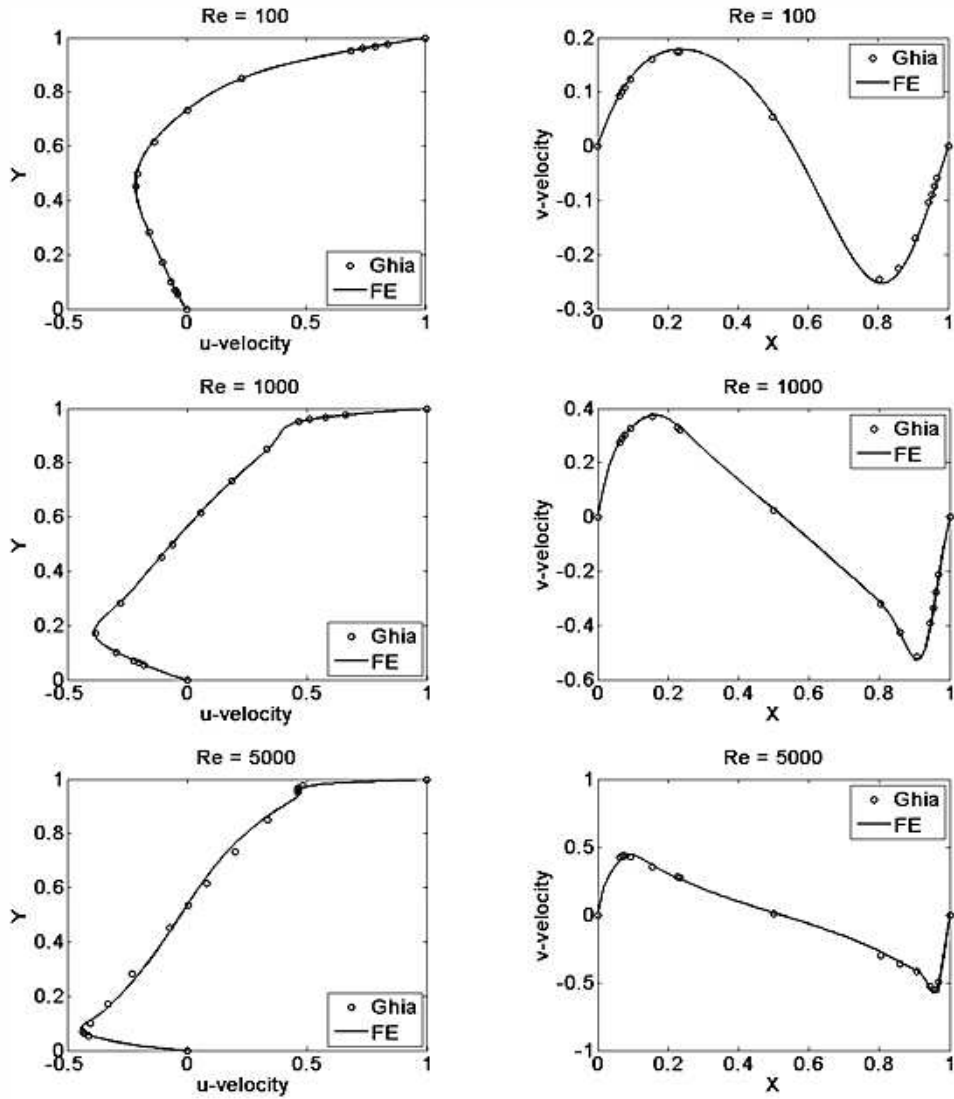
Figure 3-3: Comparison of central profile of velocity.
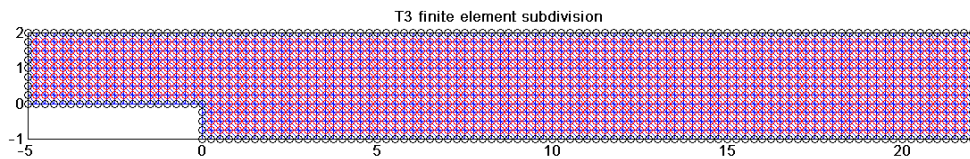
Figure 3-4: Geometry and mesh of backward step.

and $N = 5105$ nodes. Computational time is set at $t_f = 100$ with time step size $\Delta t = 0.05$. The turbulent viscosity μ_t is computed based on equation (2.32). Here, we set the boundary layer thickness $\delta = 0.85$. The computed results of streamlines and mean velocity profiles are presented in Figure 3-5.

(a) Streamlines

(b) Mean velocity profiles
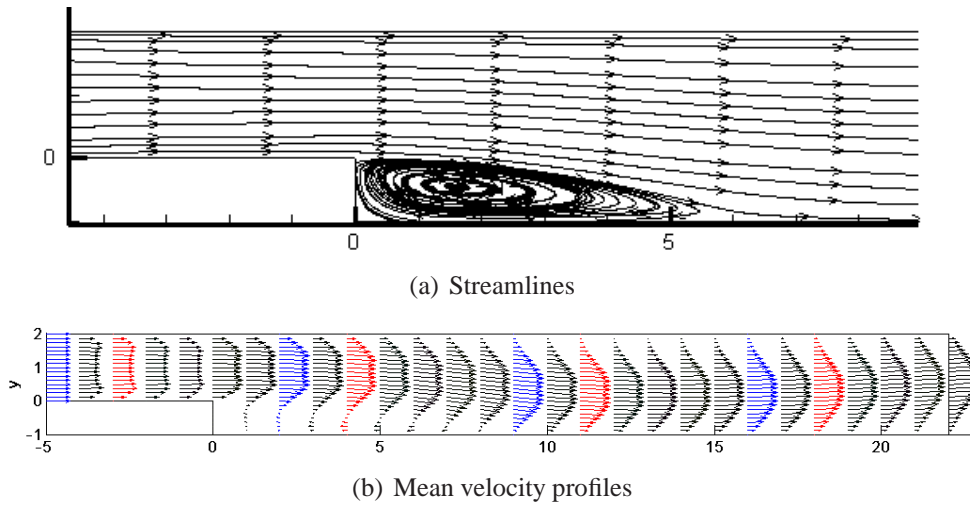
Figure 3-5: Computed results from mixing length turbulent model.

Figure 3-5 indicates that the mean reattachment point is around 6.3, which is close to the experimental value of about 7.0 in Kim et al. [82]. The value in the study of Thangam and Hur [84] is 5.58 and Speziale et al. [83] is 5.5 to 6.4 corresponding with the specific turbulence model adopted. Note that the results in [83, 84] are based on the more complex $k - \epsilon$ model.

Figure 3-6 shows the comparison of the mean velocity profiles with experimental results. In this figure, the solid line is numerical result and the symbol represents the experimental data; H is the height of step. We observe that the computed results with the mixing length model have good agreement with experimental data. When $\frac{\partial \mathbf{u}}{\partial y} = 0$ at the boundary, the eddy viscosity $\mu_t = 0$, which is why the solid line always starts at value 0. It is a shortcoming of the mixing length model. However for large-scale problems such as a lake or reservoir, it is not necessary to capture all the small characteristics of flows. Thus, the mixing length model is suitable for our study purpose.
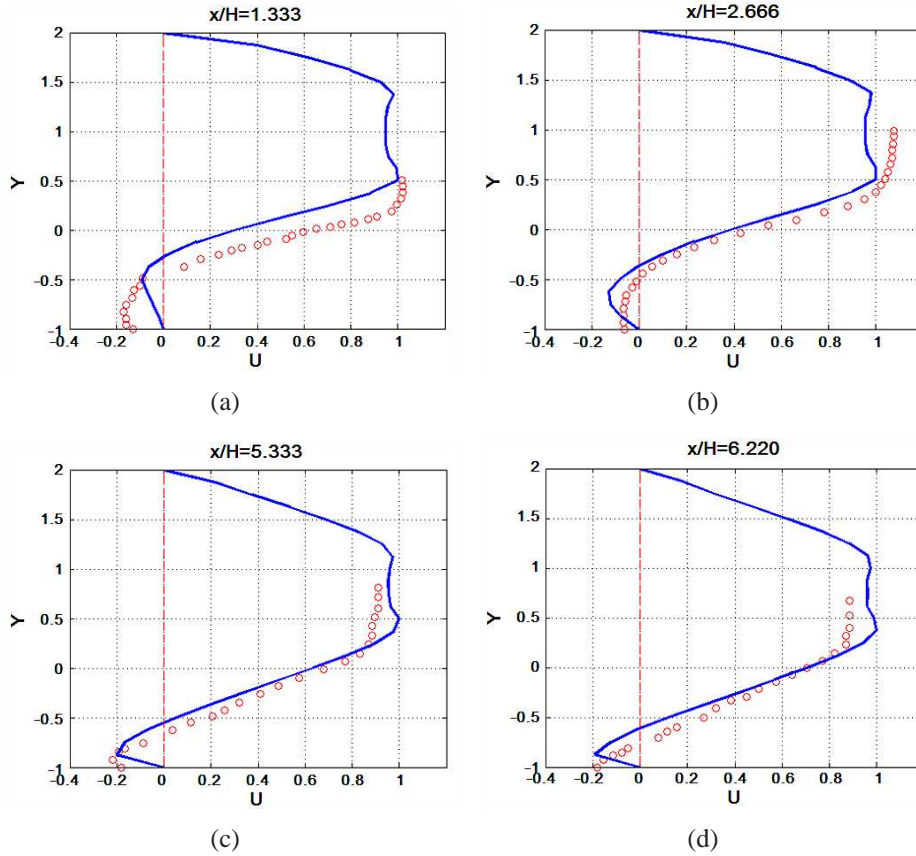
Figure 3-6: Comparison of mean velocity profiles with experimental results.

3.3 Validation of code for transport equation

In this section, we provide some numerical examples to verify our codes for the convection-diffusion equations, which are described in Chapter 2. We shall consider two test cases. First we present a numerical solutions of a pure diffusion equation. Second, a convection-diffusion flow is presented.

3.3.1 Pure diffusion equation

The first test case is equation (2.61) in the unit square domain $\mathcal{D} = [0, \ 1] \times [0, \ 1]$ with the coefficients $\mathbf{u} = 0$, $f_c = 0$ and $\kappa = 1$. It will result the Péclet number $Pe = 0$. The equation is a pure diffusion equation, whose exact solution is given

by

$$c_{exact}(\mathbf{x}, t) = e^{-2\pi^2 t} \sin(\pi x) \sin(\pi y). \tag{3.1}$$

The initial and Dirichlet conditions can be obtained directly from equation (3.1). Triangular elements are used to generate the grid. The number of grid points in the x and y directions are $n_x = 40$ and $n_y = 40$, respectively or $N = 1681$. Computational time is set at $t_f = 1$ with time step size of $\Delta t = 0.001$. Figure 3-7 shows the initial and final computed solutions. In the pure diffusion, the contaminant spreads out and decreases in magnitude gradually.

(a) Initial time   (b) Final time
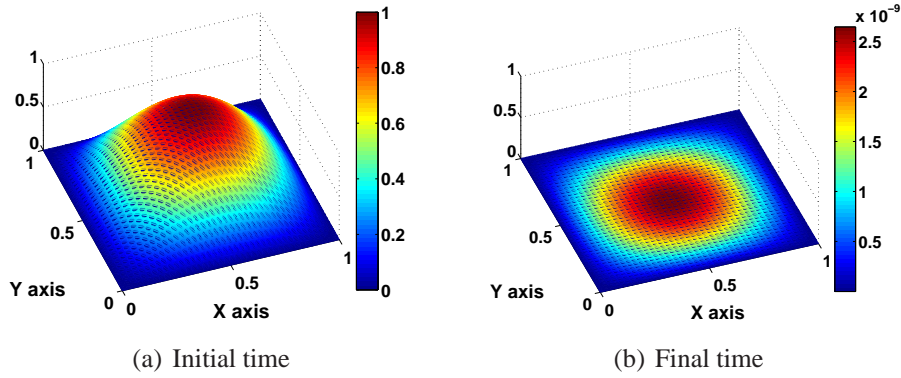
Figure 3-7: Contaminant solutions.

To further illustrate the effectiveness and validity of the codes, we compare our computed result with the results of other numerical methods (Finite Difference Method approach) such as the Peaceman-Rachford ADI (P-R ADI) scheme [87] and Karaa and Zhang ADI (HOC ADI) scheme [85]. In Figure 3-8 we plot the L_2-norm errors at each time step. The error obtained by the standard FEM is in the range of the error bounds.
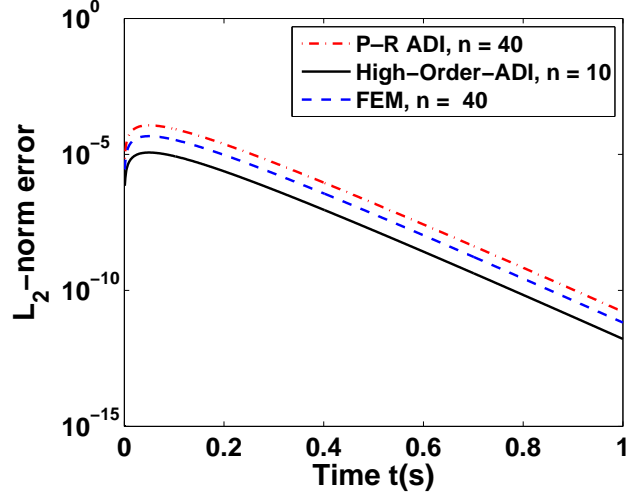
Figure 3-8: Comparison of the L_2-norm errors at each time step.

3.3.2 Convection-diffusion equation

The second test case is based on Noye and Tan [86]. We consider equation (2.61) in a square domain $\mathcal{D} = [0, \ 2] \times [0, \ 2]$ with coefficients $\mathbf{u} = [u \ v]^T = [0.8 \ 0.8]^T$, $f_c = 0$ and $\kappa = 0.01$ or $Pe = 226$. An exact solution of the problem is given by

$$c_{exact}(\mathbf{x}, t) = \frac{1}{4t+1} \exp \left(- \frac{(x - ut - 0.5)^2}{\kappa(4t+1)} - \frac{(x - vt - 0.5)^2}{\kappa(4t+1)} \right). \quad (3.2)$$

The initial condition of this problem is obtained by setting $t = 0$ in equation (3.2). It is the two dimensional Gaussian, pulse located at $x_c = 0.5$ and $y_c = 0.5$, with a strength of value 1. The Dirichlet conditions are set to zero for all sides of the square. Triangular elements are used to generate the grid. The number of grid points in the x and y directions are $n_x = 80$ and $n_y = 80$, respectively or $N = 6561$. Computation time is set at $t_f = 1.25$ with time step size of $\Delta t = 0.00625$.

42
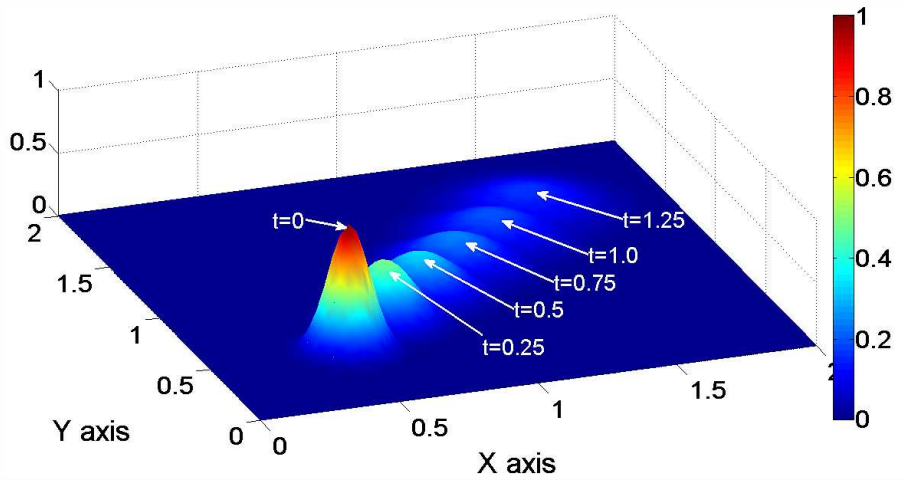
Figure 3-9: Contaminant solutions. Each peak is equidistant by $dt = 0.25$.

Figure 3-9 shows the computed solutions during the simulation in 3D viewing, where Z axis shows the magnitude of contaminant. Contaminant starts at (x_c, y_c), then moves away and spreads out due to the convective and diffusive term. Finally, a small amount of contaminant remains at region $[1, 2] \times [1, 2]$ when $t = 1.25$. Figure 3-10 shows contour plots of the exact and computed so-

(a) Exact
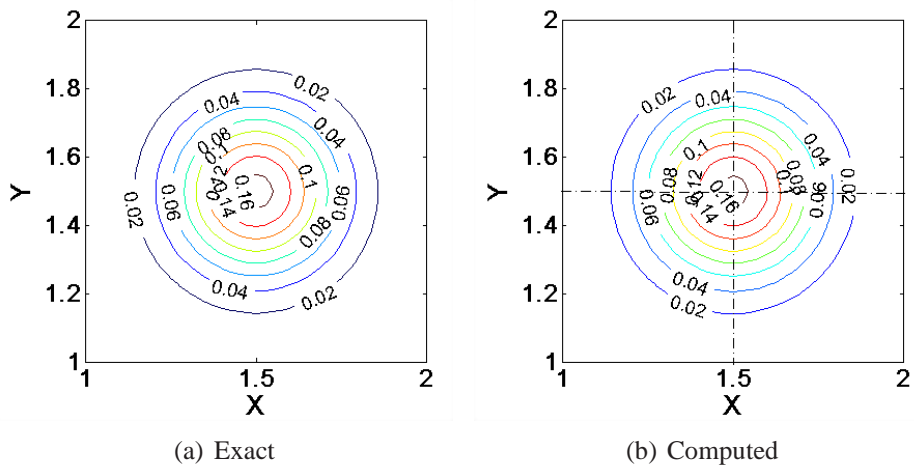
(b) Computed

Figure 3-10: Contour plots of the pulse in the sub-region $1 \leq x, y \leq 2$ at $t = 1.25$.

lutions at the final time. The computed solutions (Figure 3-10(b)) show that the FEM code captures well the moving Gaussian pulse. Contour levels and pulse

centered at final time match as well as the analytical solution (Figure 3-10(a)). Furthermore, the relative L_2-norm error between the computed and exact solution is $7.535e^{-4}$ which is reasonable in comparison with results in [86].

In summary, the verification and validation of codes for solving the Navier-Stokes equations and convection-diffusion equations had been done. The test cases show that our codes are reasonable to do the simulations of the real-systems. In the next section, we will use the codes to simulate 2D hydrodynamics processes.

3.4 Numerical simulations for 2D hydrodynamic processes

In this section, a small-scale model of a 2D laterally averaged reservoir is considered. This model is suitable for the hydrodynamic process study and optimal control study purposes.

3.4.1 Model set up

The physical domain is illustrated in Figure 3-11, which represents a simplified model of a 2D lateral reservoir system.

The reservoir system includes a main reservoir section stretched in longitudinal and vertical directions and the river connections or canals. In our model, inflow boundary is at the top-left corner, while the two outlets with gate-controllers are located on the right boundary. The remaining are solid-surface boundaries (i.e. walls and bottom-bed) and free surface. We assume that the contaminant
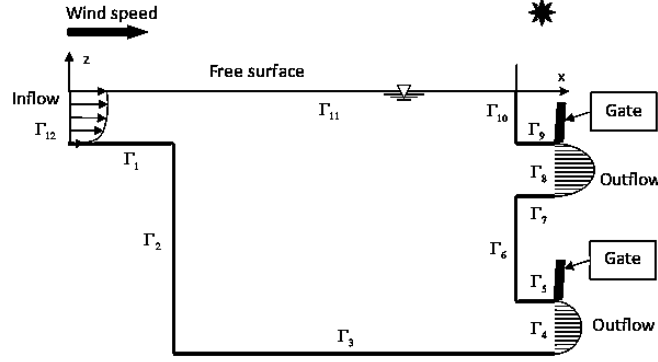
Figure 3-11: The physical domain of 2D reservoir.

will exist within the main reservoir section and the contaminant transport processes are mainly affected by the inflow and wind velocity. Heat radiation is the main source of heat exchange at the surface. For convenience in computation, we assume that averaged water temperature is around $20^0 C$. Based on equations (2.12)–(2.13) we can then determine the dynamic viscosity μ and also the Reynolds number.

The spatial domain is discretized by finite element mesh, as shown in Figure 3-12, with the total number of grid points $N = 2121$ and the total number of elements $N_{elem} = 4000$. The computational time is from $t_0 = 0$ to $t_f = 40$, with time-step size $\Delta t = 0.08$, so the number of time steps $T = 500$. We also placed $N_o = 16$ sensors located on an 4×4 uniform grid covering the reservoir section.

3.4.2 Velocity field and pressure field

A time-dependent velocity field is obtained from the 2D lateral averaged system, which is given in Equations (2.35)–(2.38), where the body force $\mathbf{f} = [f_x \ f_z]^T = [0 \ g]^T$ with g being the gravitational acceleration.
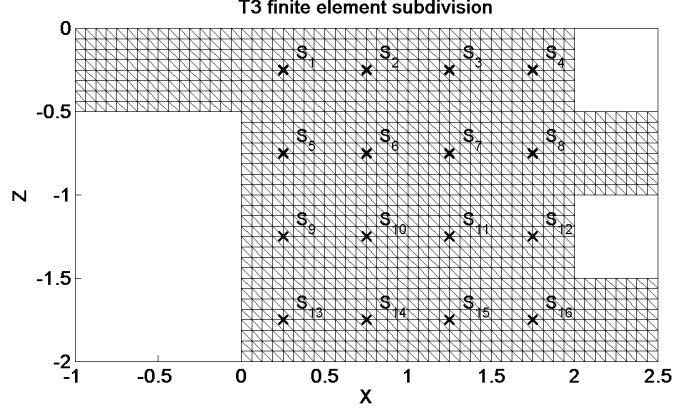
Figure 3-12: The computational domain with $N_o = 16$ sensors.

The boundary conditions are set up as follows

$$(u, w) = (1, 0) \quad \text{on } \Gamma_{12}, \tag{3.3}$$

$$(u, w) = \left(-16 * (2.0 + z) * (1.5 + z), 0 \right) \quad \text{on } \Gamma_4, \tag{3.4}$$

$$(u, w) = \left(-16 * (1.0 + z) * (0.5 + z), 0 \right) \quad \text{on } \Gamma_8, \tag{3.5}$$

$$(u, w) = (0.03 V_a, 0) \quad \text{on } \Gamma_{11}, \tag{3.6}$$

$$p = 0 \quad \text{on } \Gamma_{11} \tag{3.7}$$

The velocity on the remaining boundaries is set to zero. Here, V_a is the wind speed at $10m$ above the water surface. In this example, we assumed that $V_a = 2m/s$ for the whole simulation time. We make an assumption that the changing of free water surface is small and does not influence the simulations. Thus we can ignore the kinematic boundary condition. The Reynolds number is $Re = 1.0 \times 10^6$, the turbulence model (the mixing length model in this case) is used to approximately model the effects of turbulence.

Figure 3-13 shows the pressure field at $t = 40$. Under the gravitational ef-

46

fect, pressure field has stratification and is good agreement with the hydrostatic pressure. Let us take a look at the hydrostatic pressure as a function of depth (h) [89] and given as

$$dp = \rho g dh. \tag{3.8}$$

Here density ρ considered to be a constant, the hydrostatic pressure is obtained by integrating equation (3.8) from h to the free surface, where at $h_0 = 0$ and $p_0 = p_{atm}$ pressure in the atmosphere. We have therefore

$$p = p_{atm} + \rho g H. \tag{3.9}$$

In our computation, we assume $p_{atm} = 0$ (as in equation (3.7)) and with the total depth $H = 2$, the bottom hydrostatic pressure is $p = 19.62 kPa$.
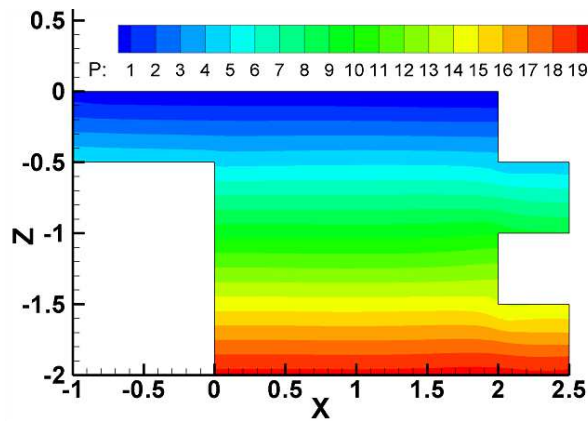
Figure 3-13: Pressure field at $t = 40$.

Figure 3-14 shows velocity fields of reservoir at $t = 40$. Because of the long wall after the inflow, the circulation at this corner is large and strong. This situation will lead to potentially bad water quality because of the agglomeration of the contaminant concentrations.
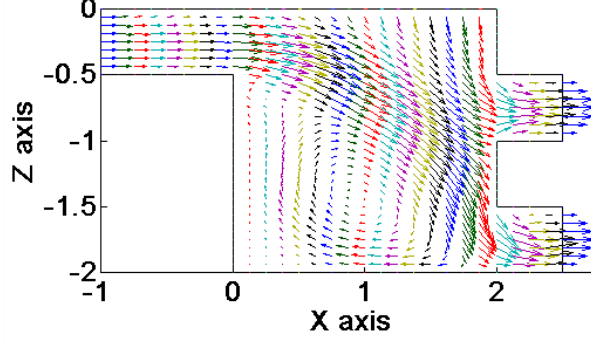
Figure 3-14: Velocity field at $t = 40$.

3.4.3 Temperature field

In water the specific heat is $c_p \cong 1 J/g^0 C$ and the Prandtl number has a fixed value $Pr = 7.0$. So the thermal Péclet has a value $Pe_T = Re \cdot Pr = 7.0 \times 10^6$. It has strong thermal dominance. As such, the thermal-stratification can be obtained from the water temperature equation (2.33) associated with initial and boundary conditions as described in the following.

For most environmental flow conditions, water velocities are usually in the range of $1 - 10 m/s$. Corresponding with this condition, the characteristic temperature change ΔT_0 is around 2.5×10^{-4} to 2.5×10^{-2} Celsius degree [15]. Thus the radiative heating coefficient is $E_p = \frac{R_{N0}}{\rho_0 c_p U_0 \Delta T_0} = (0.8 - 1)$, corresponding to $U_0 = 1 m/s$ and $R_{N0} = (200 - 250) W/m^2$.

We assume that the water surface temperature is $T_s = 20^0 C$, water depth's temperature $T_b = 10^0 C$, and atmosphere temperature is $T_a = 22^0 C$. Water in the reservoir is initially quiescent and at an initial temperature as given in Figure 3-15.

During the simulation, cold water at $T_{in} = 16^0 C$ flows into the reservoir via the inlet boundary. The outflow temperature satisfies the homogeneous Neu-
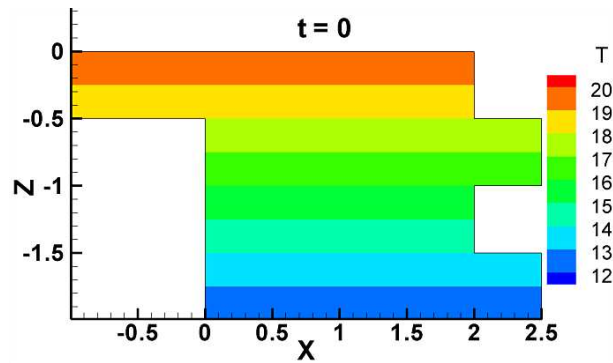
Figure 3-15: The initial temperature field.

mann conditions. The bottom and walls of the reservoir are assumed perfectly insulating. The boundary temperature at the surface is as described in Equation (2.27). The eddy viscosity is calculated from Equation (2.34). Here, depth averaged $H = 2$ and we set $E_t = 1$.

Figure 3-16 shows the process of thermal-stratification in the reservoir from initial stage to final stage. The water in the reservoir is initially quiescent. The inflow with cold water will gradually replace the water inside reservoir. This phenomenon contributes to a decrease in water temperature. The procedure is continued until cold water is completed mixed into the reservoir. However due to the radiation heat exchange, water in the reservoir received energy to maintain an unchanged water temperature. Thus, the surface water maintains at high temperature. The mixing process continues until the amount of cold water is large enough. At this stage, the remaining part of hot water was pushed to the end of reservoir and flowed out. At the steady state, thermal stratification is formed. One thing we can clearly see is that the thermal stratification process is mainly affected by the main streamline. At bottom left corner of reservoir, where the streamline has only a small influence, very little mixing has occurred.
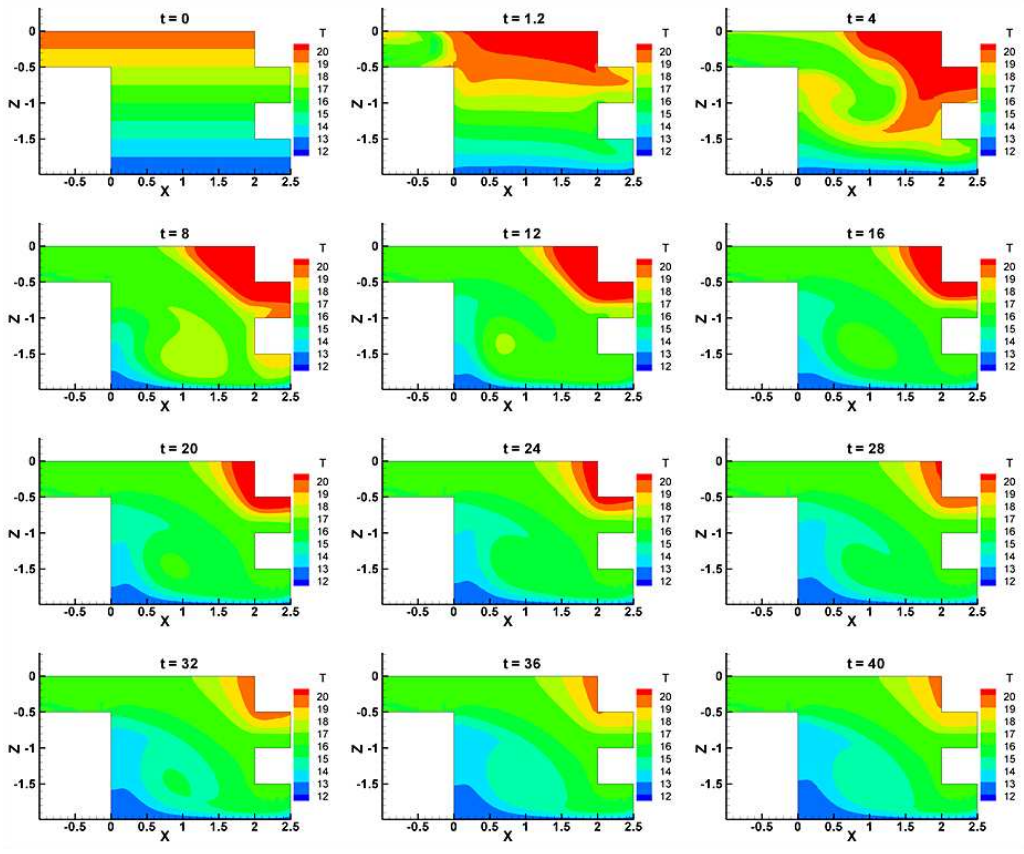
Figure 3-16: The temperature field at different time t.

Figure 3-17 shows the temperature profile at locations $x = 0.5$ and $x = 1.75$. Due to the strong velocity inflow, the temperature profile in the near field changed much more than the temperature profile in the far field.
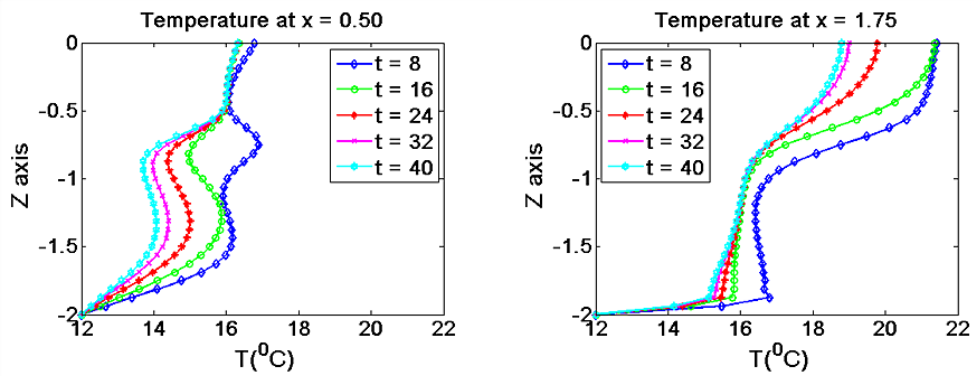
Figure 3-17: The temperature profile at different time t.

3.4.4 Contaminant field

We assume that within the reservoir section, there exists a source of contaminant. In time, the source spreads out and moves around the reservoir. That contaminant field is simulated and obtained by using equation (2.61) associated with initial condition and boundary conditions as described in the following. In this example, we use a source as the superposition of Gaussian sources, each one active on the time interval $t_{0k} \in [t_0, t_{off}]$ and centered at $\phi_k \in \mathcal{D}$, with strength h_k and width σ_{sk}. That is,

$$f_c(\mathbf{x}, t; \boldsymbol{\phi}) = \sum_{k=1}^{n_s} \frac{h_k}{2\pi\sigma_{sk}^2} \exp\left(-\frac{|\boldsymbol{\phi}_k - \mathbf{x}|^2}{2\sigma_{sk}^2}\right) \delta(t - t_{0k}). \qquad (3.10)$$

To consider a simple test case, we choose the number of sources to be $n_s = 1$, located at $\boldsymbol{\phi}_1 = (x_c, z_c)$, with the strength $h_1 = 0.2$ and width $\sigma_{s1} = 0.05$. The active time of the source is $t_{01} \in [0, t_{off}]$ with $t_{off} = 10$.

The inflow boundary and other solid boundaries satisfy a homogeneous Dirichlet condition, Γ_D; the outflow boundaries and free surface boundary satisfy a homogeneous Neumann condition, Γ_N. The diffusivity coefficient is assumed to be constant, $\kappa = 0.005$. Thus the Péclet number $Pe = 200$. The contaminant is assumed to be zero at initial time $t_0 = 0$. Figure 3-18 shows the contaminant solution $c(\mathbf{x}, t)$ of the forward model with $\boldsymbol{\phi}_1 = (0.5, -0.5)$ at specific times. The contaminant field increases while the source is active. After the shutoff time of the source, the contaminant moves away, spreads out and decreases in concentration due to convection and diffusion until it flows out of the domain.
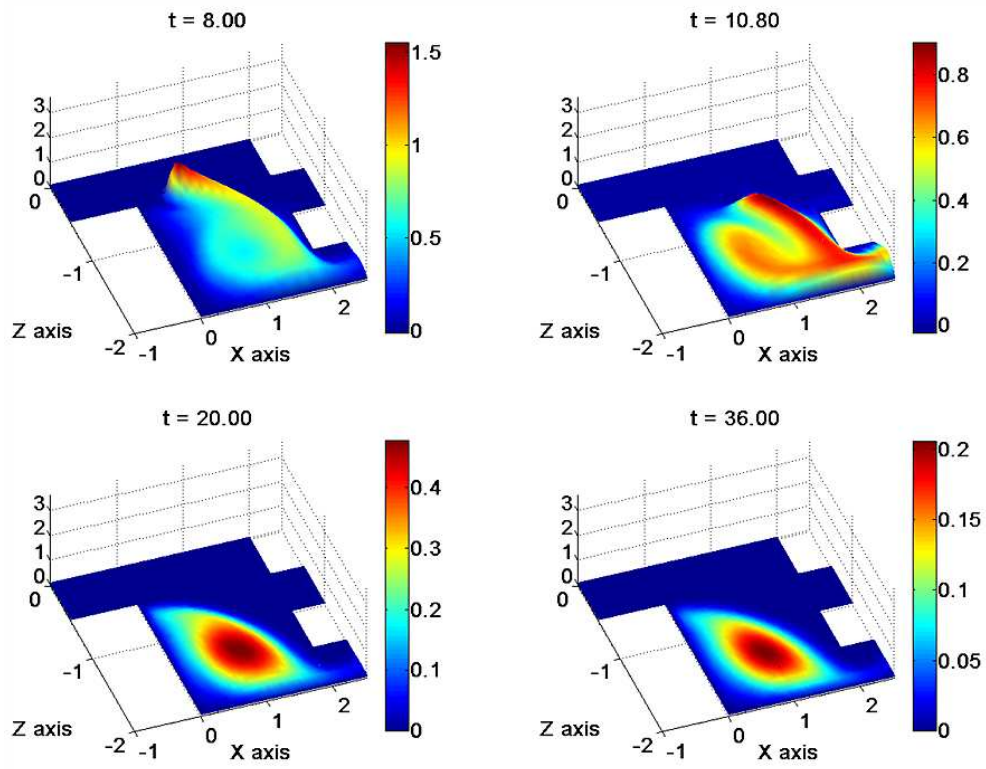
Figure 3-18: Contaminant field of at specific times.

Chapter 4

Reduced-Order Modeling

Reduced-order modeling has been widely used in computational fluid dynamics for the simulation of large-scale systems. In this chapter we present a model order reduction (MOR) technique, based on Galerkin projection and proper orthogonal decomposition (POD) methods. We use these approaches to construct efficient reduced-order models to study properties of dynamical systems in reservoir applications. A general reduction framework for linear systems is presented in Section 4.1. Then we present our Galerkin projection approach for nonlinear systems in Section 4.2.

4.1 General reduction framework for linear system

This section briefly introduces the general reduction framework for linear systems of equations. The reduced-order model is obtained by the combination of the Galerkin projection framework and the proper orthogonal decomposition.

4.1.1 Reduction via Projection

We consider the system of ODEs as they appeared in Eqns. (2.71)–(2.72). For ease of reference, we repeat the equations here:

$$\mathbf{M}\dot{\mathbf{c}} + \Big(\mathbf{C}_c(\mathbf{u}) + \mathbf{K}_c(t; \boldsymbol{\theta}^k)\Big)\mathbf{c} = \mathbf{f}_c(t; \boldsymbol{\phi}), \tag{4.1}$$

$$\mathbf{c}(t_0; \mathbf{Y}) = \mathbf{c}_0(\mathbf{Y}). \tag{4.2}$$

Here, $\mathbf{c}(t; \mathbf{Y}) \in \mathbb{R}^N$ is the discretized approximation of $c(\mathbf{x}, t; \mathbf{Y})$ and contains N state unknowns. $\dot{\mathbf{c}}$ is the derivative of $\mathbf{c}$ with respect to time. $\mathbf{M} \in \mathbb{R}^{N \times N}$ is the mass matrix, $\mathbf{C}_c(\mathbf{u}) \in \mathbb{R}^{N \times N}$ is the convective matrix, $\mathbf{K}_c(t; \boldsymbol{\theta}^k) \in \mathbb{R}^{N \times N}$ is the stiffness matrix, and $\mathbf{f}_c(t; \boldsymbol{\phi}) \in \mathbb{R}^N$ is the external source with $\boldsymbol{\phi} \in \mathbb{R}^2$ are source locations. $\mathbf{u}$ are the velocity field. $\mathbf{Y}(\omega)$ are independent random variables. Here, N is the number of grid points and $\boldsymbol{\theta}^k$ the kth collocation point. We are also interested in the output of contaminant solution at some sensor locations in the domain, which is given by

$$\mathbf{y}_o(t; \mathbf{Y}) = \mathbf{B}\mathbf{c}(t; \mathbf{Y}), \tag{4.3}$$

where matrix $\mathbf{B} \in \mathbb{R}^{N_o \times N}$ and vector $\mathbf{y}_o(t; \mathbf{Y}) \in \mathbb{R}^{N_o}$ contains the N_o outputs of the system. A reduced order model of this system can be derived by approximating the full state vector $\mathbf{c}$ as a linear combination of m basis vectors as follows,

$$\mathbf{c} \approx V \mathbf{c}_r, \tag{4.4}$$

where $\mathbf{c}_r \in \mathbb{R}^m$ is the reduced order state and $V = \begin{bmatrix} v_1 & \cdots & v_m \end{bmatrix} \in \mathbb{R}^{N \times m}$ is an orthonormal basis, i.e., $V^T V = I$. Projecting the system (4.1)–(4.3) onto the reduced space formed by the column span of basis V yields the reduced-order model in (4.5)-(4.7)

$$\mathbf{M}_r \dot{\mathbf{c}}_r + \left(\mathbf{C}_r(\mathbf{u}) + \mathbf{K}_r(t; \boldsymbol{\theta}^k) \right) \mathbf{c}_r = \mathbf{f}_{cr}(t; \boldsymbol{\phi}), \tag{4.5}$$

$$\mathbf{c}_r(t_0; \mathbf{Y}) = \mathbf{c}_{0r}(\mathbf{Y}), \tag{4.6}$$

$$\mathbf{y}_r(t; \mathbf{Y}) = \mathbf{B}_r \mathbf{c}_r(t; \mathbf{Y}). \tag{4.7}$$

Here the reduces matrices are given by

$$\mathbf{M}_r = V^T \mathbf{M} V, \tag{4.8}$$

$$\mathbf{K}_r(t; \boldsymbol{\theta}^k) = V^T \mathbf{K}_c(t; \boldsymbol{\theta}^k) V, \tag{4.9}$$

$$\mathbf{C}_r(\mathbf{u}) = V^T \mathbf{C}_c(\mathbf{u}) V, \tag{4.10}$$

$$\mathbf{f}_{cr}(t; \boldsymbol{\phi}) = V^T \mathbf{f}_c(t; \boldsymbol{\phi}), \tag{4.11}$$

$$\mathbf{B}_r = \mathbf{B} V, \tag{4.12}$$

and the reduction of the given initial condition is

$$\mathbf{c}_{0r}(\mathbf{Y}) = V^T \mathbf{c}_0(\mathbf{Y}). \tag{4.13}$$

The model reduction task is then to find a suitable basis V so that $m \ll N$. In the literature there exist various methods for the computation of proper basis in the case of large-scale system, such as balanced truncation, Krylov-subspace

55

and POD methods. This study will consider POD as the method to compute the basis.

4.1.2 Proper Orthogonal Decomposition

Proper orthogonal decomposition (POD) provides a method to compute the reduced-order basis V and construct the low-order system by projection. Here we briefly describe the general POD method (more details may be found in [52]).

Let $X = [\mathbf{c}^1(t_1)\ \mathbf{c}^1(t_2)\ \cdots \mathbf{c}^1(t_T)\ \mathbf{c}^2(t_1)\ \cdots\ \cdots \mathbf{c}^S(t_T)] \in \mathbb{R}^{N \times Q}$ be a collection of Q snapshot state solutions $\mathbf{c}^s(t_j), j = 1, \cdots, T$, where T is the number of time steps, of the system in (4.1) for $s = 1, \cdots, S$ input parameters. The POD basis is optimal in the sense that vectors V are chosen to maximize the averaged projection of $\mathbf{c}(t)$ onto V, suitably normalized

$$\max_{V} \frac{\langle |\mathbf{c}, V|^2 \rangle}{\|V\|^2}, \tag{4.14}$$

where $|\cdot|$ is the inner product of basis vector V with the field $\mathbf{c}$, $\langle \cdot \rangle$ the time averaged operator and $\|\cdot\|$ the L_2 norm.

The POD basis vectors are the m left singular vectors of X corresponding to the largest singular values $(m \leq Q)$. Let $\sigma_i, i = 1, 2, \cdots, Q$ be the singular values of X in non-increasing order. We determine the number of POD vectors to retain in the reduced-order model by choosing $m \leq Q$ vectors such that

$$\sum_{i=1}^{m} \sigma_i^2 / \sum_{j=1}^{Q} \sigma_j^2 \geq \epsilon_E, \tag{4.15}$$

where $\epsilon_E(\%)$ is the required amount of energy, typically taken to be 99% or higher. After obtaining the POD basis vectors, we can rapidly solve the reduced-order system.

4.1.3 Error quantification

In order to estimate the accuracy of the reduced model relative to the full model, we use the time-dependent relative norm error of solutions $\varepsilon_F(t)$ and relative error of outputs $\varepsilon_s(t)$. These errors are defined as follows

$$\varepsilon_F(t^k) = \frac{\|\mathbf{c}(t^k) - V\mathbf{c}_r(t^k)\|_{L_2(\mathcal{D})}}{\|\mathbf{c}(t^k)\|_{L_2(\mathcal{D})}}, \tag{4.16}$$

$$\varepsilon_y(t^k) = \frac{\|\mathbf{y}(t^k) - \mathbf{y}_r(t^k)\|_{L_2(\mathcal{D})}}{\|\mathbf{y}(t^k)\|_{L_2(\mathcal{D})}}. \tag{4.17}$$

Here, $\mathbf{c}(t^k), \mathbf{c}_r(t^k), 1 \leq k \leq T$ are the full and reduced solutions. $\mathbf{y}(t^k), \mathbf{y}_r(t^k), 1 \leq k \leq T$ are the full and reduced outputs of interest. The space-time norm error ε_F^T is then defined as

$$\varepsilon_F^T = \left(\int_0^{t_f} \varepsilon_F(t) dt \right)^{1/2}. \tag{4.18}$$

4.2 Reduced order model for non-linear systems

In this section, we present an approach to reduce the dimension of the fluid flow equations. The approach uses a combination of Galerkin projection method and proper orthogonal decomposition directly on the Navier-Stokes equations and transport equations to yield a set of ordinary differential equations capturing the essential dynamics of the system. This approach has been widely used in computational fluid mechanics and optimal control applications. For more details,

refer to [59, 61, 63, 90].

4.2.1 Galerkin projection method

The dynamical system for consideration is the two dimensional laterally aver-
aged model as described and simulated in Chapter 2 and Chapter 3. Here, we
re-write the governing equations for ease of discussion:

$$\frac{\partial \mathbf{u}}{\partial t} + (\mathbf{u} \cdot \nabla)\mathbf{u} = -\nabla p + \nu \nabla^2 \mathbf{u} + \mathbf{f} \quad \text{in } \mathcal{D} \times [t_0, t_f], \tag{4.19}$$

$$\nabla \cdot \mathbf{u} = 0 \qquad\qquad \text{in } \mathcal{D} \times [t_0, t_f], \tag{4.20}$$

$$\mathbf{u} = \mathbf{u}_D \qquad\qquad \text{on } \Gamma \times [t_0, t_f], \tag{4.21}$$

$$\mathbf{u}(\mathbf{x}, 0) = \mathbf{u}_0(\mathbf{x}) \qquad\qquad \text{in } \mathcal{D}, \tag{4.22}$$

$$\frac{\partial c}{\partial t} + \mathbf{u} \cdot \nabla c = \nabla \cdot \big(\kappa(\mathbf{x}, t; \omega)\nabla c\big) + f_c(\mathbf{x}, t; \boldsymbol{\phi}) \quad \text{in } \mathcal{D} \times [t_0, t_f], \tag{4.23}$$

$$c = c_D \qquad\qquad \text{on } \Gamma_D \times [t_0, t_f], \tag{4.24}$$

$$\frac{\partial c}{\partial \mathbf{n}} = 0 \qquad\qquad \text{on } \Gamma_N \times [t_0, t_f], \tag{4.25}$$

$$c(\mathbf{x}, t_0; \omega) = c_0(\mathbf{x}; \omega) \qquad\qquad \text{in } \mathcal{D}. \tag{4.26}$$

where $\nu = \frac{1}{Re}$ is the fluid kinematic viscosity. The boundary condition for
the pressure (p) at the water surface is set to zero. The diffusivity $\kappa(\mathbf{x}, t; \omega)$ is
assumed to be a constant.

Let $\big\{\mathbf{u}(\mathbf{x}, t_k)\big\}_{k=1}^{N_{snap}^u}$ be the snapshots of velocity and let $\big\{c(\mathbf{x}, t_k)\big\}_{k=1}^{N_{snap}^c}$ be
the snapshots of contaminant field, where N_{snap}^u and N_{snap}^c are the number of
velocity and contaminant snapshots, respectively. The velocity field is decom-
posed as follows

$$\mathbf{u}(\mathbf{x}, t) = \mathbf{u}_m(\mathbf{x}) + \mathbf{u}'(\mathbf{x}, t), \tag{4.27}$$

where $\mathbf{u}_m = \frac{1}{n^u_{snap}} \sum_{k=1}^{N^u_{snap}} \mathbf{u}(\mathbf{x}, t^k)$ is the mean flow, and $\mathbf{u}'(\mathbf{x}, t)$ the fluctuating velocity field. The fluctuating velocity field is represented by the proper orthogonal decomposition

$$\mathbf{u}'(\mathbf{x}, t) = \sum_{k=1}^{N^u_{snap}} \alpha_k(t) \mathbf{\Phi}_k(\mathbf{x}), \tag{4.28}$$

where $\mathbf{\Phi}_k(\mathbf{x})$ is the kth POD basis for the velocity and $\alpha_k(t)$ is the corresponding time dependent amplitude. We now consider the expansion of the velocity field as follows

$$\mathbf{u}(\mathbf{x}, t) = \mathbf{u}_m(\mathbf{x}) + \sum_{k=1}^{M_u} \alpha_k(t) \mathbf{\Phi}_k(\mathbf{x}). \tag{4.29}$$

where $M_u \ll N^u_{snap}$ is the number of POD velocity basis vectors used in the approximation. A similar formulation can be obtained for the contaminant field

$$c(\mathbf{x}, t) = c_m(\mathbf{x}) + \sum_{k=1}^{M_c} \gamma_k(t) \mathbf{\Psi}_k(\mathbf{x}), \tag{4.30}$$

where $\mathbf{\Psi}_k(\mathbf{x})$ is the kth POD basis for the contaminant and $\gamma_k(t)$ is the corresponding time dependent amplitude, $M_c \ll N^c_{snap}$ is the number of POD contaminant basis vectors used in the approximation.

4.2.2 Galerkin system

The Galerkin approximation to equations (4.19) and (4.23) is then

$$\left(\mathbf{\Phi}_i, \frac{\partial \mathbf{u}}{\partial t} + (\mathbf{u} \cdot \nabla)\mathbf{u}\right) + (\mathbf{\Phi}_i, \nabla p) = -\nu(\nabla \mathbf{\Phi}_i, \nabla \mathbf{u}) + (\mathbf{\Phi}_i, \mathbf{f}), \quad (4.31)$$

$$(\mathbf{\Phi}_i, \nabla \cdot \mathbf{u}) = 0, \quad (4.32)$$

$$\left(\mathbf{\Psi}_i, \frac{\partial c}{\partial t}\right) + \left(\mathbf{u} \cdot \nabla c, \mathbf{\Psi}_i\right) = -\kappa(\nabla \mathbf{\Psi}_i, \nabla c) + (\mathbf{\Psi}_i, f_c). \quad (4.33)$$

The Galerkin projection of the first term in (4.31) give us the local acceleration term

$$\left(\mathbf{\Phi}_i(\mathbf{x}), \frac{\partial}{\partial t}\left[\mathbf{u}_m(\mathbf{x}) + \sum_{j=1}^{M_u} \alpha_j(t)\mathbf{\Phi}_j(\mathbf{x})\right]\right)_{\mathcal{D}} = \sum_{j=1}^{M_u} \dot{\alpha}_j(\mathbf{\Phi}_i, \mathbf{\Phi}_j)_{\mathcal{D}} = \dot{\alpha}_i. \quad (4.34)$$

The convective term in (4.31) has the form as

$$-\left(\mathbf{\Phi}_i, (\mathbf{u} \cdot \nabla)\mathbf{u}\right) = -\left(\mathbf{\Phi}_i, \left(\left[\mathbf{u}_m + \sum_{j=1}^{M_u} \alpha_j(t)\mathbf{\Phi}_j\right] \cdot \nabla\right)\left[\mathbf{u}_m + \sum_{j=1}^{M_u} \alpha_j(t)\mathbf{\Phi}_j\right]\right)$$

$$= -\sum_{j=1}^{M_u} \left[\left(\mathbf{\Phi}_i, (\mathbf{\Phi}_j \cdot \nabla)\mathbf{u}_m\right) + \left(\mathbf{\Phi}_i, (\mathbf{u}_m \cdot \nabla)\mathbf{\Phi}_j\right)\right]\alpha_j$$

$$-\left(\mathbf{\Phi}_i, (\mathbf{u}_m \cdot \nabla)\mathbf{u}_m\right)$$

$$-\sum_{j=1}^{M_u}\sum_{k=1}^{M_u} \left(\mathbf{\Phi}_i, (\mathbf{\Phi}_j \cdot \nabla)\mathbf{\Phi}_k\right)\alpha_j\alpha_k. \quad (4.35)$$

To derive the Galerkin projection for the pressure term we first construct a solution of the pressure-Poisson equation with respect to p then project its solution of basis space [63]. Neglecting the residual of the Galerkin expansion, the

Galerkin projection of the pressure term becomes

$$(\mathbf{\Phi}_i, \nabla p) = [p\mathbf{\Phi}_i]. \tag{4.36}$$

This surface integral vanishes for Dirichlet boundary conditions. In this case, the pressure-term has no role in the Galerkin projection. The time-dependent velocity term in (4.33) has the form as

$$
\begin{aligned}
-\Big(\mathbf{u}\cdot\nabla c, \mathbf{\Psi}_i\Big) &= -\Big([\mathbf{u}_m + \sum_{k=1}^{M_u}\alpha_k(t)\mathbf{\Phi}_k]\cdot\nabla[c_m + \sum_{j=1}^{M_c}\gamma_j(t)\mathbf{\Psi}_j], \mathbf{\Psi}_i\Big) \\
&= -\sum_{j=1}^{M_c}\Big(([\mathbf{u}_m\cdot\nabla\mathbf{\Psi}_j], \mathbf{\Psi}_i) + \big(\sum_{k=1}^{M_u}[\alpha_k\mathbf{\Phi}_k\cdot\nabla\mathbf{\Psi}_j], \mathbf{\Psi}_i\big)\Big)\gamma_j \\
&\quad -\big([\mathbf{u}_m\cdot\nabla c_m], \mathbf{\Psi}_i\big) - \Big(\sum_{k=1}^{M_u}[\alpha_k\mathbf{\Phi}_k\cdot\nabla c_m], \mathbf{\Psi}_i\Big). \tag{4.37}
\end{aligned}
$$

Apply the Galerkin projection for the remaining terms, then re-arrange the co-efficients, we have

$$\frac{d\alpha_i}{dt} = \Big[a_i + \sum_{j=1}^{M_u}b_{ij}\alpha_j + \sum_{j=1}^{M_u}\sum_{k=1}^{M_u}c_{ijk}\alpha_j\alpha_k\Big], \tag{4.38}$$

$$\alpha_i(0) = \alpha_{i0}, \tag{4.39}$$

$$\frac{d\gamma_i}{dt} = \Big[\bar{a}_{mi} + \sum_{k=1}^{M_u}\alpha_k\bar{a}_{uik}\Big] + \sum_{j=1}^{M_c}\Big[\bar{b}_{mij} + \sum_{k=1}^{M_u}\alpha_k\bar{b}_{uijk}\Big]\gamma_j, \tag{4.40}$$

$$\gamma_i(0) = \gamma_{i0}. \tag{4.41}$$

Here the coefficients are computed as

$$a_i = -\big(\boldsymbol{\Phi}_i, (\mathbf{u}_m \cdot \nabla)\mathbf{u}_m\big) - \nu\big(\nabla\boldsymbol{\Phi}_i, \nabla\mathbf{u}_m\big) + \big(\boldsymbol{\Phi}_i, \mathbf{f}\big),$$

$$b_{ij} = -\big(\boldsymbol{\Phi}_i, (\boldsymbol{\Phi}_j \cdot \nabla)\mathbf{u}_m\big) - \big(\boldsymbol{\Phi}_i, (\mathbf{u}_m \cdot \nabla)\boldsymbol{\Phi}_j\big) - \nu\big(\nabla\boldsymbol{\Phi}_i, \nabla\boldsymbol{\Phi}_j\big),$$

$$c_{ijk} = -\big(\boldsymbol{\Phi}_i, (\boldsymbol{\Phi}_j \cdot \nabla)\boldsymbol{\Phi}_k\big), \tag{4.42}$$

$$\bar{a}_{mi} = -\big(\boldsymbol{\Psi}_i, \mathbf{u}_m \cdot \nabla c_m\big) - \kappa\big(\nabla\boldsymbol{\Psi}_i, \nabla c_m\big) + \big(\boldsymbol{\Psi}_i, f_c\big),$$

$$\bar{a}_{uik} = -\big(\boldsymbol{\Psi}_i, \Phi_k \cdot \nabla c_m\big),$$

$$\bar{b}_{mij} = -\big(\boldsymbol{\Psi}_i, \mathbf{u}_m \cdot \nabla\boldsymbol{\Psi}_j\big) - \kappa\big(\nabla\boldsymbol{\Psi}_i, \nabla\boldsymbol{\Psi}_j\big), \tag{4.43}$$

$$\bar{b}_{uijk} = -\big(\boldsymbol{\Psi}_i, \Phi_k \cdot \nabla\boldsymbol{\Psi}_j\big).$$

The initial values are computed as

$$\alpha_{i0} = \big(\boldsymbol{\Phi}_i, \mathbf{u}_0\big),$$

$$\gamma_{i0} = \big(\boldsymbol{\Psi}_i, c_0\big). \tag{4.44}$$

Solving the above initial value problem (4.38)–(4.41) we can obtain a set of predicted time histories for the mode amplitude of the POD approximation. Next, we shall consider a numerical example for the non-linear system.

4.2.3 Numerical example for ROM of non-linear system

We consider the solution of 2D laterally averaged system as described in Section 3.4. The snapshot is obtained at every $10\Delta t$ with time-step size $\Delta t = 0.08$. The POD method of snapshots as defined above resulted in M_u modes on POD velocity basis vectors and M_c modes on POD contaminant basis vectors. The

nonlinear Galerkin system (4.38)–(4.41) is then solved by a fourth order Runge-Kutta scheme. We note that solution $\gamma(t)$ in equation (4.40) depends on solution $\alpha(t)$ in equation (4.38) and the number of POD velocity basis vectors M_u. So we can solve two equations separately to determine which numbers of POD basis vectors are suitable for our ROMs and to evaluate the online computational time to solve ODEs of each Galerkin system.

Time-dependent relative norm errors between the full finite element and POD-based ROM solutions with $M_u = 3, 6, 9, 12, 15$ and 18 basis functions are given in Figure 4-1 and Table 4.1. Here the time-space norm error is defined as in Eqn. (4.18). With $M_u = 18$ POD velocity basis vectors, the energy cap-
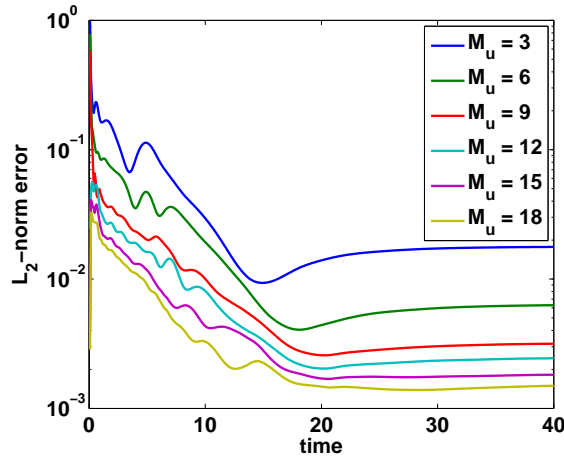
Figure 4-1: The time-dependent relative norm error $\varepsilon_u(t)$ between full FEM and POD-based ROM solutions with different number of POD velocity basis vectors.

ture is almost 100% and the relative error is around 10^{-3}. From Figure 4-1 we observe that there is little improvement in the accuracy when we use more than 12 POD velocity basis functions. However, the computational time for solving the online stage[1] increases from 6.5 second for $M_u = 12$ POD to 21.4 seconds

---

[1]The simulations were performed on a personal computer (PC) with processor Intel(R) Core(TM)2 Duo CPU E8200 @2.66GHz 2.66GHz, RAM 3.25GB, 32-bit Operating System.

Table 4.1: Time-space norm error between full FEM and POD-based ROM solutions corresponding the snapshot energy and the POD velocity basis; and the online computational time of the Galerkin system.

M_u	3	6	9	12	15	18
$\epsilon_E(\%)$	96.1447	98.8184	99.1643	99.911	99.993	99.999
ε_u^T	0.457	0.291	0.195	0.072	0.051	0.011
$t_{onlineNS}(s)$	0.4	0.5	1.2	6.5	12.6	21.4

for $M_u = 18$ POD as in Table 4.1. In this study, we choose $M_u = 12$ POD velocity basis vectors.

Figure 4-2 shows the comparison between the predicted (integrated the Galerkin system) and projected (from snapshots) temporal amplitudes with the first 6 POD velocity basis vectors. Predicted solutions match very well the behavior of projected solutions. The velocity then can be reconstructed using equation
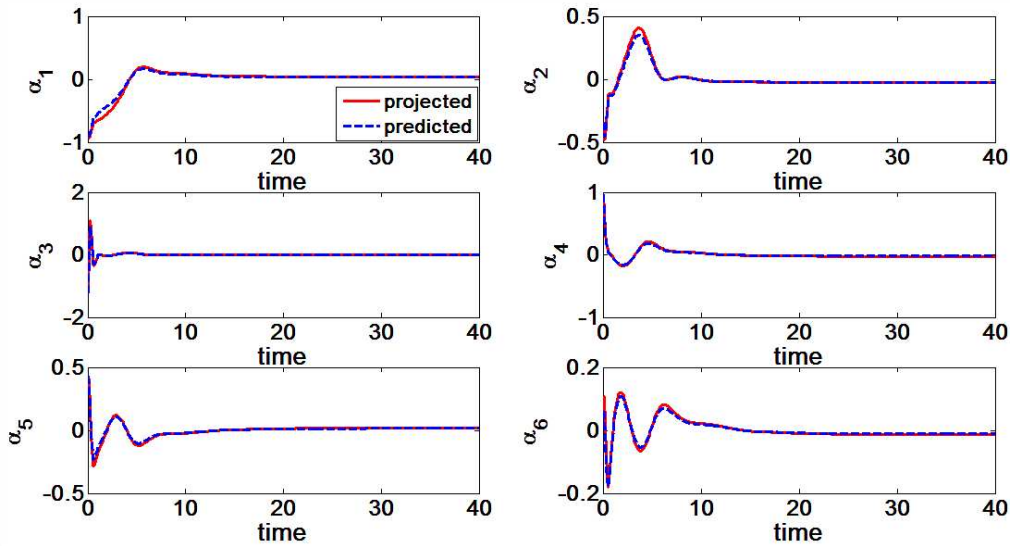
Figure 4-2: Comparison between the predicted and projected mode amplitudes.

(4.29) with $\alpha(t)$ are obtained in (4.38). Figure 4-3 shows the comparison of velocity profile at specific location between the FEM and ROMs solutions with $M_u = 12$ POD velocity basis vectors. We observe that ROMs are able to repre-

sent the most characteristics of the full velocity profiles.
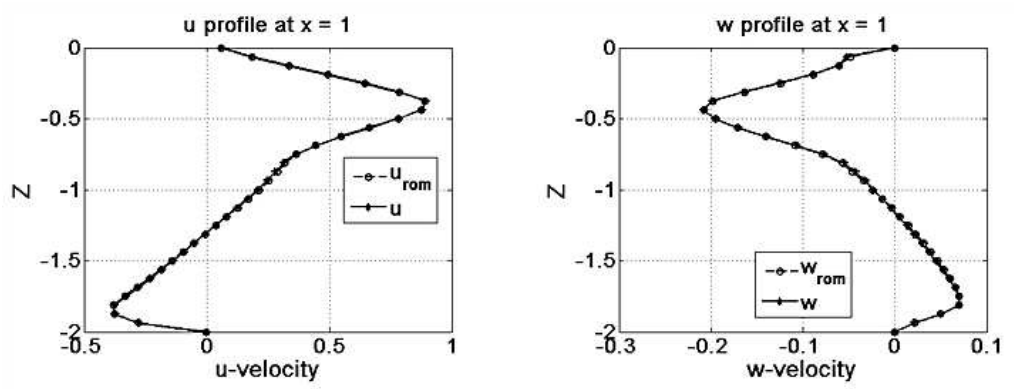
Figure 4-3: Velocity profile at $x = 1$. u and w are the FEM solutions while u_{rom} and w_{rom} are the ROM solutions.

The relative norm errors between the full FEM and POD-based ROM solutions of the transport problems with $M_c = 8, 12, 16, 20, 24$ and 30 basis functions corresponding with $M_u = 12$ basis functions are given in Table 4.2. When

Table 4.2: Time-space norm error between full FEM and POD-based ROM solutions corresponding the snapshot energy and the POD basis; and the online computational time of the Galerkin system.

M_c	8	12	16	20	24	30
$\epsilon_E(\%)$	99.8705	99.9781	99.9975	99.9992	99.9998	99.9999
ε_c^T	0.257	0.162	0.106	0.074	0.052	0.034
$t_{onlineCD}(s)$	2.4	3.5	4.8	7.8	12.1	19.6

the number of POD basis vectors $M_c \geq 20$, there is little improvement in the accuracy in the reduced model, but the online computational time has a big increase. As such $M_c = 20$ POD contaminant basis vectors is suitable for our ROMs. The computational time of the full FEM solutions is approximately $t_{fullCD} \approx 700$ seconds while the computational time of the Galerkin solutions with $M_c = 20$ POD contaminant basis is $t_{onlineCD} \approx 7.8$ seconds. The speed-up factor is around $r_t = \frac{t_{fullCD}}{t_{onlineCD}} \approx 90$ times.

65

Chapter 5

Optimal control for contaminant transport

This chapter presents a strategy to manage water quality for reservoir applications. The strategy is a combination of estimating the contaminant locations within a reservoir and then applying the optimal control on the velocity field to flush the contaminant out of the water body. This strategy also takes into account the uncertainty information such as wind velocity, measurement noise, etc., to make the problem more realistic. A Bayesian inference approach is applied for estimating contaminant source locations. Then the one shot or adjoint method is employed to determine an optimal control velocity. For large-scale models such as reservoir applications, the computational effort is too expensive and time-consuming. Model-order reduction techniques (as described in Chapter 4) are applied to reduce the cost and storage requirement.

We organize this chapter into two parts. Part I: we set up a simple model for contaminant transport with constant velocity fields. Section 5.1 presents a deter-

ministic control, in which we assume that contaminant source is a point source. Section 5.2 presents a stochastic optimal control problem, in which we assume that the uncertain parameter is presented in the diffusivity coefficients. We move on to the real applications in Part II: contaminant sources are uncertain. We first estimate the probable source locations and then apply the stochastic control to determine an optimal control strategy as described in Section 5.3.

5.1   Deterministic control for contaminant transport

This section presents a deterministic optimal control problem for a simple contaminant transport model with constant velocity fields. The optimal control formulation is based on the adjoint method. Numerical simulations present the results for a simple problem.

5.1.1   Formulation

Problem Description

Consider the fluid flows through a physical domain $\mathcal{D} \in \mathbb{R}^2$ as described in Subsection 2.4.3. The contaminant transport with boundary condition and initial conditions are given in (2.61)–(2.64). This is the general case for stochastic contaminant transport problems. In this study, however, we want to explore a deterministic control problem first. We assume that the diffusivity coefficient $\kappa(\mathbf{x}, t; \omega)$ is a constant. Hence we can ignore all the stochastic variables in the system of equations.

Suppose that we have determined a location of contaminant source in the

67

domain. Our objective is to flush the contaminants out of the domain by controlling the velocity of the fluid pump. This velocity $\mathbf{u} = [u \; v]^T$ is the convective velocity in the transport equations (2.61). The objective functional is given by

$$\mathcal{J}(c, \mathbf{u}) = \frac{1}{2} \int_{t_0}^{t_f} \int_{\mathcal{D}} c^2 d\mathcal{D} \; dt + \frac{\eta_w}{2} \int_{t_0}^{t_f} \|\mathbf{u}\|^2 \; dt, \qquad (5.1)$$

where η_w is a constant controlling the relative weighting of the components of the objective function. The optimal control problem is stated as: find $c, \mathbf{u}$ such that the functional $\mathcal{J}$ defined in (5.1) is minimized subject to the requirements that $c, \mathbf{u}$ satisfy the model constraints (2.61)–(2.64).

Semi-Discretization

Discretizing the PDEs (2.61)–(2.64) using the finite element method [77], we obtain an ODE system in the form of (2.71)–(2.72). Here we note that the stiffness matrix $\mathbf{K}_c(t; \boldsymbol{\theta}^k)$ is an invariant matrix, and the contaminant concentration is function of time $\mathbf{c}(t)$. The optimal control problem can now be stated as: minimize the amount of contaminant $\mathbf{c}$ and the cost of the control $\mathbf{u}$, given by

$$\mathcal{J}(\mathbf{c}, \mathbf{u}) = \frac{1}{2} \int_{t_0}^{t_f} \mathbf{c}^T \mathbf{M} \mathbf{c} \; dt + \frac{\eta_w}{2} \int_{t_0}^{t_f} \mathbf{u}^T \mathbf{u} \; dt. \qquad (5.2)$$

The optimality system

We introduce the Lagrangian functional with the adjoint state $\mathbf{p}(t)$ and adjoint initial condition $\chi \in \mathbb{R}^N$ as follows

$$
\mathcal{L}(\mathbf{c}, \mathbf{u}, \mathbf{p}, \chi) = \mathcal{J}(\mathbf{c}, \mathbf{u}) - \chi^T(\mathbf{c}|_{t=0} - \mathbf{c}_0)
$$
$$
- \int_{t_0}^{t_f} \mathbf{p}^T \Big(\mathbf{M}\dot{\mathbf{c}} + \big(\mathbf{C}_c(\mathbf{u}) + \mathbf{K}_c(t; \boldsymbol{\theta}^k) \big)\mathbf{c} - \mathbf{f}_c(t; \boldsymbol{\phi}) \Big). \quad (5.3)
$$

The first-order necessary conditions, also known as the Karush-Kuhn-Tucker (KKT) optimality conditions [37, 91] yield an optimality system from which optimal states and control parameters can be determined by taking variations with respect to $\mathbf{c}, \mathbf{p}$ and $\mathbf{u}$. That is:

1. State equation

   Setting the first variation of $\mathcal{L}$ with respect to the Lagrange multiplier $\mathbf{p}$ to zero, we obtain

$$
\frac{\delta \mathcal{L}}{\delta \mathbf{p}} = \lim_{\epsilon \to 0} \left(\frac{\mathcal{L}(\mathbf{c}, \mathbf{u}, \mathbf{p} + \epsilon \tilde{p}, \chi) - \mathcal{L}(\mathbf{c}, \mathbf{u}, \mathbf{p}, \chi)}{\epsilon} \right) = 0,
$$
$$
\Longleftrightarrow \tilde{p} \Big(\mathbf{M}\dot{\mathbf{c}} + \big(\mathbf{C}_c(\mathbf{u}) + \mathbf{K}_c(t; \boldsymbol{\theta}^k) \big)\mathbf{c} - \mathbf{f}_c(t; \boldsymbol{\phi}) \Big)
$$
$$
- \chi^T(\mathbf{c}|_{t=0} - \mathbf{c}_0) = 0, \quad (5.4)
$$

   where $\tilde{p}$ is an arbitrary variation.

   Since the variation $\tilde{p}$ in the Lagrange multiplier is arbitrary, we recover the ODEs (2.71)–(2.72).

2. Adjoint equation

Setting the first variation of $\mathcal{L}$ with respect to the state $\mathbf{c}$ to zero, we obtain

$$\frac{\delta\mathcal{L}}{\delta\mathbf{c}} = \lim_{\epsilon\to 0} \left(\frac{\mathcal{L}(\mathbf{c}+\tilde{c}, \mathbf{p}, \mathbf{u}, \chi) - \mathcal{L}(\mathbf{c}, \mathbf{u}, \mathbf{p}, \chi)}{\epsilon} \right)$$
$$= \int_{t_0}^{t_f} \left[-\mathbf{p}^T\mathbf{M}\dot{\tilde{c}} - \mathbf{p}^T\left(\mathbf{C}_c(\mathbf{u}) + \mathbf{K}(t; \boldsymbol{\theta}^k)\right)\tilde{c} + \tilde{c}\mathbf{M}\mathbf{c} \right] dt = 0, (5.5)$$

where the variation $\tilde{c}$ in the state $\mathbf{c}$ is arbitrary.

Integrating equation (5.5) by parts with respect to time for term $\dot{\tilde{c}}$ and since the variation $\tilde{c}$ is arbitrary, we obtain the adjoint equations as

$$-\mathbf{M}^T\dot{\mathbf{p}} + \left(\mathbf{C}_c(\mathbf{u}) + \mathbf{K}(t; \boldsymbol{\theta}^k)\right)^T\mathbf{p} = \mathbf{M}\mathbf{c}, \quad \text{in } \mathcal{D} \times [t_0 \times t_f] \quad (5.6)$$

$$\mathbf{p}(t_f) = 0. \quad (5.7)$$

3. Optimality condition

The first variation of $\mathcal{L}$ with respect to the control $\mathbf{u}$ is given by

$$\frac{\delta\mathcal{L}}{\delta\mathbf{u}} = \lim_{\epsilon\to 0} \left(\frac{\mathcal{L}(\mathbf{c}(\mathbf{u}+\epsilon h), \mathbf{u}+\epsilon h, \mathbf{p}, \chi) - \mathcal{L}(\mathbf{c}, \mathbf{u}, \mathbf{p}, \chi)}{\epsilon} \right). \quad (5.8)$$

where h is an variation in the control $\mathbf{u}$.

Setting equation (5.8) to zero and manipulating the formulation we can obtain the optimal control equation given below as

$$\mathcal{L}_{,\mathbf{u}} := \frac{\delta\mathcal{L}}{\delta\mathbf{u}} = \eta_w \int_{t_0}^{t_f} \mathbf{u}\, dt - \int_{t_0}^{t_f} \mathbf{c}^T\mathbf{C}(\mathbf{u})\, \mathbf{p}\, dt. \quad (5.9)$$

Summarizing, the state equation, adjoint equation, and optimality condition form the optimality system, solutions of which provide the optimal state $\mathbf{c}$, ad-

joint state **p**, and control function **u**. To solve the KKT system for deterministic control, we use Algorithm 1 in Appendix **B**.

5.1.2   Results

We present the 2D mathematical model to which we apply the deterministic optimal control with the full model using Algorithm 1. A finite difference test is first used to validate the numerical algorithm. We compare the contaminant field with optimal control actions and without control action.

Model setup

In order to implement the contaminant transport problem, we consider the computational domain as in Figure 5-1. The domain is rectangular with $\mathcal{D} = [0,1] \times [0,0.5]$. The inflow boundary, which is defined on $x = 0, 0 \leq y \leq 0.5$, satisfies a homogeneous Dirichlet condition, Γ_D; the remaining boundaries satisfy homogeneous Neumann conditions, Γ_N. The velocity vector with x and y-component is chosen as uniform and constant in time, given by $\mathbf{u} = [u \ v]^T$. A velocity of $\mathbf{u} = [1 \ 0]^T$ is used as an initial guess for finding an optimal velocity. The diffusivity coefficient is assumed to be constant and is given as $\kappa = 0.005$ corresponding to a Péclet number of $Pe = 200$.

In this example, we discretize the KKT system on a $n_x \times n_y = 61 \times 31$ grid, where n_x and n_y are the number of grid points in x and y-direction, respectively. This results in $N = 1891$ spatially discrete unknowns using the standard finite element method. The Crank-Nicolson method is employed to discretize the system in time, where $t \in [t_0, t_f]$ with $t_0 = 0, t_f = 1.4$ and the time-step size
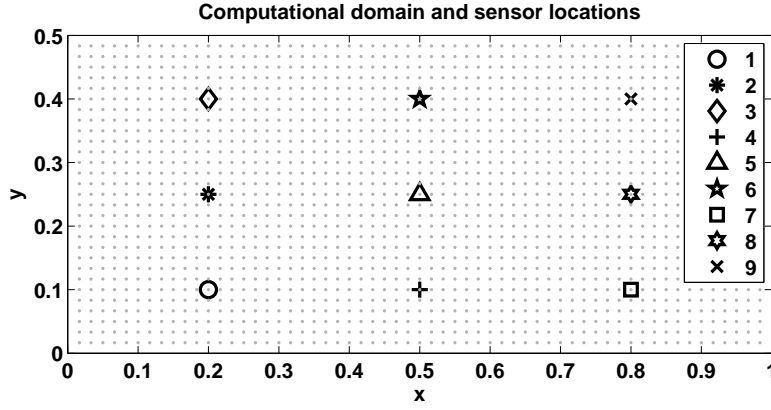
Figure 5-1: The computational domain with $N_o = 9$ sensors.

$\Delta t = 0.02$ or $T = 70$ time steps.

The source function $f_c(\mathbf{x}, t; \boldsymbol{\phi})$ is described as a Gaussian shape as follows,

$$f_c(\mathbf{x}, t; \boldsymbol{\phi}) = \sum_{k=1}^{n_s} \frac{h_k}{2\pi\sigma_{sk}^2} \exp\left(-\frac{|\boldsymbol{\phi}_k - \mathbf{x}|^2}{2\sigma_{sk}^2}\right)\delta(t - t_{0k}). \qquad (5.10)$$

Here, we choose the number of sources to be $n_s = 1$, located at $\boldsymbol{\phi}_1 = (x_c, y_c) = (0.3, 0.25)$, with the strength $h_1 = 1$ and width $\sigma_{s1} = 0.05$. The active time of the source is $t_{01} \in [t_0, t_{off}]$ with $t_{off} = 0.4$.

Figure 5-2 shows the contaminant solution $c(\mathbf{x}, t; \kappa_0)$ of the full model at specific time. The contaminant field increases in magnitude while the source is active. After the shutoff time of the source, the contaminant moves away and spreads out due to convection and diffusion until it flows out of the domain.

Finite Difference test

The finite difference method is used here to check the sensitivity of the gradient-based optimization algorithms. The objective functional $\mathcal{J}$ can be written using
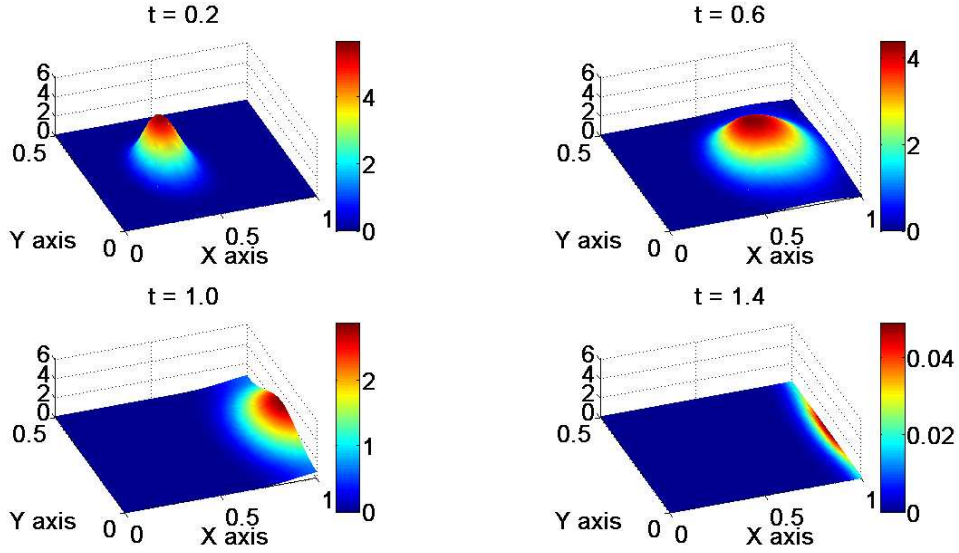
Figure 5-2: Contaminant field of full model at times $t = 0.2, t = 0.6, t = 1.0$ and $t = 1.4$.

a Taylor Series expansion:

$$\mathcal{J}(\mathbf{c}, \mathbf{u}_0 + \epsilon) = \mathcal{J}(\mathbf{c}, \mathbf{u}_0) + \epsilon \mathcal{J}'(\mathbf{c}, \mathbf{u}_0) + \frac{\epsilon^2}{2} \mathcal{J}''(\mathbf{c}, \mathbf{u}_0) + \mathcal{O}\epsilon^3. \qquad (5.11)$$

Neglecting the second order and higher order terms, we obtain the approximation of the gradient vector

$$\mathcal{J}_{,\mathbf{u}} :\equiv \mathcal{J}'(\mathbf{c}, \mathbf{u}_0) \approx \frac{\mathcal{J}(\mathbf{c}, \mathbf{u}_0 + \epsilon) - \mathcal{J}(\mathbf{c}, \mathbf{u}_0)}{\epsilon}. \qquad (5.12)$$

Equation (5.12) is called the forward difference scheme. We shall use this to compare with the gradient formulations (5.9) above. The relative error is given by

$$\text{error} = \frac{\mathcal{L}_{,\mathbf{u}} - \mathcal{J}_{,\mathbf{u}}}{\mathcal{L}_{,\mathbf{u}}}. \qquad (5.13)$$

Figure 5-3 shows the relative error of the gradient test. Figures 5-3(a) and 5-3(b) show the test case with initial velocity fields $\mathbf{u} = [1; 0]$, while the Figures

73

5-3(c) and 5-3(d) are results with initial velocity fields $\mathbf{u} = [0; 1]$. These figures validate that the adjoint-based gradient calculation is implemented correctly.

(a) gradient of $\mathcal{J}$ with respect to u

(b) gradient of $\mathcal{J}$ with respect to v

(c) gradient of $\mathcal{J}$ with respect to u

(d) gradient of $\mathcal{J}$ with respect to v
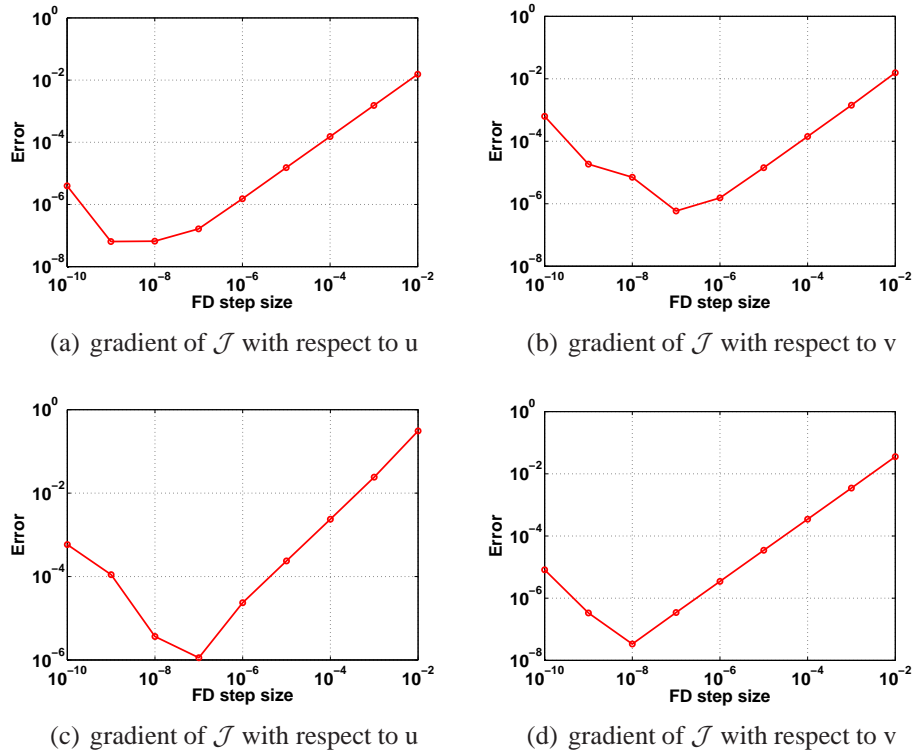
Figure 5-3: Finite Difference test of the cost function with the respect to the control $\mathbf{u}$.

Optimal velocity control

Once the source location is determined, we want to flush the contaminants out of the domain rapidly by applying the optimal control algorithm 1. Figure 5-4 shows the contaminant field c of the forward model at time $t = 1.2$, for the example case where the source is positioned at $x_c = 0.3, y_c = 0.25$. We can see the effectiveness of the optimal velocity control to flush the contaminant c out of the domain. When applying control the contaminant is removed from the domain faster in comparison with the case without applying the control.

(a) Applying control   (b) Without applying control
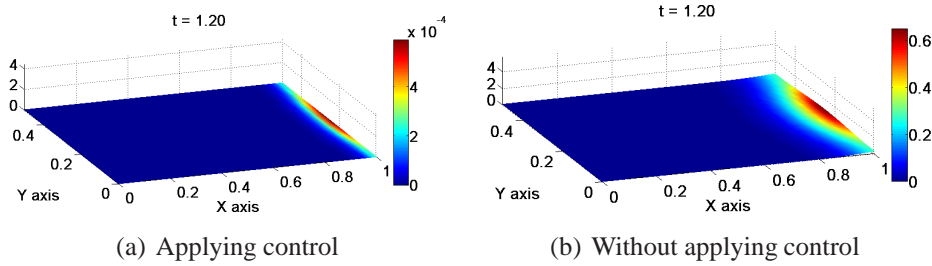
Figure 5-4: Contaminant field c of the forward model at $t = 1.2$. Note the difference in contaminant concentration scale between the two plots.

5.1.3 Remarks

In this section, we have explored the deterministic optimal control problem for the transport equations. A gradient-based optimization approach is used to determine the optimal control solution. Applying optimal control gives us an efficient way to achieve water quality management. However, it is just an ideal case where there is no influence from external uncertain factors. In real applications, there are factors that impact the system and hence affect the solution. In the next section, we shall consider the optimal control problem with uncertain input parameters.

5.2 Stochastic control for contaminant transport

This section presents a stochastic optimal control problem for a contaminant transport model with a constant velocity field. The stochastic optimal control formulation is based on a combination of model reduction, an adjoint approach and a collocation method. Numerical simulation presents the result of this type of control, and compare the effectiveness of the control based on the full model with that based on reduced-order model.

5.2.1 Formulation

Problem Description

Consider the fluid flows through a physical domain $\mathcal{D} \in \mathbb{R}^2$ as described in Subsection 2.4.3. The stochastic contaminant transport with boundary condition and initial conditions are given in (2.61)–(2.64). The stochastic collocation method with the finite element method approximates this a SPDE problem. Suppose that we have already determined a location of contaminant source in the domain. The goal of our control problem is to flush the contaminant out of the domain by controlling the velocity of the fluid pump. The objective functional is to seek a velocity over an admissible control set $\mathbf{u} \in U_{ad}$ that minimizes a weighted combination of the L_2-norm of the expected contaminant field and the velocity field:

$$\min_{\mathbf{u} \in U_{ad}} \hat{\mathcal{J}} = \frac{1}{2} \int_{t_0}^{t_f} \mathbb{E}\left[\|c(\mathbf{x},t;\omega)\|_{L_2}^2\right] dt + \frac{\eta_w}{2} \int_{t_0}^{t_f} \|\mathbf{u}\|_{L_2}^2 dt, \qquad (5.14)$$

subject to the constraints Eqns. (2.61)–(2.64). Here, η_w is a constant controlling the relative weighting of the components of the objective function and $\mathbb{E}[\cdot]$ denotes the expectation operator.

Semi-Discretization

The finite element method (FEM) [77] together with collocation method is employed to obtain a semi-discrete set of equations as given in (2.71)–(2.72).

We now consider optimal control with the cost functional as given in Equation (5.14). In the collocation framework, the expected value is approximated

via a quadrature rule (such as Clenshaw–Curtis quadrature [92]) built on the collocation points. Define $\{w^k\}_{k=1}^P$ to be the quadrature weights associated with the collocation points,

$$w^k = \int_\Theta \rho(\mathbf{Y})L_k^2(\boldsymbol{\theta})d\boldsymbol{\theta}, \quad \text{for } k = 1, \cdots, P, \tag{5.15}$$

where $\rho(\mathbf{Y})$ is the probability density of the random vector $\mathbf{Y}$. The cost functional is replaced by the discretized problem as follows

$$\min_{\mathbf{u}\in U_{ad}} \hat{\mathcal{J}}(\mathbf{u}) = \frac{1}{2}\int_{t_0}^{t_f} \sum_{k=1}^P w^k \mathbf{c}^T(t; \mathbf{Y})\, \mathbf{M}\, \mathbf{c}(t; \mathbf{Y})\, dt$$
$$+ \frac{\eta_w}{2}\int_{t_0}^{t_f} \|\mathbf{u}\|_{L_2}^2\, dt. \tag{5.16}$$

Here, the solution $\mathbf{c}(t; \mathbf{Y}), k = 1, \cdots, P$, solves the ordinary differential equations (ODEs) (2.71)–(2.72).

The Optimality System

We introduce the Lagrangian functional with the adjoint state $\mathbf{p}(t; \mathbf{Y})$ and adjoint initial condition $\chi \in \mathbb{R}^N$ as follows

$$\mathcal{L}(\mathbf{c}, \mathbf{u}, \mathbf{p}, \chi) = \hat{\mathcal{J}}(\mathbf{u}) - \chi^T\Big(\mathbf{c}(t_0; \mathbf{Y}) - \mathbf{c}_0(\mathbf{Y})\Big)$$
$$- \mathbf{p}^T\Big(\mathbf{M}\dot{\mathbf{c}} + \big(\mathbf{C}_c(\mathbf{u}) + \mathbf{K}_c(t; \boldsymbol{\theta}^k)\big)\mathbf{c} - \mathbf{f}_c(t; \boldsymbol{\phi})\Big). \tag{5.17}$$

Applying the procedure as similar as in Subsection 5.1.1 we obtain the KKT optimality conditions, with the state equations are given in (5.18)–(5.19), adjoint equations in (5.20)–(5.21) and optimality condition in (5.22).

1. State equations:

$$\mathbf{M}\dot{\mathbf{c}} + \left(\mathbf{C}_c(\mathbf{u}) + \mathbf{K}_c(t; \boldsymbol{\theta}^k)\right)\mathbf{c} = \mathbf{f}_c(t; \boldsymbol{\phi}), \qquad (5.18)$$

$$\mathbf{c}(t_0; \mathbf{Y}) = \mathbf{c}_0(\mathbf{Y}). \qquad (5.19)$$

2. Adjoint equations:

$$-\mathbf{M}^T\dot{\mathbf{p}} + \left(\mathbf{C}^T(\mathbf{u}) + \mathbf{K}^T(t; \theta^k)\right)\mathbf{p} = \mathbf{M}\mathbf{c}, \qquad (5.20)$$

$$\mathbf{p}(t_f; \mathbf{Y}) = 0. \qquad (5.21)$$

3. Optimality condition:

$$\frac{\delta\mathcal{L}}{\delta\mathbf{u}} = \eta_w \int_{t_0}^{t_f} \mathbf{u}\, dt - \int_{t_0}^{t_f} \sum_{k=1}^{P} w^k \mathbf{c}^T\, \mathbf{C}(\mathbf{u})\, \mathbf{p}\, dt = 0. \qquad (5.22)$$

To solve the KKT system for stochastic control with deterministic source location, we use Algorithm 1 in Appendix B.

Discretization of the KKT system in space yields a high-dimensional discrete state-space system in the form of ODEs (Equations (5.18)–(5.22)). In addition, the collocation method and optimal control work require evaluating repeatedly the solutions of both the state and adjoint equations. Thus, these simulations are computationally expensive and may not be feasible to perform in real time. Model order reduction is applied to obtain a reduced-order approximation of the large model, which allows for efficient simulation.

5.2.2 Results

We present a 2D mathematical model to which we apply stochastic optimal control with the full model using Algorithm 1. Then we apply the model reduction to obtain the reduced-order model. We compare the stochastic optimal control result using the reduced model and the full model. Finally, we compare the behavior of the stochastic control with a deterministic control strategy.

Model Setup

To implement the stochastic contaminant transport problem, we use the same model setup as described in Section 5.1.2.

The input is a random diffusivity field κ. To generate the diffusivity coefficients under the finite dimensional noise assumption, we use the formulation similar to that in [42]. The random diffusivity coefficient is a nonlinear function of the random vector Y, namely

$$\kappa(\mathbf{x}, t; \mathbf{Y}) = \kappa_0 + \exp\left\{ \left[Y_1(\omega)\cos(\pi\eta) + Y_3(\omega)\sin(\pi\eta) \right] e^{-\frac{1}{8}} \right.$$
$$\left. + \left[Y_2(\omega)\cos(\pi\xi) + Y_4(\omega)\sin(\pi\xi) \right] e^{-\frac{1}{8}} \right\}/\sigma_Y. \qquad (5.23)$$

Here, $\boldsymbol{\theta} = (\xi, \eta) \in \mathbb{P}$ are the coordinates of the collocation points. We choose $\kappa_0 = 1/125, \sigma_Y = 200$. The initial Péclet number $Pe_0 = \frac{\|\mathbf{u}\|L}{\kappa_0} = 125$, where the length of the domain is used as the characteristic length $L = 1$. The real random variables $Y_n, n = 1, \cdots, 4$ are independent and identically distributed with zero mean value and unit variance.

Full Stochastic Control Model

The stochastic optimal control now can be solved by following Algorithm 1. To illustrate the behavior of the collocation, we simulate the unbounded random variables Y_n via the Gaussian density function. We employ the Smolyak algorithm [41, 42, 43] to determine the collocation points and collocation weights.
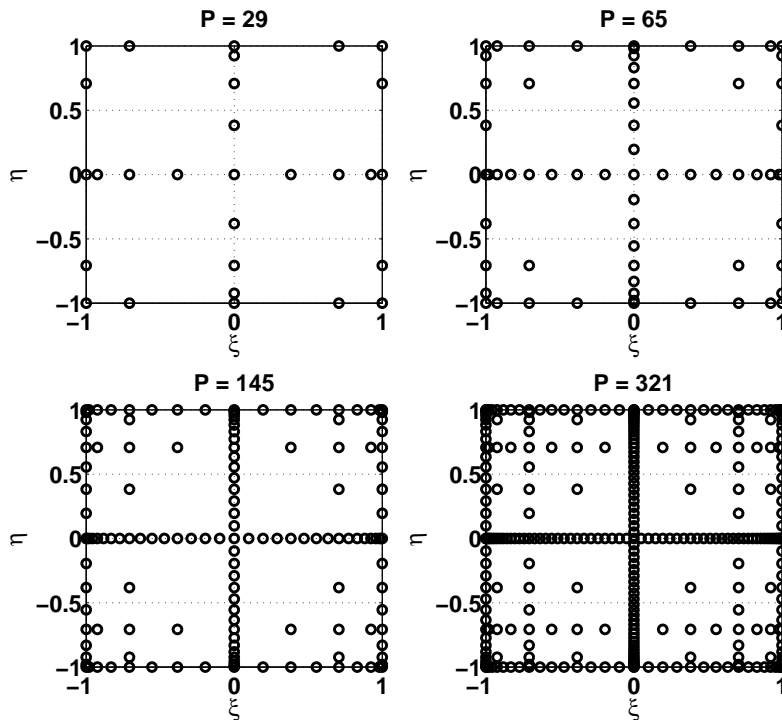
Figure 5-5: The Smolyak quadrature nodes.

We evaluate the optimal solution with Smolyak nodes which represent exactly polynomials of total degree 5 ($P = 29$), degree 7 ($P = 65$), degree 9 ($P = 145$) and degree 11 ($P = 321$) as shown in Figure 5-5. To estimate the relative error of the solution, we choose the solution corresponding to the finest collocation scheme ($P = 321$) as a "truth" solution. We then set the control parameter $\eta_w = 0.1$.

Table 5.1: Estimated optimal control for different numbers of collocation points.

P	u	v	$\hat{\mathcal{J}}$	$time_{Full}$ (hours)
29	1.350	0.0	0.312	0.9
65	1.351	0.0	0.311	2.3
145	1.351	0.0	0.311	5.0
321	1.351	0.0	0.311	9.8

Table 5.1 shows the results of the optimal control with different numbers of collocation points. Figure 5-6 shows the relative error of the stochastic optimal control solutions based on the finest solution. When the number of collocation points increases, the relative error in the estimated optimal solution decreases. However the computational time to solve the optimal control problem also increases when the number of collocation points increases [1]. We observe that the computational time is approximately 9.8 hours when $P = 321$ Smolyak nodes.
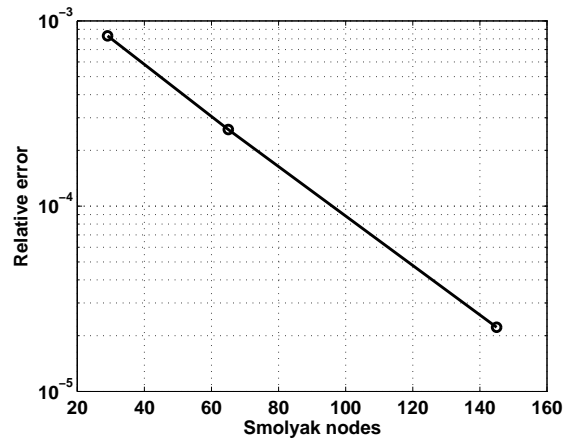
Figure 5-6: Relative error of the estimated stochastic control solution with number of collocation points.

---

[1]The simulations were performed on a personal computer (PC) with processor Intel(R) Core(TM)2 Duo CPU E8200 @2.66GHz 2.66GHz, RAM 3.25GB, 32-bit Operating System.

Reduced Stochastic Control Model

To generate the snapshots needed for the POD basis, we choose N_k evenly-spaced samples, κ_t, on the interval $[\kappa_{min} \ \kappa_{max}]$. In this example, $N_k = 10$. For each value of κ, we generate $T/2$ snapshots over the considered time horizon, where T is the number of time steps. To determine an appropriate number of POD modes we use the same energy capture as in Equation (4.15).

Table 5.2: Properties of various model reduced-order models.

$\epsilon_E(\%)$	POD	ε_{state}	$\varepsilon_{adjoint}$
99.0	18	5.48e-3	1.10e-2
99.5	21	3.45e-3	5.28e-3
99.9	30	6.28e-4	8.11e-4
99.99	46	1.13e-4	1.81e-4
99.999	65	2.05e-5	6.68e-5
99.9999	86	6.85e-6	2.39e-5

Table 5.2 shows the relative error of the approximation (for a randomly chosen value of κ not in the snapshot set) for different sizes of the reduced-order model. In practice, we need both the dimensions of the reduced-order model and the relative error to be small. Here, we choose the case with $\epsilon_E = 99.99\%$ yielding a POD basis of size $m = 46$. The outputs of interest are the values of contaminant solution c at selected sensor locations. The outputs of the full model, y, and reduced model of order $m = 46$, y_r, are shown in Figure 5-7 at sensor locations. These locations correspond to sensors in Figure 5-1. It can be seen that the magnitude of the sensor reading varies depending on the location of the sensor relative to the source. In all cases the reduced-order model is able to capture well the behavior of the full model at the sensor locations.

Applying Algorithm 1 for the reduced-order model, we obtain the optimal
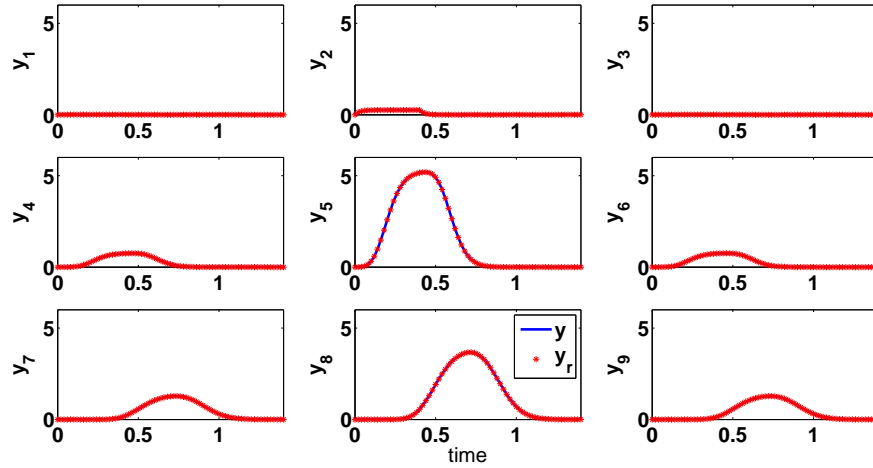
Figure 5-7: A comparison of the full model ($N = 1891$) and reduced model ($m = 46$) output of interest at sensor locations.

control result as in Table 5.3. The comparison of accuracy and computational time between the full model and reduced model are given in Table 5.4. The reduced model of order $m = 46$ has a relative error around 10^{-5}. The computational time to solve the reduced control model is decreased by approximately 80 times in comparison with the full control model.

Table 5.3: Optimal control of reduced model.

P	u	v	$\hat{\mathcal{J}}$	$time_{MOR}$ (s)
29	1.350	0.0	0.312	40
65	1.350	0.0	0.311	98
145	1.351	0.0	0.311	214
321	1.351	0.0	0.311	460

Stochastic Control vs. Deterministic Control

To make the comparison between the stochastic control and deterministic control, we choose the solution of the stochastic control at the degree of polynomial 9 or $P = 145$ Smolyak nodes. We then choose a subset of Smolyak nodes in

Table 5.4: Relative error between full control and reduced control solutions and speedup factor of full model vs. reduced order model corresponding collocation points.

P	$\varepsilon_{\mathbf{u}}$	$\frac{time_{Full}}{time_{MOR}}$
29	5.38e-5	81
65	1.41e-5	83
145	2.27e-5	84
321	1.42e-5	76

the collocation space $\mathbb{P}$, for example we choose $\mathbb{P}_S \in \mathbb{P}$ such that $-1 \leq \xi \leq 1$ and $\eta = -1$. For each pair $\boldsymbol{\theta}^k = (\xi, \eta)$ we compute the diffusivity coefficient $\kappa(\mathbf{x}, t; \mathbf{Y})$. We then compute the deterministic optimal control for the mean value of κ to find the optimal velocity and estimate its cost functional. Figure 5-8 shows that the stochastic optimal control always has the value above the average of the set of deterministic control.
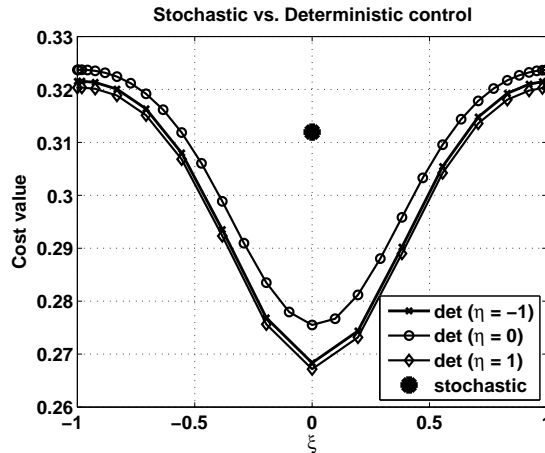
Figure 5-8: Stochastic control vs. deterministic control.

5.2.3 Remarks

This study has applied the combination of model order reduction techniques based on POD and an adjoint-based method to solve a stochastic optimal con-

trol problem. The reduced model with order $m = 46$ decreases the computational time of solution by a factor of about 80 while retaining acceptable accuracy with a relative error of around 10^{-5} as compared to the full model with size $N = 1891$. This speedup is important in real-time decision-making applications because it provides a rapid solution and reduces time cost and storage requirements. Application of the optimal control strategy shows the potential effectiveness of this computational modeling approach for managing flow quality.

We have already studied stochastic optimal control for a deterministic contaminant source. In the next section, we consider the case where the contaminant source is uncertain.

5.3 Stochastic control for uncertain contaminant source location

We assume that under the influence of uncertain parameters such as wind speed, contaminant sources become uncertain. Before we can apply any control to flush the contaminant out of the domain, we have to determine the source locations first. In this section, the stochastic estimation problem is first considered. The stochastic optimal control problem is then described. We shall use a numerical example to demonstrate the solution of stochastic problems and the reduced-order model performance.

5.3.1 Problem Description

Consider the fluid flows through a physical domain $\mathcal{D} \in \mathbb{R}^2$ with boundary condition and initial conditions as described in Subsection 2.4.3. The stochastic contaminant transport with boundary condition and initial conditions are given in (2.61)–(2.64). The stochastic collocation method with the finite element method approximates this SPDE problem. Our problem is now stated as: given a set of contaminant measurements $\mathbf{y} = \{y_1, y_2, \cdots, y_{N_o}\}$ in the domain, we want to determine contaminant source locations and apply a control to flush them out of the domain.

5.3.2 Stochastic estimation problems

The relationship between the state of contaminant concentration to be estimated from the physical model and the measurements is given by

$$\mathbf{y} = G(\boldsymbol{\phi}) + \boldsymbol{\eta}_t, \tag{5.24}$$

where $\mathbf{y} \in \mathbb{R}^{N_o}$ is the measurement vector (e.g. concentration measurements), the source location $\boldsymbol{\phi} \in \boldsymbol{\Phi}^s \subseteq \mathcal{D}$ is the input parameter set, and $\boldsymbol{\eta}_t \in \mathbb{R}^{N_q}$ the vector noise. The input-output in Equations (2.71)–(2.72) is denoted as the forward model $G(\boldsymbol{\phi})$, which maps the inputs $\boldsymbol{\phi}$ to outputs $\mathbf{y}$.

Bayesian formulation of the inverse problem

The Bayesian solution to the above problem is to obtain an estimate $\hat{\phi}$ of ϕ based on measured data, using Bayes's rule

$$p(\phi|\mathbf{y}) = \frac{p(\mathbf{y}|\phi)p(\phi)}{p(\mathbf{y})}. \tag{5.25}$$

Here the density function $p(\phi|\mathbf{y})$ is known as the posterior density function of ϕ. The density function $p(\phi)$ is the prior distribution of the parameter, reflecting our prior knowledge on the possible source location. The density function $p(\mathbf{y}|\phi)$ is the likelihood function. If we assume vector noise $\boldsymbol{\eta}_t$ to be additive white Gaussian noise $\boldsymbol{\eta}_t \sim N(0, \sigma^2 I)$, the likelihood function can be written as

$$p(\mathbf{y}|\phi) = \frac{1}{\sigma\sqrt{2\pi}} \exp(-\frac{1}{2\sigma^2}\|\mathbf{y} - G(\phi;\omega)\|^2). \tag{5.26}$$

There are many different ways to incorporate prior information such as Gaussian Markov random field (MRF) model, beta distribution model, etc. In this work, we assume that our only prior information on the source location is given by the bounds on the domain. Thus, using the Principle of Maximum Entropy [93] we take our prior to be a uniform distribution. If more information were available, our approach admits other prior distributions. Therefore, Equation (5.25) becomes

$$p(\phi|\mathbf{y}) \propto \begin{cases} \prod_{i=1}^{K} \exp\left[-\frac{1}{2\sigma^2}\left(\mathbf{y}_i - G(\phi;\omega)_i\right)^T\left(\mathbf{y}_i - G(\phi;\omega)_i\right)\right], & \forall \phi \in \mathcal{D} \\ 0, & \text{otherwise,} \end{cases} \tag{5.27}$$

where $\mathcal{D}$ is the support the (uniform) prior distribution of ϕ. Here, K is the number of time steps in the collected output data. To perform the Bayesian computation, we use the Markov chain Monte Carlo method. In the next subsection we shall briefly introduce this method.

Markov chain Monte Carlo

The Markov chain Monte Carlo (MCMC) provides a sampling strategy from the proposal distribution $q(\phi|\mathbf{y}, \phi^{(t-1)})$ to the target distribution $p(\phi|\mathbf{y})$ using the Markov chain [94]. In this work, the Metropolis-Hastings (MH) algorithm is used to solve the Bayesian inverse problems. Suppose that our goal is to sample from the target distribution $p(\phi|\mathbf{y})$ with $\phi \in \mathcal{D}$. The Metropolis sampler generate a Markov chain with a sequence of values: $\phi^{(1)} \rightarrow \phi^{(2)} \rightarrow \cdots \rightarrow \phi^{(t)} \rightarrow \cdots$, where $\phi^{(t)}$ is the state of a Markov chain at iteration t. The Metropolis procedure is to initialize the first state $\phi^{(1)}$, then to use a proposal distribution $q(\phi|\mathbf{y}, \phi^{(t-1)})$ to generate a candidate value ϕ^*. The next step is either accept the proposal or reject it. New proposals is then generated and this procedure continues until the sampler reaches convergence. The samples $\phi^{(t)}$ now reflect samples from the target distribution $p(\phi|\mathbf{y})$. The MH algorithm is summarized below as follows,

Algorithm 2

1. Initialize the chain ϕ^0 and set $t = 0$

2. Repeat

   - $t = t + 1$

88

- Generate a proposal point $\phi^* \sim q(\phi^*|\mathbf{y}, \phi)$

- Generate u_a from a Uniform(0,1) distribution

- Update the state to ϕ^{t+1} as

$$\phi^{t+1} = \begin{cases} \phi^*, \text{ if } \beta_a < u_a \\ \\ \phi^t, \text{ otherwise} \end{cases}$$

3. Until $t = N_{mcmc} \rightarrow$ stop.

Here, β_a is the acceptance-rejection ratio, given by

$$\beta_a = \min\left(1, \frac{p(\phi^*|\mathbf{y})q(\phi^{t-1}|\mathbf{y}, \phi^*)}{p(\phi^{t-1}|\mathbf{y})q(\phi^*|\mathbf{y}, \phi^{t-1})}\right). \tag{5.28}$$

N_{mcmc} is the total number of samples and u_a is a random number from Uniform(0,1) distribution.

Once the samples or the posterior probability density of source location are determined, we have a characterization of the probable location of the source. Then we can apply the control stochastic control. However, applying the stochastic control on the probable regions will be extremely expensive even with the reduced-order model used. Here we explore the Gaussian mixture model (GMM) to approximate the posterior density function of the source before applying the control.

Gaussian mixture model

Given the data set $\boldsymbol{\Phi} = \{\phi_n\}_{n=1}^{N_c}$ samples from the posterior density function, the next step is to approximate this data using Gaussian mixture model (GMM). A mixture of Gaussians is defined by a superposition of N_G Gaussian densities

in the form

$$p_G(\phi|\Xi) \equiv p(\phi|\mathbf{y}) \approx \sum_{k=1}^{N_G} \pi_k^m \mathcal{N}(\phi|\bar{\phi}_k, \Sigma_k). \qquad (5.29)$$

Here the parameter list $\Xi = \pi_1^m, \cdots, \pi_{N_G}^m, \bar{\phi}_1, \cdots, \bar{\phi}_{N_G}, \Sigma_1, \cdots, \Sigma_{N_G}$ defines a particular Gaussian mixture probability density function. Each Gaussian density $\mathcal{N}(\phi|\bar{\phi}_k, \Sigma_k)$ is called a component of the mixture and has its own mean $\bar{\phi}_k$ and covariance Σ_k, which has the form

$$\mathcal{N}(\phi|\bar{\phi}_k, \Sigma_k) = \frac{1}{(2\pi)^{d/2}} \frac{1}{|\Sigma_k|^{1/2}} \exp\left\{ -\frac{1}{2}(\phi - \bar{\phi}_k)^T \Sigma_k^{-1}(\phi - \bar{\phi}_k)\right\}, \quad (5.30)$$

where d is the dimension of vector ϕ and $|\Sigma|$ denotes the determinant of Σ. The coefficients π_k^m are called mixing coefficients, which have two properties:

$$\begin{cases} \sum_{k=1}^{N_G} \pi_k^m = 1, \\ 0 \leq \pi_k^m \leq 1, \end{cases} \qquad (5.31)$$

that satisfy the requirements of probabilities.

The likelihood of the data set $\mathbf{\Phi} = \{\phi_n\}_{n=1}^{N_c}$ assuming that ϕ_n are independently distributed is given by

$$p_G(\mathbf{\Phi}|\Xi) = \prod_{n=1}^{N_c} p_G(\phi_n|\Xi). \qquad (5.32)$$

From (5.29) the log of the likelihood function is given by

$$\ln p_G(\mathbf{\Phi}|\Xi) = \sum_{n=1}^{N_c} \ln\left\{ \sum_{k=1}^{N_G} \pi_k^m \mathcal{N}(\phi_n|\bar{\phi}_k, \Sigma_k)\right\}. \qquad (5.33)$$

Our task is to find the maximum of the likelihood function (5.33) with respect to the parameters of the GMM. The expectation-maximization (EM) algorithm is a general method for finding maximum likelihood estimates with respect to the parameters (comprising the means and covariances of the components and the mixing coefficients). For more details, refer to [95].

5.3.3 Stochastic optimal control problems

Given our approximate representation of the unknown source using our GMM, the next step is to solve the control. The goal of our control problem is to flush the contaminant out of the domain by controlling the velocity of the fluid pump.

Objective functional

The objective functional is to seek a velocity over an admissible control set $\mathbf{u} \in U_{ad}$ that minimizes a weighted combination of the L_2-norm of the expected contaminant field and the L_2-norm of the velocity field:

$$\min_{\mathbf{u} \in U_{ad}} \hat{\mathcal{J}}(\mathbf{u}, c) = \frac{1}{2} \int_{t_0}^{t_f} \mathbb{E}\left[\|c(\mathbf{x}, t, \boldsymbol{\phi}; \omega)|\mathbf{y}\|_{L_2}^2\right] dt + \frac{\eta_w}{2} \int_{t_0}^{t_f} \|\mathbf{u}\|_{L_2}^2 dt, \quad (5.34)$$

subject to the constraints Equations (2.61)–(2.64). Here, η_w is a constant controlling the relative weighting of the components of the objective function, $\mathbb{E}[\cdot]$ denotes the expectation operator and $\mathbf{y}$ the measurement vector.

In the stochastic estimation framework, the expected value is simply the

mean of the posterior density function [96, 97]. That is,

$$\mathbb{E}[\phi|\mathbf{y}] = \int_{\Phi} \phi \, p(\phi|\mathbf{y}) \, d\phi. \tag{5.35}$$

Consider the expected contaminant field in (5.34), a similar manner to (5.35) we have

$$\mathbb{E}\left[\|c(\mathbf{x}, t, \phi; \omega)|\mathbf{y}\|_{L_2}^2\right] = \int_{\Phi} \|c(\mathbf{x}, t, \phi; \omega)\|_{L_2}^2 \, p(c(\mathbf{x}, t, \phi; \omega)|\mathbf{y}) \, d\phi. \tag{5.36}$$

The posterior density function of the contaminant field $c(\mathbf{x}, t, \phi; \omega)$ is estimated implicitly via the contaminant source ϕ. Thus, we can re-write (5.36) as

$$\mathbb{E}\left[\|c(\mathbf{x}, t, \phi; \omega)|\mathbf{y}\|_{L_2}^2\right] \approx \int_{\Phi} \|c(\mathbf{x}, t, \phi; \omega)\|_{L_2}^2 \, p(\phi|\mathbf{y}) \, d\phi. \tag{5.37}$$

Combining Equations (5.29) and (5.37), we get

$$\mathbb{E}\left[\|c(\mathbf{x}, t, \phi; \omega)|\mathbf{y}\|_{L_2}^2\right] \approx \sum_{j=1}^{N_G} \pi_j \, \mathbb{E}\left[\|c(\mathbf{x}, t, \bar{\phi}_j; \omega)\|_{L_2}^2\right]. \tag{5.38}$$

In the collocation framework, the expected value in (5.38) is approximated via a quadrature rule (such as Clenshaw–Curtis quadrature [92]) built on the collocation points. Define $\left\{w^k\right\}_{k=1}^{P}$ to be the quadrature weights associated with the collocation points,

$$w^k = \int_{\Theta} \rho(\mathbf{Y}) \, L_k^2(\boldsymbol{\theta}) \, d\boldsymbol{\theta}, \quad \text{for } k = 1, \cdots, P, \tag{5.39}$$

where $\rho(\mathbf{Y})$ is the probability density of the random vector $\mathbf{Y}$. The cost func-

tional is replaced by the discretized problem as follows

$$
\min_{\mathbf{u} \in U_{ad}} \hat{\mathcal{J}}(\mathbf{u}) \approx \frac{1}{2} \int_{t_0}^{t_f} \left[\sum_{j=1}^{N_G} \pi_j^m \left[\sum_{k=1}^{P} w^k \mathbf{c}^T(t, \bar{\boldsymbol{\phi}}_j; \mathbf{Y}) \mathbf{M} \mathbf{c}(t, \bar{\boldsymbol{\phi}}_j; \mathbf{Y}) \right] \right] dt
$$

$$
+ \frac{\eta_w}{2} \int_{t_0}^{t_f} \|\mathbf{u}\|_{L_2}^2 \, dt. \tag{5.40}
$$

Here, the solution $\mathbf{c}(t, \bar{\boldsymbol{\phi}}_j; \mathbf{Y}), j = 1, \cdots, N_G; k = 1, \cdots, P$, solves the ordinary differential equations (ODEs) (2.71)–(2.72).

The Optimality System

The optimality system is derived in a similar manner to Subsection 5.2.1. Only the optimality condition equation is slightly different, which is given as

$$
\frac{\delta \mathcal{L}}{\delta \mathbf{u}} = \eta_w \int_{t_0}^{t_f} \mathbf{u} dt - \int_{t_0}^{t_f} \sum_{j=1}^{N_G} \pi_j^m \sum_{k=1}^{P} w^k \mathbf{c}^T \mathbf{C}(\mathbf{u}) \mathbf{p} \, dt = 0. \tag{5.41}
$$

In summary, the state equation (5.18)–(5.19), adjoint equation (5.20)–(5.21) and optimality condition (5.41) form the optimality system, solutions of which provide the optimal state $\mathbf{c}$, adjoint state $\mathbf{p}$ and control variable $\mathbf{u}$. To solve the stochastic optimal control problem using the collocation method we use Algorithm 1 in Appendix B.

As mentioned in Subsection 5.2.1, these simulations in real-time are computationally expensive and may not be feasible. Model order reduction is applied to obtain a reduced-order approximation of the large model, which allows for efficient simulation.

5.3.4 Results

We present a 2D mathematical model to evaluate the efficiency of the proposed approach to the application of water management. The reduced order models are first determined to serve as an efficient forward solver in the stochastic estimation problem and stochastic optimal control problem. That solver is then employed to find the realization of source locations using Algorithm 2 and the optimal solution of velocity using Algorithm 1. We shall follow the same model setup from Section 5.2.2.

Full order model and reduced order model

To illustrate the behavior of the collocation approach, we employ the Smolyak algorithm [41, 42, 43] to determine the collocation points $\left\{\boldsymbol{\theta}^k\right\}_{k=1}^K = (\xi, \eta)^k$ and collocation weights $\left\{w^k\right\}_{k=1}^K$. For each pair of $(\xi, \eta)^k$, the diffusivity κ^k is determined and then candidate solution $\mathbf{c}(t, \bar{\boldsymbol{\phi}}_j, \mathbf{Y})$.

We evaluate the candidate solutions with Smolyak nodes which represent exactly polynomials of total degree 5 ($P = 29$), degree 7 ($P = 65$), degree 9 ($P = 145$) and degree 11 ($P = 321$) as shown in Figure 5-5. Solution of the stochastic convection-diffusion equation is global approximation of the candidate solutions at collocation points as given in Equation (2.66).

The POD method is then implemented to generate a POD basis from a set of snapshots. The snapshot are taken not only at different time instants but also for different realizations of source locations and for different realizations of diffusivity coefficients using independent random inputs. In this case, we choose N_k evenly-spaced samples, κ_t, on the interval $[\kappa_{min} \ \kappa_{max}]$, and a sample

94

set of source locations, S_k. To increase the efficiency of the snapshot collection we use the following strategy: for each value of κ_t we generate S_k values of randomly source locations over $\mathcal{D}$, and for every two time-steps we store one instantaneous solution. Here, $N_k = 10$ and $S_k = 30$ samples. The total number of snapshots is $N_{snap} = N_k \times S_k \times T/2$.

Table 5.5: Properties of various MOR models.

$\epsilon_E(\%)$	POD	ε_{state}	$\varepsilon_{adjoint}$
98.5	86	3.64e-3	1.24e-2
99.0	97	2.82e-3	3.78e-3
99.5	118	1.73e-3	1.46e-3
99.9	169	7.28e-4	7.98e-4
99.99	250	2.48e-4	8.96e-5

Table 5.5 shows the relative error of the approximation (for a randomly chosen value of κ and source location not in the snapshot set) for different sizes of the reduced-order model. The size of reduced-order model is chosen based on the snapshot energy as in Equation (4.15). In practice, we need both the dimensions of the reduced-order model and the relative error to be small. Here, we choose the case with $\epsilon_E = 99.0\%$ yielding a POD basis of size $m = 97$. The solution of SPDEs is evaluated for both full forward model and reduced-order model with order $m = 97$. We observe that the computational time of the full model is approximately 9 minutes when $P = 321$ Smolyak nodes [2].

To estimate the relative error of the solution, we choose the solution corresponding to the finest collocation scheme ($P = 321$) as a "truth" solution. Table 5.6 shows the relative errors and computational time ratio of the full model and reduced model (defined as $r_t = \frac{t_{Full}}{t_{MOR}}$) for different Smolyak nodes. We

---

[2]The simulations were performed on a personal computer (PC) with processor Intel(R)

Table 5.6: Estimated solution of SPDEs for different numbers of collocation points.

P	ε_{error}	r_t
29	2.53e-3	25
65	2.51e-3	25
145	2.51e-3	24
321	2.51e-3	26

observe that the relative errors of estimated solutions are decreased when the number of collocation points increases. However, these relative errors do not change very much. Furthermore, the ratio of computational time is speed-up with a similar factor — 25 times. We choose the second case with $P = 65$ Smolyak nodes. Next, our reduced model will be utilized as an efficient forward solver in the stochastic estimation and stochastic optimal control problems.

Stochastic estimation problems

We assumed that at the beginning we are given a set of measured data as shown in Figure 5-9. These data can be collected by experimentation or simulation. In this case, we simulate the deterministic model by assuming $\kappa(\mathbf{x}, t; \mathbf{Y}) = \kappa_0$ and source location $\phi = (0.3,\ 0.25)$. To illustrate the behavior of uncertain variables such as wind velocity into the model, we add noise into the ideal data. The noise is assumed to be additive white Gaussian noise $\boldsymbol{\eta}_t \sim N(0, \sigma^2 I)$ with $\sigma = 0.2$.

The Bayesian formulation and MCMC approach is now used to solve for variety of source locations using the reduced solver above. We conduct the MCMC simulation with the starting point $\phi_{ini} = (0.5; 0.2)$. The total number

Core(TM)2 Duo CPU E8200 @2.66GHz 2.66GHz, RAM 3.25GB, 32-bit Operating System.
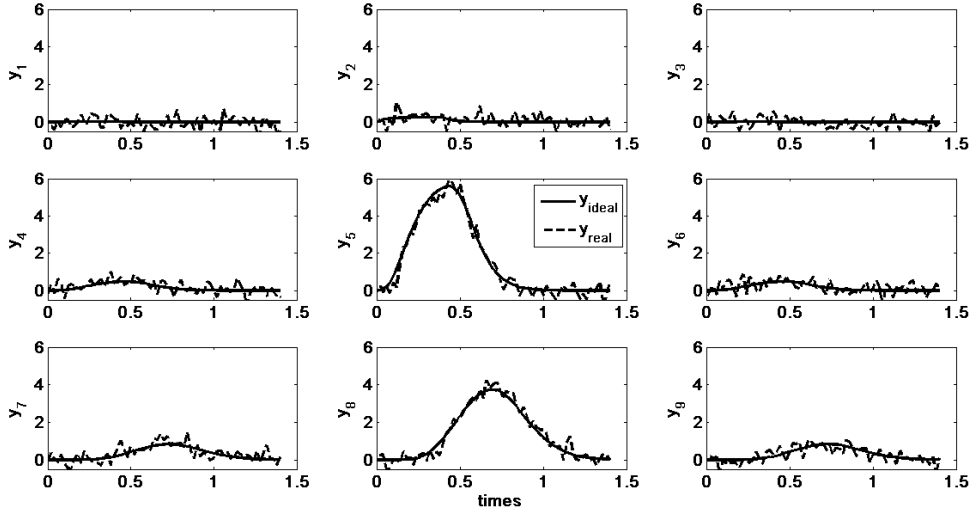
Figure 5-9: A set of synthetic data.

of MCMC samples is set to $N_{mcmc} = 5000$. The initial burn-in period is set to $N_{burnin} = 1000$. After this stage, data is saved to compute the statistics of source locations.

Figure 5-10(a) shows the trace plot (or history plot) of the parameters versus the iteration numbers. Based on these plots we can estimate whether the Markov chain has converged. The Markov chain for both parameters ϕ_1 and ϕ_2 is used beginning at the starting point $\phi_{ini} = (0.5; 0.2)$. The acceptance ratio at 67.6% is consistent with the recommended range between 30% to 70% as suggested in [98].

Figure 5-10(b) shows the posterior probability density of the source location ϕ. In this figure, both pairwise scatter plot and one-dimensional marginal distributions are displayed. The dashed-line on each axis shows the probability density function of each parameter. The contours show the posterior probability density of source location ϕ (the probable regions) while red-dot is the actual source location for which the measured data are synthesized. The computational

97

(a) Trace plot (b) Scatter plot
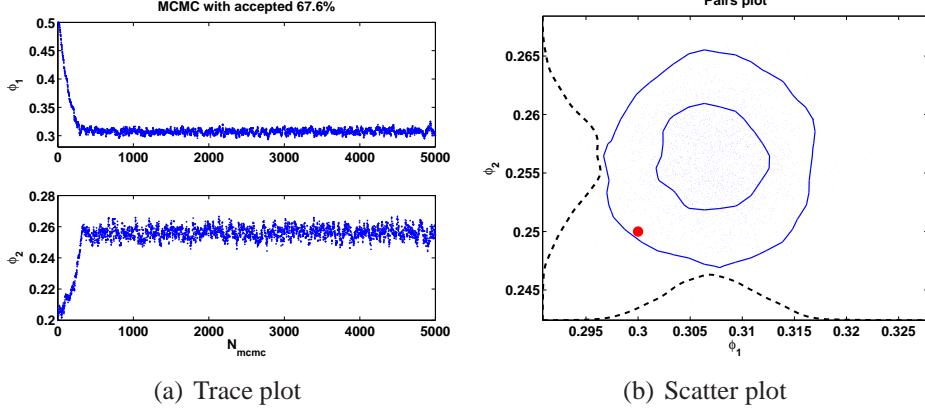
Figure 5-10: Trace plots and scatter plot of parameters ϕ_1 and ϕ_2.

time to solve the inverse problem is approximately 6 hours. (If we use the full forward solver, with the speed-up factor of around 25 times, the computational time is estimated at around 150 hours or approximately 6 days.)

Next, we employ the Gaussian mixture models (GMM) to approximate the posterior density function of the estimated source location before applying the stochastic optimal control to flush them out of the domain. From the probable regions, we used the GMM to approximate the mean, covariance and mixing coefficients of Gaussian components. Figure 5-11 show the Gaussian mixture models with 1, 2, 3 and 4 Gaussian components, respectively. Table 5.7 shows the mean $(\bar{\phi})$ of the components and mixing coefficients, which maximizes the likelihood of Gaussian mixtures. The covariance is different for each Gaussian component, for example, $\Sigma_1 = 1.0e^{-3} \times [1.5, -0.42; -0.42, 0.91]$, but $\Sigma_4 = 1.0e^{-3} \times [0.79, 0.25; 0.25, 0.59]$.

Stochastic optimal control problems

The stochastic optimal control now can be solved by following Algorithm 1 as described in Appendix **B**. In this example, we set the control parameter
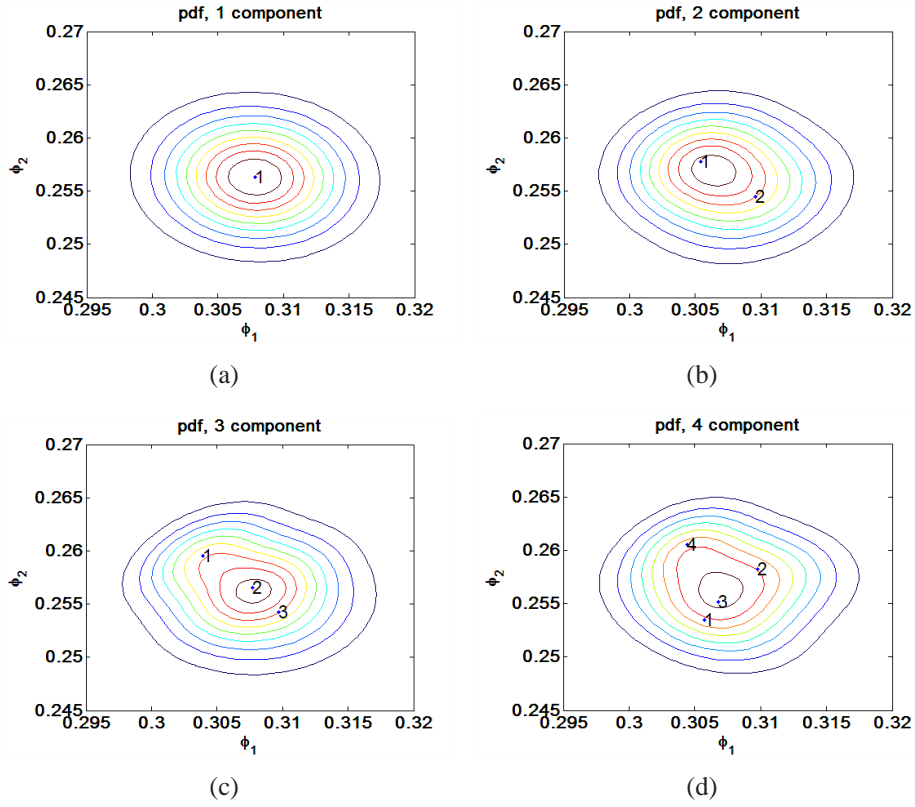
Figure 5-11: Gaussian mixture models with 1, 2, 3 and 4 Gaussian components, respectively.

Table 5.7: Gaussian mixture model with 4 Gaussian components.

Parameters	GMM_1	GMM_2	GMM_3	GMM_4
ϕ_1	0.3061	0.3100	0.3071	0.3048
ϕ_2	0.2530	0.2578	0.2547	0.2600
π^m	0.2200	0.3733	0.2467	0.1601

$\eta_w = 0.1$. We will perform our control using the Gaussian mixture models with

$1, 2, 3$ and 4 components. Table 5.8 shows the results of the optimal control with

Table 5.8: Estimated optimal control for different numbers of mixtures in the GMM.

N_G	u	v	$\hat{\mathcal{J}}$	time (min)
1	1.38	0.00	0.329	4.5
2	1.39	-0.02	0.331	18.2
3	1.39	0.03	0.334	32.1
4	1.41	0.04	0.345	48.4

99

different numbers of Gaussian components. We observe that when the number of mixtures in the GMM increases the amplitude of the estimated optimal velocity increases and its estimated cost functional increases. The computational time to solve the stochastic control increases when the number of mixtures in the GMM increases. We observe that the computational time is approximately 50 minutes when $N_G = 4$, using our reduced-solver. If we use the full solver, the computational time is around 1 day according to the speed-up factor given in Table 5.6.

Figure 5-12 shows the efficiency of the management when applying the control. With the determined control strategy, the contaminant is almost flushed out of the domain at the same final time.

(a) With Control   (b) Without Control
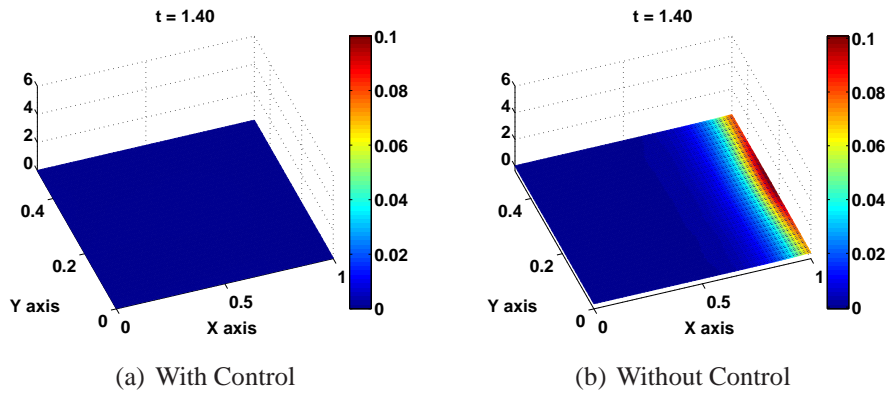
Figure 5-12: The contaminant field with control and without control for case $N_G = 4$.

5.3.5 Remarks

This study has applied the combination of model order reduction technique based on POD and the collocation method to solve a stochastic measure-invert-control problem. A Bayesian formulation for the inverse problem solved us-

ing MCMC together with a reduced-order solver provides a rapid estimate of the probability density function of the parameters describing source location. Gaussian mixture model is then applied to determine a number of mixtures in the GMM which is able to cover the probable regions well. Stochastic optimal control based on collocation and adjoint method provides a rapid solution to the control problem. The reduced solver with order $m = 97$ decreases the computational time of solution by a factor of about 25 while retaining acceptable accuracy. This speed up is important in real-time decision-making applications because it provides a rapid solution and reduces storage requirements. Application of the optimal control strategy shows the potential effectiveness of this computational modeling approach for managing flow quality.

Chapter 6

Conclusions and Future Work

6.1 Conclusions

Understanding of hydrodynamic processes such as contaminant transport, mixing water, and thermal stratification provides knowledge to the management of quality in reservoir system. These processes strongly influence water quality under the effect of parameters such as water velocities, wind velocity and heat exchange at the air-water interface. Of particular significance is contaminant transport, which may contain many species of pollution, that directly affect the water quality. Since the contaminant may exist in point-source or nonpoint-source forms, locating and estimating of the contaminant sources are required before we can apply the control to 'clean' or 'get rid of' them. For large-scale and realistic applications such as reservoirs, experiments for these works can be very costly. Experiments via numerical simulations provide an alternative tool for detailed analysis and evaluation. To perform the control, we have to deal with many uncertain parameters relating to the instrumentations which measure the

wind speed, water circulation currents, contaminant species and others. These uncertain parameters may have undue influence on the system. As such these need to be properly accounted for as stochastic variables in the system model. In this study, we explored an end-to-end: measure-invert-control strategy for a stochastic problem with application to the management of quality in reservoir system. Due to the stochastic nature of the simulations and optimization formulation, the computational costs and storage requirements increase rapidly. An efficient reduced-order model that approximates the full model can overcome this computational issue.

With this strategy, we first develop a numerical simulation code for 2D laterally averaged model for lake and reservoir models. The numerical code is validated through comparisons to benchmark problems. Numerical results show that the hydrodynamics processes are in good agreement with the theoretical and experimental data. The physical phenomena are also investigated and compared to practice. Data collected is then processed in the measurement step. Here we used data from numerical simulations and added some noise. The inverse problem step is then performed using a Bayesian formulation and solved with a Markov chain Monte Carlo method. After that the Gaussian mixture models are used to determine a number of mixtures in the GMM. Finally the stochastic control step using the adjoint method together with a collocation method is applied to 'flush' the contaminant out of the reservoir.

The reduced-order model for the reservoir system is obtained using the proper orthogonal decomposition and Galerkin projection techniques. For dependent variable or non-linear problems, we have to use a combination of Galerkin pro-

jection method and POD directly on the coupled Navier-Stokes equations and transport equation that yield a set of ordinary differential equations capturing the essential dynamics of the system. To demonstrate the efficiency of reduced-order models, two examples are considered. The first is a simple 2D transport model with constant velocity field and the second is a coupled Navier-Stokes and transport model. In both cases, the final purpose is to 'flush' the contaminant out of the domain with the lowest cost. The first study has applied successfully the combination of model order reduction technique based on POD and the collocation method to solve the stochastic problems. A Bayesian formulation for the inverse problem solved using MCMC together with a reduced-order solver provides a rapid estimate of the probability density function of the parameters describing source location. Gaussian mixture model is then applied to determine a number of mixtures in the GMM which is able to cover the probable regions well. Stochastic optimal control based on collocation and adjoint method provides a rapid solution to the control problem. The reduced solver with order m = 97 decreases the computational time of solution by a factor of about 25 while retaining acceptable accuracy in comparison with the full model with size $N = 1891$. This speedup is important in real-time decision-making applications because it provides a rapid solution and reduces storage requirements. For coupled Navier-Stokes and transport model, the POD-based ROMs has been studied and applied successfully for the simulation of fluid flow. This approach provides an efficient method to deal with nonlinear and coupled systems. In this study, the speedup factor is approximately 90 using reduced models with $M_u = 12$ and $M_c = 20$ POD basis vectors in comparison with the full model with size

$N = 2121$. The controlled actions provide a cleaner water body than uncontrolled actions. Due to the significant savings in computational costs and storage requirements and the effectiveness of the optimal control, the POD-based ROMs is able to provide an effective tool for water quality management.

6.2 Future Work

The 2D laterally averaged model is able to provide solutions with adequate accuracy. However the most environmental flows are three-dimensional models; they require general solutions. Our numerical code has been developed for 2D model and it can readily be extended into 3D model. With 3D model we can explore in great details the movement of water and find out the "dead zones", which increase residence time of contaminant and augment the risk of recontamination within the reservoir.

The stochastic optimal control of outflow velocity to clean up the contaminant in a reservoir is our next target. We have already developed the approach for a deterministic control. We need to extend the code to other realistic problems: the stochastic control of reservoir problems. Presently, we can only control for all the outflows with the same factor. We have to modify the approach so that we can control each outflow separately in order to increase flexibility.

Bibliography

[1] P. Shanahan. Water temperature modeling: A practice guide. In Proceedings Stormwater and Water Quality Model Users Group Meeting, pages 1–13, April 1984.

[2] A. Techet. Hydrodynamics (class code 2.016). Lecture notes on marine hydrodynamics for MIT Mechanical Engineering student, 2005.

[3] J. Imberger and J. C. Patterson. A dynamic reservoir simulation model DYRESM. In H. B. Fisher, editor, *Transport Models for Inland and Coastal waters*, Proceedings of a Symposium on Predictive Ability, pages 310–361. Academic Press, New York, October 1981.

[4] T. M. Cole and E. M. Buchak. *CE-QUAL-W2: A two-dimensional, laterally averaged, hydrodynamic and water quality model, Version 2.0.* US Army Engineer Waterways Experiment Station, Vicksburg, MS, users manual, instruction report el-95-1 edition, 1994.

[5] R. R. Gu and S. W. Chung. A two-dimensional model for simulating the transport and fate of toxis chemicals in a stratified reservoirs. *J. Environ. Qual.*, 32:620–632, 2004.

[6] D. S. Sivia and J. Skilling. *Data Analysis: A Bayesian Tutorial*. Oxford University Press, second edition, 2006.

[7] A. Tarantola. *Inverse Problem Theory and Methods for Model Parameter Estimation*. SIAM, 2004.

[8] N. Metropolis and S. Ulam. The Monte Carlo method. *Journal of the American Statistical Association*, 44:335–341, 1949.

[9] N. Metropolis, A. W. Rosenbluth, M. N. Rosenbluth, A. H. Teller, and E. Teller. Equations of state calculations by fast computing machines. *Journal of Chemical Physics*, 21:1087–1092, 1953.

[10] W. K. Hastings. Monte Carlo sampling methods using Markov chains and their applications. *Biometrika*, 57:97–109, 1970.

[11] A. Gelman, J. Carlin, H. Stern, and D. Rubin. *Bayesian Data Analysis*. Chapman and Hall/CRC, second edition, 2003.

[12] Z. G. Ji. *Hydrodynamics and Water Quality: Modeling Rivers, Lakes, and Estuaries*. John Wiley and Sons, 2007.

[13] J. L. Martin and S. C. McCutcheon. *Hydrodynamics and Transport for Water Quality Modeling*. Taylor and Francis, New York, 1999.

[14] G. T. Orlob. *Mathematical Modeling of Water Quality: Streams, Lakes, and Reservoirs*. John Wiley and Sons, New York, 1983.

[15] H. Rubin and J. Atkinson. *Environmental fluid mechanics*. Marcel Dekker, Inc. New York, 2001.

[16] V. Akcelik, G. Biros, A. Drananescu, O. Ghattas, J. Hill, and B. van Bloemen Waanders. Dynamic data-driven inversion for terascale simulations: Real-time identification of airborne contaminants. Proceedings of SC2005, Seattle, WA, November 2005.

[17] V. Akcelik, G. Biros, O. Ghattas, K. R. Long, and B. van Bloemen Waanders. Variational finite element method for source inversion for convective-diffusive transport. *Finite Elements in Analysis and Design*, 39:683–705, 2003.

[18] S. M. Gorelick, B. Evans, and I. Remson. Identifying sources of groundwater pollution: An optimization approach. *Water Resour. Res.*, 19(3):779–790, 1983.

[19] J. Atmadja and A. C. Bagtzoglou. State of the art report on mathematical methods for groundwater pollution source identification. *Environ. Forens.*, 2:205–214, 2001.

[20] C. Jackson, M. K. Sen, and P. L. Stoffa. An effcient stochastic Bayesian approach to optimal parameter and uncertainty estimation for climate model predictions. *Journal of Climate*, 17:2828–2841, 2004.

[21] Y. M. Marzouk, H. N. Najm, and L. A. Rahn. Stochastic spectral methods for efficient Bayesian solution of inverse problems. *Journal of Computational Physics*, 224(2):560–586, 2007.

[22] M. F. Snodgrass and P. K. Kitanidis. A geostatistical approach to contaminant source identification. *Water Resour. Res.*, 33(4):537–546, 1997.

[23] A. D. Woodbury and T. J. Ulrych. A full-Bayesian approach to the groundwater inverse problem for steady state flow. *Water Resour. Res.*, 36(1):159–171, 2000.

[24] J. Wang and N. Zabaras. Hierarchical Bayesian models for inverse problems in heat conduction. *Inverse Problems*, 21:183–206, 2005.

[25] J. W. Nicklow and L. W. Mays. Optimal control of reservoir releases to minimize sedimentation in rivers and reservoirs. *Journal of the American Water Resources Association*, 37(1):197–211, 2001.

[26] D. G. Fontane, J. W. Labadie, and B. Loftis. Optimal control of reservoir discharge quality through selective withdrawal. *Water Resour. Res.*, 17(6):1594–1602, 1981.

[27] N. Zeitouni. *Efficient management of groundwater quality: an evaluation of spatially differentiated policies*. PhD dissertation, University of Rhode Island, Resources Economics, 1991.

[28] M. G. Bhat, K. R. Fister, and S. Lenhart. An optimal control model for the surface runoff contamination of a large river basin. *Natur. Resource Modeling*, 12:175–195, 1999.

[29] L. J. Alvarez-Vazquez, A. Martinez, M. E. Vazquez-Mendez, and M. A. Vilar. An application of optimal control theory to river pollution remediation. *Applied Numerical Mathematics*, 59:845–858, 2009.

[30] S. Lenhart. Optimal control of a convective-diffusive fluid problem. *Math. Models Method Appl. Sci.*, 5:225–237, 1995.

[31] F. Abergel and R. Temam. On some control problems in fluid mechanics. *Theoretical and Computational Fluid Dynamics*, 1(6):303–325, 1990.

[32] T. Bewley, P. Moin, and R. Temam. Optimal and robust approaches for linear and nonlinear regulation problems in fluid mechanics. *AIAA Paper 97-1872*, 1997.

[33] M. Desai and K. Ito. Optimal controls of Navier-Stokes equations. *SIAM J. Control Optim.*, 32(5):1428–1446, September 1994.

[34] M. Gunzburger, L. Hou, and T. Svobodny. Boundary velocity control of incompressible flow with an application to viscous drag reduction. *SIAM J. Control Optim.*, 30:167–181, 1992.

[35] M. Gunzburger and S. Manservisi. The velocity tracking problem for Navier-Stokes flows with bounded distributed controls. *SIAM J. Control Optim.*, 37(6):1913–1945, September 1999.

[36] M. Gunzburger. Adjoint equation-based methods for control problems in incompressible, viscous flows. *Flow, Turbulence and Combustion*, 65:249–272, 2000.

[37] M. Gunzburger. *Perspectives in Flow Control and Optimization*. SIAM Advances in Design and Control, Philadelphia, 2003.

[38] M. Hinze and K. Kunisch. Control strategies for fluid flows - optimal versus suboptimal control. *Preprint No. 573/98, Technische Universitt Berlin, Germany*, 1998.

[39] M. Hinze and K. Kunisch. Suboptimal control strategies for backward facing step flows. In A. Sydow, editor, *Modelling and Applied Mathematics*, volume 3 of *Proceedings of 15th IMACS World Congress on Scientific Computation*, pages 53–58, 1997.

[40] X. Ma and N. Zabaras. An adaptive hierarchical sparse grid collocation algorithm for the solution of stochastic differential equations. *Journal of Computational Physics*, 228(8):1471–1489, 2004.

[41] F. Nobile, R. Tempose, and C. Webster. A sparse grid stochastic collocation method for partial differential equations with random input data. *SIAM Journal on Numerical Analysis*, 46(5):2309–2345, May 2008.

[42] I. Babuska, F. Nobile, and R. Tempose. A stochastic collocation method for elliptic partial differential equations with random input data. *SIAM Journal on Numerical Analysis*, 45(3):1005–1034, 2007.

[43] H. J. Bungartz and M. Griebel. Sparse grids. *Acta Numerica*, 13:1–123, 2004.

[44] B. Ganapathysubramaniam and N. Zabaras. Sparse grid collocation schemes for stochastic natural convection problems. *Journal of Computational Physics*, 225(1):652–685, July 2007.

[45] X. Ma and N. Zabaras. A stabilized stochastic finite element second-order projection method for modeling natural convection in random porous media. *Journal of Computational Physics*, 227:8448–8471, 2008.

[46] A. C. Antoulas. *Approximation of Large-Scale Dynamical Systems*. SIAM Advances in Design and Control, Philadelphia, 2005.

[47] B. C. Moore. Principal component analysis in linear systems: Controllability, observability, and model reduction. *IEEE Transactions on Automatic Control*, 1:17–31, August 1981.

[48] C. Mullis and R. Roberts. Synthesis of minimum roundoff noise fixed point digital filters. *IEEE Trans. on Circuits and Systems*, pages 551–562, 1976.

[49] E. Grimme. *Krylov projection methods for model reduction*. PhD dissertation, Iniversity of Illinois, Urbana-Champaign, 1997.

[50] P. Feldmann and R. W. Freund. Efficient linear circuit analysis by pade approximation via the lanczos process. *EEE Transactions on Computer-Aided Design of Integrated Circuits and Systems*, 14:639–649, 1995.

[51] P. Holmes, J. Lumley, and G. Berkooz. *Tubulence, Cohenrent Structures, Dynamical Systems and Symmetry*. Cambridge University Press, UK, 1996.

[52] L. Sirovich. Turbulence and the dynamics of cohenrent structures. Part 1: Cohenrent structures. *Quarterly of Applied Mathematics*, 45(3):561–571, October 1987.

[53] G. Berkooz, P. J. Holmes, and J. L. Lumley. The proper orthogonal decomposition in the analysis of turbulent flows. *Annu. Rev. Fluid Mech.*, 25:539–575, 1993.

[54] M. Kirby, J. P. Boris, and L. Sirovich. A proper orthogonal decomposition of a simulated supersonic shear layer. *Int. J. Numerical Methods Fluids*, 10:411–428, 1990.

[55] K. Kunisch K and S. Volkwein. Galerkin proper orthogonal decomposition methods for a general equation in fluid dynamics. *SIAM J. Numer. Anal.*, 40(2):492–515, 2002.

[56] M. Gunzburger, J. S. Peterson, and J. N. Shadid. Reduced-ordr modeling of time-dependent PDEs with multiple parameters in the boundary data. *Comput. Methods Appl. Mech. Engrg.*, 196:1030–1047, 2007.

[57] K. Willcox. Unsteady flow sensing and estimation via the gappy proper orthogonal decomposition. *Computers & Fluids*, 35(2):208–226, 2006.

[58] K. Kunisch and S. Volkwein. Control of the burgers equation by a reduced-order approach using proper orthogonal decomposition. *Journal of Optimization Theory and Applications*, 102:345–371, 1999.

[59] S. S. Ravindran. Proper Orthogonal Decomposition in optimal control of fluids. *Int. J. Numer. Meth. Fluids*, 34:425–448, 1999.

[60] A. J. Fletcher. *Computational Galerkin Methods*. Springer, New York, 1st edition, 1984.

[61] W. R. Graham, J. Peraire, and K. Y. Tang. Optimal control of vortex shedding using low-order models. Part I: Open-loop model development. *International Journal for Numerical Methods in Engineering*, 44(7):945–972, March 1999.

[62] W. R. Graham, J. Peraire, and K. Y. Tang. Optimal control of vortex shedding using low-order models. Part II: Model-based control. *International Journal for Numerical Methods in Engineering*, 44(7):973–990, March 1999.

[63] B. R. Noack, M. Schlegel, M. Morzynski, and G. Tadmor. *Galerkin Method for Nonlinear Dynamics*, volume 528 of *Reduced-Order Modelling for Flow Control, CISM Courses and Lectures*, pages 111–149. Springer Vienna, 2011.

[64] M. Gunzburger and J. Ming. Optimal control of stochastic flow over a backward-facing step using reduced-order modeling. *SIAM J. Sci. Comput.*, 33(5):2641–2663, 2011.

[65] M. Barrault, Y. Maday, N. C. Nguyen, and A. T. Patera. Empirical interpolation method: Application to efficient reduced-basis discretization of partial differential equations. *Comptes Rendus Mathematique*, 339(9):667–672, 2004.

[66] M. A. Grepl, Y. Maday, N. C. Nguyen, and A. T. Patera. Effcients reduced-basis treatment of nonaffine and nonlinear partial differential equation. *Mathematical Modelling and Numerical Analysis*, 41(3):575–605, 2007.

[67] S. Chaturantabut and D. Sorensen. Discrete empirical interpolation for nonlinear model reduction. In *Decision and Control, 2009 held jointly with the 2009 28th Chinese Control Conference. CDC/CCC 2009. Proceedings of the 48th IEEE Conference on*.

[68] S. Chaturantabut. *Nonlinear Model Reduction via Discrete Empirical Interpolation*. PhD dissertation, Rice University, Houston, Texas, 2011.

[69] V. B. Nguyen. *Computational simulation of detonation waves and model reduction for reacting flows*. PhD dissertation, SMA, National University of Singapore, Singapore, 2011.

[70] S. R. Karpik and G. D. Raithby. Laterally averaged hydrodynamics model for reservoir predictions. *Journal of Hydraulic Engineering*, 116(6):783–798, 1990.

[71] L. Bui and K. Mori. A two-dimensional numerical model of wind-induced flow and water quality in closed water bodies. *Paddy and Water Environment*, 5(1):29–40, March 2007.

[72] R. G. Kurup, D. P. Hamilton, and R. L. Phillips. Comparison of two 2-dimensional, laterally averaged hydrodynamic model applications to the Swan river estuary. *Mathematics and Computers in Simulation*, 51(6):627–638, February 2000.

[73] D. R. Maidment. *Handbook of Hydrology*. McGraw-Hill, New York, 1993.

[74] C. D. Wilcox. *Turbulence Modeling for CFD*. DCW Industries, La Caada, California, 1993.

[75] L. Bengtsson. Conclusions about turbulent exchange coefficients from model studies. International Symposium Hydrology of lakes, Helsinki, pages 306–312. IAHS publication, 1973.

[76] R. Codina and J. Blasco. Stabilized finite element method for the transient Navier-Stokes equations based on a pressure gradient projection. *Comput. Methods Appl. Mech. Engrg*, 182:277–300, 2000.

[77] O. C. Zienkiewicz and K. Morgan. *Finite Elements and Approximation*. Wiley, New York, 1983.

[78] A. J. Chorin. Numerical solution of the Navier-Stokes equations. *Math. Comp*, 22:745–762, 1968.

[79] D. P. Kouri. Optimization governed by stochastic partial differential equations. Master thesis, Rice University, Houston, Texas, 2010.

[80] R. G. Ghanem and P. D. Spanos. *Stochastic Finite Elements: A Spectral Approach*. Springer - Verlag, New York, 1991.

[81] U. Ghia, K. N. Ghia, and C. T. Shin. High-resolution for incompressible flow using the Navier-Stokes equations and the multigrid method. *Journal of Computational Physics*, 44:387–411, 1982.

[82] J. Kim, S. J. Kline, and J. P. Johnston. Investigation of a reattaching turbulent shear layer flow over a backward-facing step. *Journal of Fluids Engineering*, 102(3):302–308, 1979.

[83] C. G. Speziale and Tuan Ngo. Numerical solution of turbulent flow past a backward facing step using a nonlinear k–e model. *International Journal of Engineering Science*, 26(10):1099–1112, 1988.

[84] S. Thangam and N. Hur. A highly-resolved numerical study of turbulent separated flow past a backward-facing step. *International Journal of Engineering Science*, 29(5):607–615, 1991.

[85] S. Karaa and J. Zhang. High order ADI method for solving unsteady convectiondiffusion problems. *Journal of Computational Physics*, 198(1):1–9, 2004.

[86] B. J. Noye and H. H. Tan. Finite difference methods for solving the two-dimensional advectiondiffusion equation. *International Journal for Numerical Methods in Fluids*, 9(1):75–98, 1989.

[87] D. W. Peaceman and Jr. H. H. Rachford. The numerical solution of parabolic and elliptic differential equations. *Journal of the Society for Industrial and Applied Mathematics*, 3(1):28–41, 1955.

[88] J. Crank and P. Nicolson. A practical method for numerical evaluation of solutions of partial differential equations of the heat-conduction type. *Advances in Computational Mathematics*, 6(1):207–226, 1996.

[89] G. Hauke. *An Introduction to Fluid Mechanics and Transport Phenomena*, volume 86 of *Fluid Mechanics and Its Applications*. Springer, 2008.

[90] K. Kunisch and L. Xie. *Suboptimal feedback control of flow separation by POD Model Reduction*, chapter 12, pages 233–249. Real-Time PDE-Constrained Optimization. SIAM, 2007.

[91] D. P. Bertsekas. *Nonlinear Programming*. Athena Scientific, second edition, 1999.

[92] C. W. Clenshaw and A. R. Curtis. A method for numerical integration on an automatic computer. *Numerische Mathematik*, 2:197–205, October 1960.

[93] E. T. Jaynes. Information theory and statistical mechanics. *Physical Review*, 104(4):620–630, May 1957.

[94] P. Brémaud. *Markov Chains, Gibbs Fields, Monte Carlo Simulation, and Queues*. Springer-Verlag, New York, 1999.

[95] C. M. Bishop. *Pattern Recognition and Machine Learning - Information Science and Statistics*. Springer, 2006.

[96] Y. C. Ho and R. C. K. Lee. A Baysian approach to problems in stochastic estimation and control. *Automatic Control, IEEE Transactions on*, 9(4):333–339, 1964.

[97] A. V. Oppenheim and G. C. Verghese. Chapter 8: Estimation with minimum mean square error, (class code 6.011). Lecture notes on Introduction to Communication, Control, and Signal Processing, MIT Open Course Ware, 2010.

[98] J. Besag, P. Green, D. Higdon, and K. Mengersen. Bayesian computation and stochastic systems. *Statistical Science*, 10(1):3–41, 1995.

[99] D. A. Siegel and T. D. Dickey. Variability of net longwave radiation over Eastern North Pacific ocean. *Journal of Geophysical Reseach*, 91:7657–7666, June 1980.

[100] S. C. Chapra. *Surface water-quality modeling*. McGraw-Hill, New York, 1996.

[101] J. R. Shewchuk. An introduction to the conjugate gradient method without the agonizing pain. Technical report CMU-CS-94-125, Carnegie Mellon University, School of Computer Science, Carnegie Mellon University, Pittsburgh, PA, 1994.

[102] L. Armijo. Minimization of functions having Lipschitz continuous first partial derivatives. *Pacific Journal of Mathematics*, 16(1):1–3, 1966.

Appendix A

Finite Element Method

A.1 Solar components

We consider the solar component relationships as shown in Figure 2-1. The total net heat flux through the water surface is calculated by the net all-wave radiation [1], given by

$$R_N^* = R_{SN} + R_{AN} - R_{BR} - R_C - R_L. \tag{A.1}$$

1. The net solar shortwave radiation

$$R_{SN} = \beta R_S (1 - \alpha), \tag{A.2}$$

where R_S is the incoming solar shortwave radiation, $\alpha \in (0, 1)$ is the water reflection coefficient, $\beta = 0.65$ is the fraction of solar shortwave radiation. The remaining fraction of the solar shortwave radiation $(1 - \beta)R_S$ is absorbed ex-

ponentially with depth as follows

$$R_z = (1 - \beta)R_S \exp(-\eta H), \tag{A.3}$$

where H is water depth and $\eta = 0.5$ is the extinction coefficient.

2. The down-welling longwave radiation: is expressed in terms of the Stefan-Boltzmann Law, for more details refers to [99],

$$R_{AN} = \sigma\varepsilon_{eff}(273 + T_a)^4 = \sigma\varepsilon_{cs}F_{cs}(273 + T_a)^4. \tag{A.4}$$

Here T_a is air temperature, $\sigma = 5.67 \times 10^{-8}(Wm^{-2}K^{-4})$ is Stefan-Boltzmann constant, $\varepsilon_{eff} = \varepsilon_{cs}F_{cs}$ is referred to as the effective or apparent emissivity, $F_{cs} \geq 1$ is a cloud factor expressing the increase in clear-sky, ε_{cs} is the clear-sky atmospheric emissivity,

$$\varepsilon_{cs} = (1 - r_a)(1 + 0.17 * C^2)K_f T_a^2, \tag{A.5}$$

where $r_a = 0.03$ is the albedo for long wave radiation, $K_f = 9.37 \times 10^{-6}(K^{-2})$ a coefficient and $0 \leq C \leq 1$ is cloud cover fraction.

3. The up-welling longwave radiation: follows the same formulation of the dow-welling, in which air temperature T_a is replaced by water surface temperature T_s,

$$R_{BR} = \sigma\varepsilon_w(273 + T_s)^4, \tag{A.6}$$

where the emissivity ε_w is fixed at 0.975.

4. The evaporative loss (latent heat flux) from the water is given as

$$R_L = f(U_a)(e_s - e_a), \tag{A.7}$$

where e_s and e_a is the saturation vapor pressure above the water surface and the vapor pressure of air (hPa), which can be computed from [100],

$$e_s = 4.596 \exp\left(\frac{17.27T_a}{237.3 + T_a}\right), \tag{A.8}$$

$$e_a = \frac{e_s R_h}{100}, \tag{A.9}$$

where R_h is relative humidity. The function of U_a is expressed as follows

$$f(U_a) = 7.6 \times 10^{-4} \times (9.2 + 0.46U_a^2). \tag{A.10}$$

5. The conduction heat loss (sensible heat flux) from the water

$$R_C = 0.47f(U_a)(T_s - T_a). \tag{A.11}$$

Note that the dimension of all the radiation fluxes are expressed as energy per unit area (Wm^{-2}).

A.2 Finite Element Methods

A.2.1 Linear triangular element

Consider a linear triangular element with three nodal values $\phi_i = (u, w, p, c, T)_i$ and nodal coordinate $(x, z)_i$, with $i = 1, 2, 3$ as shown in Figure A-1. The variable interpolation within the element is linear in x and z directions, as

$$\phi = \alpha_0 + \alpha_1 x + \alpha_2 z, \tag{A.12}$$

where α_i are constants to be determined.

The interpolation function (A.12) should represent the nodal variables at the three nodal points. Therefore, substituting x and z values at each nodal point gives

$$\begin{bmatrix} 1 & x_1 & z_1 \\ 1 & x_2 & z_2 \\ 1 & x_3 & z_3 \end{bmatrix} \begin{pmatrix} \alpha_0 \\ \alpha_1 \\ \alpha_2 \end{pmatrix} = \begin{pmatrix} \phi_1 \\ \phi_2 \\ \phi_3 \end{pmatrix}. \tag{A.13}$$

Inverting the matrix and rewriting equation (A.13), gives

$$\begin{pmatrix} \alpha_0 \\ \alpha_1 \\ \alpha_2 \end{pmatrix} = \frac{1}{2A} \begin{bmatrix} a_1 & a_2 & a_3 \\ b_1 & b_2 & b_3 \\ c_1 & c_2 & c_3 \end{bmatrix} \begin{pmatrix} \phi_1 \\ \phi_2 \\ \phi_3 \end{pmatrix}, \tag{A.14}$$

where A is the area of the triangle and is given by the determinant

$$A = \frac{1}{2} \det \begin{bmatrix} 1 & x_1 & z_1 \\ 1 & x_2 & z_2 \\ 1 & x_3 & z_3 \end{bmatrix}, \tag{A.15}$$

and

$$a_1 = x_2 z_3 - x_3 z_2 \quad b_1 = z_2 - z_3 \quad c_1 = x_3 - x_2$$

$$a_2 = x_3 z_1 - x_1 z_3 \quad b_2 = z_3 - z_1 \quad c_2 = x_1 - x_3 \tag{A.16}$$

$$a_3 = x_1 z_2 - x_2 z_1 \quad b_3 = z_1 - z_2 \quad c_3 = x_2 - x_1.$$

Substituting the coefficients into equation (A.12) and rearrange, we have

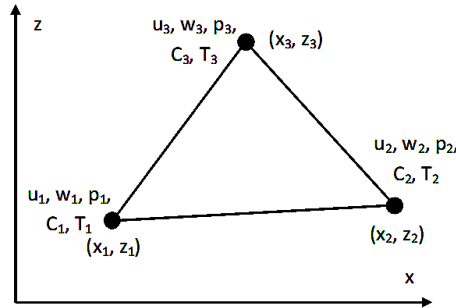Figure A-1: Linear triangle element.

$$\phi = H_1 \phi_1 + H_2 \phi_2 + H_3 \phi_3, \quad \text{or} \quad \phi = \mathbf{H} \phi^{(e)}. \tag{A.17}$$

Here $\mathbf{N}$ are the shape functions, defined as

$$H_1 = \tfrac{1}{2A}(a_1 + b_1 x + c_1 z),$$

$$H_2 = \tfrac{1}{2A}(a_2 + b_2 x + c_2 z), \tag{A.18}$$

$$H_3 = \tfrac{1}{2A}(a_3 + b_3 x + c_3 z),$$

These shape functions satisfy the conditions

$$H_i(x_j, z_j) = \delta_{ij}, \tag{A.19}$$

$$\sum_{i=1}^{3} H_i = 1. \tag{A.20}$$

Here δ_{ij} is is the Kronecker delta function.

A.2.2 Elemental Matrices

The finite element matrices are evaluated on each element as

$$\mathbf{M}^e = \int_{\mathcal{D}^e} \mathbf{H}^T \mathbf{H} d\mathcal{D}^e, \tag{A.21}$$

$$\mathbf{G}_x^e = \int_{\mathcal{D}^e} \mathbf{H}^T \frac{\partial \mathbf{H}}{\partial x} d\mathcal{D}^e, \tag{A.22}$$

$$\mathbf{G}_z^e = \int_{\mathcal{D}^e} \mathbf{H}^T \frac{\partial \mathbf{H}}{\partial z} d\mathcal{D}^e, \tag{A.23}$$

$$\mathbf{L}^e = \int_{\mathcal{D}^e} \nabla \mathbf{H}^T \nabla \mathbf{H} d\mathcal{D}^e, \tag{A.24}$$

$$\mathbf{f}_x^e = \int_{\mathcal{D}^e} \mathbf{H}^T f_x d\mathcal{D}^e, \tag{A.25}$$

$$\mathbf{f}_z^e = \int_{\mathcal{D}^e} \mathbf{H}^T f_z d\mathcal{D}^e, \tag{A.26}$$

$$\mathbf{C}^e(\mathbf{u}) = \int_{\mathcal{D}^e} \mathbf{H}^T \left(\mathbf{H} u_h \frac{\partial \mathbf{H}}{\partial x} + \mathbf{H} w_h \frac{\partial \mathbf{H}}{\partial z} \right) d\mathcal{D}^e +$$
$$\int_{\mathcal{D}^e} \mathbf{H}^T \mathbf{H} \left(\frac{\partial \mathbf{H}}{\partial x} u_h + \frac{\partial \mathbf{H}}{\partial z} w_h \right) d\mathcal{D}^e, \tag{A.27}$$

$$\mathbf{K}^e(\mathbf{u}) = \int_{\mathcal{D}^e} \nu(\mathbf{u}) \nabla \mathbf{H}^T \nabla \mathbf{H} d\mathcal{D}^e, \tag{A.28}$$

$$\mathbf{A}^e(\mathbf{u}) = \int_{\mathcal{D}^e} \mathbf{H}^T \left(\frac{\partial \mathbf{H}}{\partial x} u_h + \frac{\partial \mathbf{H}}{\partial z} w_h \right) d\mathcal{D}^e, \tag{A.29}$$

$$\mathbf{D}^e(\mathbf{u}) = \int_{\mathcal{D}^e} \left(\mathbf{H} u_h \frac{\partial \mathbf{H}^T}{\partial x} + \mathbf{H} w_h \frac{\partial \mathbf{H}^T}{\partial z} \right) d\mathcal{D}^e. \tag{A.30}$$

$$\mathbf{K}_c^e = \int_{\mathcal{D}^e} \kappa(\boldsymbol{\theta}^k) \nabla \mathbf{H}^T \nabla \mathbf{H} d\mathcal{D}^e, \tag{A.31}$$

$$\mathbf{f}_c^e = \int_{\mathcal{D}^e} \mathbf{H}^T f_c d\mathcal{D}^e, \tag{A.32}$$

$$\mathbf{C}_c^e(\mathbf{u}) = \int_{\mathcal{D}^e} \mathbf{H}^T \Big(\mathbf{H} u_h \frac{\partial \mathbf{H}}{\partial x} + \mathbf{H} w_h \frac{\partial \mathbf{H}}{\partial z} \Big) d\mathcal{D}^e. \tag{A.33}$$

Appendix B

Optimization algorithm for control

Algorithm 1 is a general procedure to solve for deterministic control, stochastic control with deterministic source and stochastic control with uncertain source. For particular problem, we need to set the input parameter appropriately. For example, if the deterministic control is considered, we set $P = 0$, $N_G = 0$; $\Theta = 0$, etc.

To solve the KKT system, the Crank-Nicolson method [88] is used to discretize the state, adjoint and optimality condition equations in time. The conjugate gradient method [101] is employed to solve the linearized system; the Armijo line-search [102] is used to ensure convergence.

1. Initial work

    1a. Given P, $\mathcal{D}$, N_G, $\mathbf{\Theta}$, $\mathbf{\Phi}$, initial velocity $\mathbf{u}_0$, tolerance ε. Set $j = 0$

    1b. Given the FEM basis φ_l for $l = 1, ..., N$, where N is the number of grid points

    1c. Compute the matrices $\mathbf{M}$, $\mathbf{C_c}(\mathbf{u})$

1d. Compute collocation point $\{\theta^k = (\xi, \eta)\}_{k=1}^P$ and collocation weights

$\{w^k\}_{k=1}^P$.

2. Solve for the KKT system

For $j = 1 : N_G$

    2a. Compute vector $\mathbf{F}(\boldsymbol{t}, \boldsymbol{\phi}_j) = \int_{\mathcal{D}} f(\mathbf{x}, t, \boldsymbol{\phi}_j) \varphi_i d\mathbf{x}$

    For $k = 1 : P$

        2b. Compute input $\kappa(\mathbf{x}, t; \mathbf{Y})$ at each $\boldsymbol{\theta}^k$

        2c. Compute $\mathbf{K}(t; \boldsymbol{\theta}^k) = \int_{\mathcal{D}} \kappa(\mathbf{x}, t; \mathbf{Y}) \nabla \varphi_i(\mathbf{x}) \cdot \nabla \varphi_l(\mathbf{x}) d\mathbf{x}$

        2d. Solve the state equations with input $\mathbf{u}_j$

        2e. Solve the adjoint equations

        2f. Store results

    end

end

3. Compute the optimal control

    3.a Compute the cost-functional $\hat{\mathcal{J}}(\mathbf{u}_j)$ and the gradient $\mathrm{grad}(\mathbf{u}_j)$

    3.b If $\|\mathrm{grad}(\mathbf{u}_j)\| < \epsilon \rightarrow$ stop.

    3.c Perform Armijo line search

        • Set $s_j = -\mathrm{grad}(\mathbf{u}_j)$

        • Set $\alpha_j = 1$ then evaluate $\hat{\mathcal{J}}(\mathbf{u}_j + \alpha_j s_j)$, and gtol $= 10^{-4} \alpha_j s_j^T \mathrm{grad}(\mathbf{u}_j)$

        • While $\hat{\mathcal{J}}(\mathbf{u}_j + \alpha_j s_j) > \hat{\mathcal{J}}(\mathbf{u}_j) + $ gtol

        Set $\alpha_j = \alpha_j/2$ and evaluate $\hat{\mathcal{J}}(\mathbf{u}_j + \alpha_j s_j)$.

    3.d Set $\mathbf{u}_{j+1} = \mathbf{u}_j + \alpha_j s_j$, and $j = j + 1$. Go to step 2.